ABSTRACT

Title of Document: **OPTICAL COHERENCE TOMOGRAPHY FOR NEUROSURGEY AND CANCER RESEARCH.**

Chia-Pin Liang, Doctor of Philosophy, 2014

Directed By: Assistant Professor, Yu Chen,
Fischell Department of Bioengineering

Optical Coherence Tomography (OCT) provides non-labeling, real-time and high resolution images, which has the potential to transform the paradigm of surgical guidance and preclinical animal studies. The design and development of OCT devices for neurosurgery guidance and novel imaging algorithms for monitoring anti-cancer therapy have been pursued in this work. A forward-imaging needle-type OCT probe was developed which can fit into minimally invasive tools (I.D. ~ 1mm), detect the at-risk blood vessels, and identify tissue micro-landmarks. This promising guidance tool improves the safety and the accuracy of needle-based procedures, which are currently performed without imaging feedback. Despite the great imaging capability, OCT is limited by the shallow imaging depth (1-2 mm). In order to address this issue, the first MRI compatible OCT system has been developed. The multi-scale and multi-contrast MRI/OCT imaging combination significantly improves the accuracy of intra-operative MRI by two orders (from 1mm to 0.01 mm). In contrast to imaging systems, a thin (0.125 mm), low-cost (1/10 cost of OCT system) and simple fiber sensor technology called coherence gated Doppler (CGD) was developed which can be integrated with many surgical tools and aid in the avoidance of intracranial hemorrhage. Furthermore, intra-vital OCT is a powerful tool to study the mechanism of anti-cancer therapy. Photo-immunotherapy (PIT) is a low-side-effect cancer therapy based on an armed antibody conjugate that induces highly selective cancer cell necrosis after exposure to near infrared light both in vitro and in vivo. With novel algorithms that remove the bulk motion and track the vessel lumen automatically, OCT reveals dramatic hemodynamic changes during PIT and helps to elucidate the mechanisms behind the PIT treatment. The transformative guidance tools and the novel image processing algorithms pave a new avenue to better clinical outcomes and preclinical animal studies.

OPTICAL COHERENCE TOMOGRAPHY FOR NEUROSURGERY AND CANCER RESEARCH

By

Chia-Pin Liang

Dissertation submitted to the Faculty of the Graduate School of the
University of Maryland, College Park, in partial fulfillment
of the requirements for the degree of
Doctor of Philosophy
2014

Advisory Committee:
Assistant Professor Yu Chen, Chair
Professor Cha-Min Tang
Assistant Professor Ian White
Associate Professor Adam Hsieh
Professor Jaydev Desai, Dean's Representative

Dedication

This work is dedicated to my family, who has taught me about the most important things in life.

Acknowledgements

And now for the most important part of the dissertation.

First, I would like to thank my advisor, Dr. Yu Chen for providing me with resources, opportunity and latitude to pursue this research. It is been a great privilege to work with Dr. Chen because I do not think there is a nicer guy any student could have had as an adviser. I am grateful for the time and energy he has put into educating and training me on various imaging technologies. Whenever help is needed, he is always accessible. He creates extensive collaborations with top-notch labs and supports me to pursue exciting projects with experts in various fields. The excellent multidisciplinary environment enriches my knowledge in many fields intersecting engineering, medicine, and biology, and broadens my vision in science and research. He also generously helps me develop other professional skills by funding me to present at major conferences and providing me the opportunity to write research grants. More importantly, he teaches me and shows me that the persistence and dedication is the only way to achieve the highest level of excellence. In the face of adversity, his optimism and encouragement keeps me focused on the problems, not on negative emotions. His passion and attitude towards research will continue to influence me in my future career.

I wish to thank all the outstanding collaborators who have aided me along the way in my research:

Drs. Cha-Min Tang and Jafri Samir from the University of Maryland School of Medicine (UMSOM) provided an excellent environment for testing our neurosurgery

guidance tools in large animals *in vivo*. Without their knowledge of neurosurgery and project guidance, it would not have been possible to create a translational device. I would like to extend a special thanks to Dr. Tang, who is a pioneer of using OCT for neurosurgery and always proposes innovative engineering solutions for unmet clinical needs. His wisdom and insightful suggestions exhilarated every discussion projecting new ideas and towards progressive research.

Professor Jaydev Desai at the University of Maryland, College Park (UMCP) is a pioneer in medical robotics and spearheads the exciting and emerging field of image-guided interventions (IGI) by tele-operated robots. His lab develops innovative MRI-compatible robots and steerable cannulas, which allow us to explore the new territories that we could not imagine before. These incredible devices deliver our imaging probe into the previously inaccessible places and enables us to perform OCT imaging under continuous MRI monitoring. Their creativity and vision have significant impact on biomedical imaging and could potentially transform the current paradigm of IGI. I would like to thank Dr. Desai and his students, Yang Bo and and Elif Ayvali, for collaborating with us and patiently instructing us on how to use these sophisticated devices. I also would like to give special thanks to Dr. Desai for his generosity and kindness to serve in my thesis committee and for his critical comments, which significantly improved the quality of this dissertation.

Dr. Rao Gullapalli's group from the UMSOM provides us a valuable resource of MRI and their abundant knowledge in radiology. I was fortunate to have a radiology expert's valuable input for improving the system. Dr. Gullapalli's experience and constructive suggestions have saved us tons of time while developing the MRI-

compatible OCT endoscope. I also would like to thank Dr. Gullapalli for educating me on the fundamentals of MRI which broadens my knowledge base in medical imaging and radiology.

Dr. Joe Schmitt from St. Jude Medical developed the first CGD device and kindly passed on the schematic of his first design to me. He is one of the most knowledgeable engineers I have ever worked with. Discussing improvements to the system with him has been one of the most informative and educational experiences. I also want to thank Joe for providing me his great suggestions and experience on career choices. I would like to extend a special thanks to Joe's coworker, Dr. Chris Peterson for making the custom-made fiber probes for us.

Drs. Hisataka Kobayashi and Peter Choyke from the National Cancer Institute (NCI) have provided me the opportunity to study the novel photo-immunotherapy (PIT). The engaging conversation with Dr. Kobayashi greatly enriches my knowledge on cancer biology. He is dedicated to the development of anti-cancer therapy and is my best role model of a great scientist. Also his great mentorship makes our collaboration a truly enjoyable experience. Thanks Drs. Takahito Nakajima, Rira Watanabe, and Kazuhide Sato for preparing animals for PIT studies. Their expertise and skills are critical to the success of this project. I am grateful to Dr. Choyke for sharing his keen insights on PIT and his great comments on data interpretation.

Drs. Anthony Sandler and Kyle Wu from the Children's National Medical Center provide a great environment for preclinical large animal studies. It is my great privilege to explore the new applications of our devices with surgeons who are so skillful and open-minded. I would like to thank them for being so supportive and

encouraging when we encountered obstacles. I really hope we can have more opportunities to collaborate in the future.

I would like to give my sincerest thanks to Drs. Ian White and Adam Hsieh for serving on my thesis committee. Defense of my proposal and thesis has been one of the most educational experiences. Their critical comments sharpen my thinking and motivate me to achieve higher goals. Their constructive feedback greatly enhanced the quality of this work.

I also want to acknowledge my great lab-mates, Drs. Jerry Wierwille and Chao-Wei Chen, for their companionship and mentorship. Our countless lunch chats are my most important lesson of American culture and constitute some of my best memories from UMD. To Qinggong Tang and Nick Woolsey for their help on research. It was a terrific experience to share time with you both in and out of the lab. I have no doubt that I will hear your great achievements one day. To Allen Wu for your efforts on the CGD project. Thank you for finishing all the programming in a very short time frame which was crucial to the success for the CGD project. I wish you the best in Denmark. To Jay Kim for assisting in the MRI/OCT projects. It was a great experience of building the first MRI-compatible OCT system with you. I could never forget the excitement when we first saw the MRI/OCT images. To Dr. Jiangting Wang for your generosity and hospitality. Thank you for hosting so many happy hours for the lab. To the top-notch postdocs in our lab, Drs. Hengchang Guo, Hyounguk Jang, Zhengyang Ding, Jiangting Wang and Hsingwen Wang. Thank you for sharing your great experience and knowledge with me. It is my great honor to work with you.

Finally to my family and girlfriend, your support and love always keep me light-hearted and motivate me to move forward. Without you, none of this would have been remotely possible.

Table of Contents

List of Figures

Chapter 6

Chapter 7

Chapter 1: Introduction

1.1 Motivation

1.1.1 Neurosurgery

Navigating instruments accurately and safely to deep brain targets significantly impacts the therapeutic outcome of stereotactic neurosurgery. A fundamental limitation of needle-based stereotactic neurosurgeries, such as biopsy [1, 2], catheterization [3, 4], and electrode placement [5, 6] is that they are blind procedures in which the operator does not have real-time feedback as to what lies immediately ahead of the advancing instrument. This results in several problems:

I. Numerous medium sized blood vessels which cannot be detected by CT and MRI are at risk of being lacerated by the advancing probe. Lacerated vessels in the brain can lead to stroke and death [7-9].

II. The discrepancy between the actual position of the gray matter targets and its pre-operatively determined coordinate caused by inaccuracy of imaging navigation, intra-operative positioning issues and loss of cerebrospinal fluid can lead to false biopsy [10], failure of surgery [11] and severe adverse events [12].

III. Connectomic surgery that can restore many brain diseases by stimulating specific neural fiber tracts [13-15] also requires precise intra-operative guidance to locate the pathology-related fiber tracts. Electrode misplacement by a few mm would generate no therapeutic effects [15] at all.

In order to address the challenges of performing stereotactic neurosurgery safely and accurately, several intra-operative optical guidance tools have been developed and tested with in vivo large animal experiments in this study.

1.1.2 Photoimmunotherapy

Photo-immunotherapy (PIT) is a low-side-effect cancer therapy based on an armed antibody conjugate that induces rapid cellular necrosis after exposure to near infrared light. The conjugate consists of a hydrophilic photosensitizer phthalocyanine dye, IR700, which is covalently bound to a humanized monoclonal antibody. When exposed to near-infrared light, the conjugate induces highly selective and rapid cancer cell death both in vitro and in vivo [16, 17]. Selective destruction of perivascular cancer cells while leaving most of tumor blood vessels unharmed leads to 24-fold greater accumulation of nanomaterials in the tumor bed and significantly improves the efficacy of a nano-anti-cancer drug [18]. This effect is termed super-enhanced permeability and retention (SUPR). Histology and fluorescence images confirm that high concentration of non-specific nanomaterials can penetrate into the tumor bed away from the tumor blood vessels after the PIT treatment. However, little is known about how the tumor vasculature responds while the perivascular cancer cells are destroyed during PIT. Will the lumen still open for drug delivery? Will the blood flow speed increase or decrease due to dramatic change of interstitial pressure? In this study, we used intra-vital optical coherence tomography (OCT) to monitor tumor hemodynamics and study the mechanism behind the SUPR effect.

1.2 Background

1.2.1 Intracranial hemorrhage

Cerebral Hemorrhage is one of the leading complications of needle-based stereotactic neurosurgery. Severe hemorrhage requires immediate surgical evacuation; otherwise increased intracranial pressure will lead to coma and death. Even with emergency treatments, however, patients may still suffer from neurological deficit or paralysis. The overall hemorrhage rates of stereotactic brain biopsy is as high as 59.8% and the risk of symptomatic hemorrhage is 8.8% [19]. Biopsy of deep seated lesion (basal ganglion and thalamus) is associated with 2-fold higher hemorrhage risk than other regions [20]. One study reported that three in twelve cases of biopsy in basal ganglion and thalamus developed the hematoma requiring surgical removal and two of these three patients resulted in permanent hemiparesis [21]. On the other hand, hemorrhage is also one of the most worried complications of deep brain stimulation (DBS) surgery. DBS is a surgical approach for managing certain neurologic and psychiatric disorders [22, 23] by implanting therapeutic electrodes to deep brain targets. The most widely accepted condition is Parkinson's disease (PD) [24, 25]. The symptomatic hemorrhage rate associated with the insertion of sharp electrodes is 2-5% [26-31] and 2- to 8-fold higher for hypertensive patients [26, 29, 31]. The sever consequence includes permanent paralysis and death [8, 9, 11]. The major problem is that operators do not have real-time imaging feedback of the vessels lying ahead of advancing needles. Therefore, there is a critical need to detect the at-risk vessels sitting in front of the advancing instrument.

1.2.2 Stereotactic discrepancy

Despite with the preoperative CT or MRI guidance, loss of cerebrospinal fluid once the cranium is open, inaccuracy of imaging navigation and brain shift due to positioning can lead to marked discrepancies in stereotactic coordinate up to 1 cm [32]. In the surgery targeting the deep brain nuclei in size of few mm to cm, the offset could result in failed surgery. In DBS surgery, for example, considering how close critical pathways travel next to each other in these nuclei, it is not surprising that even mm shift of the electrodes can introduce unwanted side effects, such as muscle twitching, unpleasant sensation and acute depression [33]. Also, along with the development of gene or cell therapies for neurological disorders, precise delivery of therapeutic agents into a specific brain region becomes more and more important. For example, in the glial-cell derived neurotrophic factor (GDNF) trials for PD (34 patients), misplaced infusion catheters led to severe adverse events and required surgical repositioning in two patients and complete removal in another [12]. Currently, microelectrode recording (MER) is gold standard for compensating the stereotactic discrepancy. Deep brain nuclei are typically identified by their characteristic neural firing patterns [34]. However, refinement mapping comes at cost. Inserting the electrode for mapping in one track requires up to 2 hours and typically 3 or more tracks are necessary to locate the target. Therefore, guiding therapeutic instrument efficiently and accurately to the target is still an unmet challenging.

1.2.3 Connectomic neurosurgery

Connectomic neurosurgery that directly targets white matter tracts connecting different functional hubs is gaining importance in neurosurgical interventions [15].

There is growing evidence that abnormal connectivity between these hubs could lead to pathological brain states [35-37]. For example, one study has demonstrated increased connectivity between cortex and subthalamic nucleus (STN) plays an important role in the generation of Parkinsonian symptoms [35]. De-synchronization of these mis-wired circuits by electrical stimulation could restore the abnormal brain function [38]. However, there is no effective intra-operative guidance tool to locate these tracts. MER cannot acquire signal from the fiber tracts. Deviation from the tractographically defined target, such as dentatorubrothalamic (DRT) tract can lead to poor tremor control, as shown in a patient with bilateral DBS for essential tremor [15]. In theory, diffusion tensor imaging provided by MRI can locate these fiber tracts, but in reality, intra-operative MRI tractography still suffers from poor signal to noise ratio, large voxel size and fiber orientation ambiguity at crossing points [15]. Therefore, there is critical need to develop intra-operative guidance tools that can specifically target these pathologically-related tracts and it is also important to develop better imaging technology for studying the connectome in the micro-scale.

1.2.4 PIT and SUPR effect

Photo-immunotherapy (PIT) is an emerging low-side-effect cancer therapy based on monoclonal antibody (mAb) conjugated with a near-infrared (NIR) phthalocyanine dye (IR700) that induces selective cancer cell necrosis after exposure to near infrared light [39]. PIT induces much less side effect than other anti-cancer therapies due to the targeting capability. Unlike radio ablation, which damages all the tissue close to the energy source, PIT only destroys the cells conjugated with mAb and received NIR photons. Surrounding tissues that have low affinity to mAb are not damaged, because

PIT conjugates that receive NIR photons in light illumination path, but do not bind with cell membrane receptors, are not toxic for the cells. This is a distinctive feature compared with conventional photodynamic therapy and external X-ray therapy, which both damage the tissues in the illumination path. Compared with the radio immunotherapy, PIT offers an advantage of only affecting the region received photons. PIT does not damage the organs that have high accumulation of the drug but have no NIR exposure.

When exposed to near-infrared light, the PIT conjugate induces highly selective cancer cell death while leaving most of tumor blood vessels unharmed and leads to an effect termed super-enhanced permeability and retention (SUPR). PIT treatment destroying the perivascular barrier without damaging the transportation vessels significantly enhances the accumulation of non-specific nanomaterials in the tumor bed and significantly improves the efficacy of nano-anti-cancer drug [18]. Histology and ex vivo fluorescence images show that high concentration of non-specific nanomaterials can penetrate into the tumor bed away from the tumor blood vessels after the PIT treatment [18].

1.3 Emerging tools for neurosurgery and cancer research

1.3.1 OCT for neurosurgery

OCT is an elegant solution to address the challenges in stereotactic neurosurgery: targeting brain nuclei [40] , avoiding hemorrhage [41], and locating tractographically defined fibers [42]. Dr. Tang's group inserted a side-viewing OCT probe into human brain ex vivo following the surgical trajectory toward a DBS target, GPi [40]. The

structural information provided clear landmarks for determining the probe location. Operators can easily know whether the probe has reached or passed GPi by the surrounding landmarks, including white matter lamina and internal capsule. The same group also demonstrated the structural OCT imaging can guide drug delivery or tissue dissection aiming at specific deep brain targets in small rodents in vivo [43]. On the other hand, optical microangiography (OMAG) provides sensitive and high resolution brain blood vessel imaging [44]. Furthermore, polarization-sensitive OCT (PSOCT) allows the white matter track to be isolated from gray matter based on the birefringence contrast and PSOCT can also measure the orientation of fiber tracks [42]. Therefore, an OCT system that possesses three imaging protocols — structure, Doppler, and polarization is a promising tool for neurosurgery guidance.

1.3.2 OCT for cancer research

OCT is an emerging biomedical imaging tool, which provides depth-resolved images similar to ultrasound images. However, OCT sends light waves instead of sound waves into tissue and thus has much better resolution (~ 0.01 mm) than ultrasound (~ 1 mm). OCT can provide 3D high resolution image of tumor microarchitecture, angiography, lymphangiography and viability [45]. It has been widely used in cancer research to study both cellular and vascular response to cancer therapy. For instance, Doppler OCT (DOCT) has been used to monitor vascular changes caused by photodynamic therapy [46]. However, it remains challenging to obtain in situ information without window chamber due to motion artifact. In this study, we overcome this challenge by real-time motion gating using speckle variance (SV) imaging. Furthermore, we develop a vessel lumen recognition algorithm to

automatically quantify the size of open lumen and the blood flow speed. With the novel imaging algorithms, we can obtain the important in situ information from tumor bearing mice without the window chamber.

1.3.3 Endoscopic OCT[1]

Using fiber-optics and micro-optics components, OCT can be readily integrated with a wide range of imaging devices such as endoscope, laparoscope, catheter, and needle which enable imaging inside the body [47]. Detailed methods of various endoscopic OCT design have been introduced in previous review papers [48, 49]. Depending on the clinical applications, endoscopic OCT can be designed to be either flexible or rigid. For example, imaging the vascular system and the gastrointestinal (GI) tract usually requires the probe to be flexible. For applications involving incision-based procedures such as image-guided biopsy, a rigid probe will be desired. Endoscopic OCT can be categorized by imaging direction too. Forward-imaging OCT probe provides information of the tissue located in front of the probe for image-guided biopsy or device placement. On the other hand, side-imaging probe provides circumferential information from the tissue surrounding the probe. Side-imaging devices are uniquely suitable for scanning the lumen of tubular systems (such as the vascular system or the GI tract). In this section, we summarize endoscopic OCT based on different beam delivery methods and beam scanning mechanisms.

Most of the current endoscopic OCT devices use a single-mode fiber to deliver the light into the tissue and collect the backscattering signals. To form a high-fidelity

[1] The content of this section is reproduced from "C.-P Liang, C. Chen, J. Wierwille, J. Desai, R. Gullapalli, R. Mezrich, C.-M. Tang and Y. Chen, "Endoscopic Microscopy Using Optical Coherence Tomography," Current Medical Imaging Reviews 8, 174-193 (2012) ." with perimission.

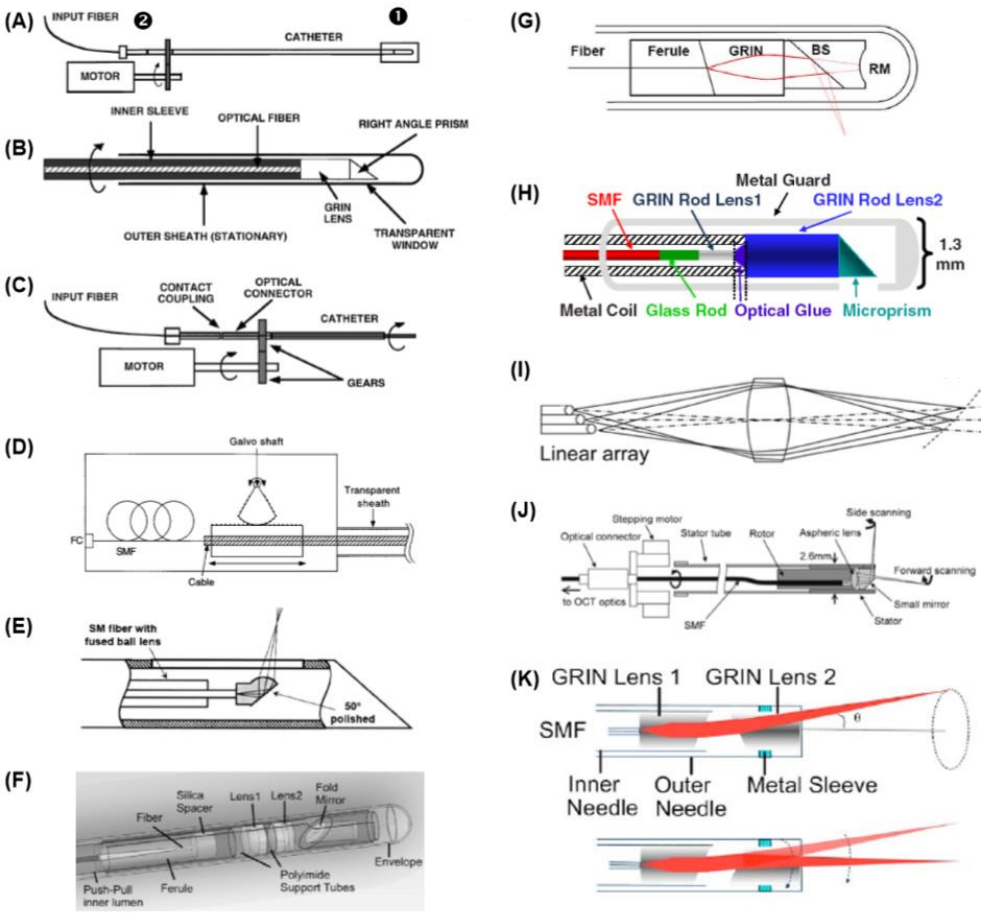

Fig. 1-1. Proximal actuated OCT imaging devices.

(A) Circumferential scanning catheter. (B) and (C) corresponding to portions 1 and 2 in (A), respectively. (B) Distal tip of the OCT imaging catheter, consisting of a single-mode fiber, a GRIN lens, and a microprism. (C) Rotary actuation system. (A)-(C) are from Ref. [50]. (D) Linear actuation system, from Ref. [51]. Single mode fiber (SMF). Fiber Coupler (FC). (E) Distal tip of the OCT imaging catheter, with an angle-cut ball-lensed fiber replacing the GRIN lens, from Ref. [52] (F) Distal tip of the OCT imaging catheter with chromatic aberration correction using a pair of doublets, from Ref. [53] (G) Distal tip of the OCT imaging catheter integrating the reference arm optics in the distal end of the probe, from Ref. [54]. Beam splitter (BS). Reference mirror (RM). (H) A balloon imaging catheter with long working distance, from Ref. [55] (I) Multi-channel parallel imaging probe, from Ref. [56] (J) A combined forward- and side-imaging OCT catheter, from Ref. [57] (K) Forward imaging using paired angle rotation scanning (PARS) techniques, from Ref. [58]. The figure is reprinted from ref [59] with permission.

image, precise scanning of the illumination spot on the tissue is critical. Depending on the actuation mechanisms, endoscopic imaging can be categorized by either proximal or distal actuation. Alternatively, light can be delivered through fiber bundle or gradient-index (GRIN) rod lens, which can relay beam scanning at the proximal end to the distal tip and therefore no scanning device is required in the endoscope.

1. Single Fiber Delivery and Proximal Actuation: The general endoscope design consists of two parts: the optical component for projecting a micron-sized light spot onto the tissue and the mechanical component for scanning the spot to form two-dimensional (2D) or three-dimensional (3D) images. The first endoscopic OCT design was reported by Tearney et al. [47, 50] as shown in Fig. 1-1A. They assembled a GRIN lens to the end of a single mode fiber to focus the emitted light to a spot and attached a prism to deflect the light for side-viewing images (Fig. 1-1B). Rotary (circumferential) scanning was achieved by using a motor and a gear system at the proximal end of the endoscope (Fig. 1-1C). The outer diameter and working distance of this probe were 1.1 mm and 2.5 mm, respectively. Later, a similar optical design was incorporated into a 27 gauge (~ 470 μm) hypodermic needle by Li et al. [60]. Doppler imaging was also demonstrated with the rotary imaging catheter [61]. Besides rotation, side-view imaging can be also achieved by linearly scanning the proximal end of the catheter. Bouma and Tearney developed a linear-scanning OCT endoscope by converting the angular displacement of a galvanometer shaft into linear displacement of the OCT catheter (Fig. 1-1D) [51]. Later, a similar actuation system was used by Yang et al. for Doppler OCT [62]. Proximal linear actuation can also be achieved by using a magnetic actuator [63] or a linear galvanometer [64]. By combining the rotary and linear (pull-back) actuations, spiral scans can be performed to acquire a 3D cylindrical image [55, 63, 65-68].

The distal optics can be further simplified or improved. Yang et al. used an angle-cut, ball-lensed fiber to replace the GRIN lens (Fig. 1-1E) in an interstitial Doppler imaging needle [52], and a similar design has been developed for an intraoperative

OCT probe [69]. Tumlinson et al. have improved the axial resolution to 3.2 μm by correcting the chromatic aberration using a pair of doublets (Fig. 1-1F) [53]. The same group also integrated a beam splitter to the distal end of the OCT endoscope (Fig. 1-1G) [54]. This design avoided the dispersion and polarization mismatch between the sample and reference arms and thus improved the axial resolution to 2.4 μm.

To increase the working distance for imaging organs with larger diameter (such as the GI tract), Fu et al. developed a balloon imaging catheter [55] with miniature GRIN lenses that reduced the spot size from the fiber diameter (9 μm) to 3.5 μm and provided ~20 μm spot at focal point 9 mm away from the probe (Fig. 1-1H). Moreover, the same group used a cylindrical reflective mirror to correct the astigmatism caused by the wall of balloon catheter to achieve diffraction-limited, high–resolution imaging with long working distance [70]. Balloon catheters have also been developed by other groups at the Massachusetts General Hospital [66, 67] and Case Western Reserve University for GI tract imaging [68].

High NA optics provides improved transverse resolution but suffers from shallow imaging depth of field. To overcome this limitation, Yang et al. used an elliptical MEMS membrane mirror to dynamically adjust the beam focus along with the movement of the reference mirror [71]. Other groups have used electrically controlled liquid lens [72] or pneumatically actuated micro-lens [73] to vary the focal plane position. Another approach is parallel imaging utilizing a multi-channel OCT setup (Fig. 1-1I) to separate the entire depth of field into independent channels [56]. Recently, this design has been used for in vivo animal GI tract imaging [74].

In certain applications, it is desired to have both side-imaging and forward-imaging capabilities. One recent design enables both forward- and side-imaging using one catheter [57]. This design was based on an aspheric micro-lens and a prism with the beam being scanned eccentrically (Fig. 1-1J).

Wu et al. reported forward imaging using paired angle rotation scanning (PARS) technique [75]. As shown in Fig. 1-1K, this design used two angle-cut counter-rotating GRIN lenses to deflect the beam and achieve beam scanning in the forward region [58, 75]. Also, a handheld, forward-imaging PARS OCT needle (21 gauge, 820 μm diameter) has been reported for retinal imaging [58].

Endoscopic imaging using common-path OCT has been demonstrated by Sharma and Kang [76]. One recent design used a conical tip fiber to serve as both imaging lens and self-aligning reference plane [77]. Common-path endoscopic imaging has the advantage of being insensitive to probe length, wavelengh dispersion, and polarization distortions. Therefore, it is very convenient for clinical use [78].

2. Single Fiber Delivery and Distal Actuation: For proximal actuation, the mechanical motion (either rotation or linear motion) is translated along the endoscope, which might cause friction in scanning, especially when the endoscope is bent inside the body (such as colonoscopy). Distal actuation greatly alleviates this problem by moving the device at the distal end. However, it is challenging to design a high-fidelity scanning device within small diameter. Therefore, in general, distally actuated endoscopes have larger diameter than proximally actuated endoscopes.

Boppart et al. reported a 6.4 mm diameter lead zirconate titanate (PZT) cantilever-based handheld forward-imaging probe [79]. In the design shown in Fig. 1-2A, the

PZT cantilever translated the fiber and GRIN lens assembly together to perform beam scanning. Other kinds of actuator also achieved similar scanning. Wang et al. used a low-voltage (2 V) electroactive ionic polymer-metal composite (IPMC) cantilever to actuate the fiber and GRIN lens to achieve both forward- and side-viewing imaging [80]. Low-voltage actuation ensures safety in clinical applications. Munce et al. developed an electrostatic, forward-viewing probe by placing the optical fiber and lens assembly through a platinum coil in the lumen of a dissipative polymer [81]. This probe is packaged at 2.2 mm in diameter, and driven by high voltage (1-3 kV) but at low current (~2 μA). Furthermore, the ground wire is present in the catheter itself, which minimizes the chance of delivering an electric discharge to the tissue.

Alternatively, beam scanning can be achieved by actuating the fiber tip only and relaying the scanning spot onto the tissue through the stationary GRIN lens or imaging lens (Fig. 1-2B) [79]. Sergeev et al. reported the first fiber-based, forward-imaging OCT endoscope with ~2.2 mm in diameter [82]. They used an electromechanical unit with < 5V voltage to actuate the fiber tip to perform in vivo imaging through the accessory channel of a standard endoscope. Liu et al. used a tubular PZT actuator to scan the fiber in front of a stationary GRIN lens (Fig. 1-2C) [83]. This 2.4-mm diameter endoscope utilized the resonant scanning to perform rapid lateral forward-scanning. Continuous focus tracking has been realized with lateral-priority scanning [84], and an ultrahigh transverse resolution of 4 μm can be achieved by replacing the GRIN lens with an achromatic compound lens [85].

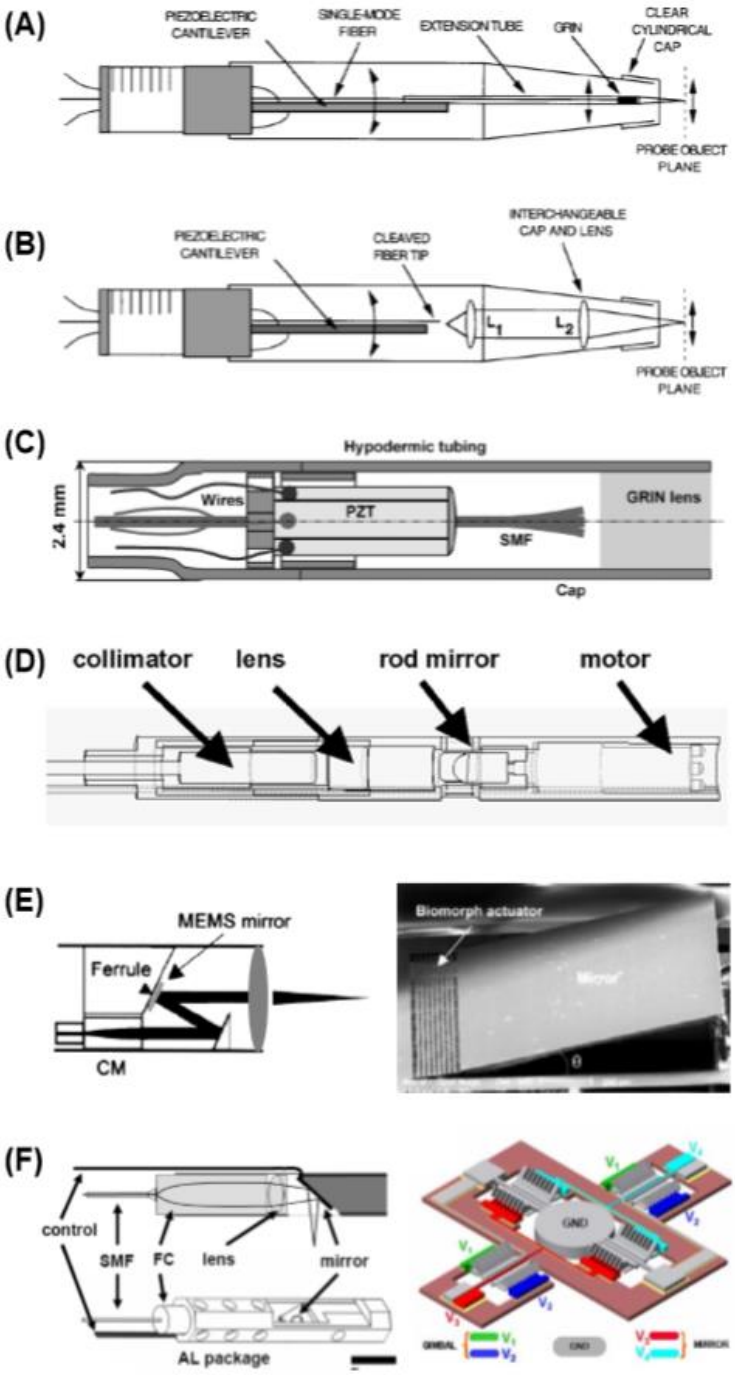

Fig. 1-2. Distal actuated OCT imaging devices.

(A) Piezoelectric (PZT) cantilever-based handheld forward-imaging probe, from Ref. [79] (B) Forward imaging by actuating the fiber tip only through the stationary imaging lens, from Ref. [79] (C) A tubular PZT actuator to scan the fiber in resonance to perform rapid lateral-priority forward-scanning, from Ref. [83] (D) Circumferential imaging using a rotary micromotor, from Ref. [86] (E) Distal beam scanning using a one-dimensional microelectromechanics (MEMS) mirror, from Ref. [87] (F) Distal beam scanning using a two-axis MEMS mirror, from Ref. [88]. The figure is reprinted from ref [59] with permission.

To perform circumferential imaging, Tran et al. [89] and Hertz et al. [86] integrated a micro-motor at the distal end of an OCT endoscope to rotate the micro-prism (or rod mirror) for circumferential scanning (Fig. 1-2D). Focus tracking can be achieved by varying the separation between the GRIN lens and the rod mirror [86]. The diameter of the reported probes were 2.4 mm and 5 mm, respectively. The size of the micromotor itself can be a limiting factor for miniaturization. In vivo 3D endoscopic OCT imaging of a rabbit esophagus and trachea were achieved by combining linear translation with a rotational micromotor [90]. By further miniaturizing the endoscope down to 1.5 mm, Su et al. recently demonstrated in vivo 3D imaging of human airway [91].

Pan et al. developed an elliptical handheld arthroscope with the long and short axes of 7.5 mm and 3 mm, respectively [92]. They used a scanning mirror at the back focal plane of imaging lens to achieve 6 mm linear scan length. Miniaturized mirror designs using either microelectromechanical systems (MEMS) or PZT technology enables further miniaturization of the endoscope. Pan et al. reported the first MEMS mirror with a bimorph thermally actuated contraction hinge (Fig. 1-2E) [87]. This forward-viewing probe enabled cross-sectional OCT imaging with 2.9 mm lateral scan range. Later, the same group modified the MEMS design to increase the scan range to 4.2 mm [93, 94]. In vivo cystoscopic OCT imaging of human bladder has been demonstrated using the MEMS-based probe with spectral domain OCT [95]. Zara et al. also reported an electrostatic MEMS scanning mirror for OCT [96]. This 2 mm x 2.25 mm mirror was resting on 3 μm thick polyimide hinges and tilted by a linear integrated force array (IFA) actuator. Later, Zara and Patterson reported using a

polyimide amplified piezoelectric bimorph scanning mirror for spectral-domain OCT imaging [97]. This device used a piezoelectric bimorph actuator to drive microfabricated polyimide structures at resonance to achieve video rate imaging of 25-41 frames/s. Chong et al. reported a novel design of optically driven MEMS scanning mirror, which eliminates directly powering up the scanning element and minimize the hazardous risks for in vivo imaging [98].

To acquire 3D OCT images, a two-axis MEMS mirror was developed. Jain et al. reported a two-axis electrothermal micromirror with 1 mm^2 mirror size for OCT imaging[99]. 3D OCT imaging using 2D MEMS mirror has subsequently been reported by several groups [100-102]. The first OCT endoscope utilizing 2D MEMS scanner was demonstrated by Jung et al. using time-domain OCT[103]. The entire endoscope had an outer diameter of < 4 mm. Later the same group developed an OCT probe with 5.5 mm in diameter using 2D MEMS mirror probe and spectral-domain OCT[104]. Aguirre et al. demonstrated a ~5 mm OCT catheter with a 1-mm in diameter two-axis scanning MEMS mirror at the distal end (Fig. 1-2F) [88]. This mirror was driven by angular vertical comb (AVC) actuators on both inner mirror axis and outer orthogonal gimbal axis. Kim et al. reported a two-axis magnetically-driven MEMS scanning catheter with 2.8 mm in diameter, which was actuated by magnetic field with low voltage (1-3 V)[105]. Other designs for two-axis MEMS scanning mirror [106] and piezoelectric scanning mirrors [107] have also been reported recently for OCT imaging.

3. Optical Relay of Scanning Beam: Another way of formulating an image is using relay optics, such as relay lens, GRIN rod lens, or fiber bundles, to translate the

scanning beam at the proximal end to the distal end. Boppart et al. demonstrated a 2.68-mm-in-diameter OCT laparoscope using a 1.5 pitch GRIN rod lens as the relay [79]. Later, Xie et al. reported a GRIN-rod-lens-based endoscope using spectral-domain OCT [108]. They used 1 pitch long GRIN rod lens with different diameters (2.7 mm and 4.5 mm, respectively) for both forward- and side-view imaging and have successfully acquired images from rabbit lung in vivo. Furthermore, high speed (500 mm/s) dynamic focusing can be achieved by changing the distance between the scan head lens and the proximal entrance surface of GRIN rod lens [108]. Long dynamic focus tracking (0-7.5 mm) can be achieved without moving the endoscope.

Relaying the image planes through the endoscope can be achieved by using a flexible fiber bundle as well. A fiber bundle consists of several tens of thousands cores to preserve the spatial relationship between the entrance and the output. In fact, flexible fiber bundles have been commonly used in standard white light endoscopy. Endoscopic OCT using fiber bundles has been demonstrated by Xie et al. [109]. Later, Han et al. also demonstrated a common-path OCT endoscope using fiber bundle [110]. Different performances of focusing systems (bulk lens, GRIN lens, and microlens array) associated with fiber bundle endoscope have been investigated by the same group as well [111].

Table 1-1. The imaging performance of endoscopic OCT.

Ref	Resolution (μm)		Working Distance (mm)	Image Configuration	Image Formation	Speed	Diameter (mm)
	Lateral	Axial					
[[50]]	38	20	2.5	C	P	1 rpm	1.1
[[60]]	17	6.7	0.08	C	P	NA	0.4
[[89]]	13	9.5*	2	C	D	1 kHz	2.4
[[86]]	8	5	variable	C	D	2 kHz	5
[[63]]	15	5	0.5	S/CP	P	~3 kHz	1.5
[[51]]	30	9.3	0.7	S	P	1.7 kHz	NA
[[62]]	NA	13	NA	S	P	8 kHz	2
[[64]]	18	16	0.3	S	P	14 Hz	2
[[52]]	26	13	0.35	S	P	4.8 kHz	0.9
[[54]]	10	2.4	0.3	S	P	20 kHz	2
[[53]]	4.4	3.2	0.2	S	P	250 Hz	2
[[74]]	< 10	7.4	0.125 0.375 0.625 [a]	S	P	~4.4 kHz *	5.6
[[65]]	9	5-7	NA	CP	P	100 kHz	0.83
[[55]]	39	12	~ 9	CP	P	12 kHz	1.3
[[70]]	21.2	10.2	~ 11	CP	P	40 kHz	1.3
[[90]]	20	8	NA	CP	D&P	20 kHz	2.7
[[91]]	20	8	NA	CP	D&P	20 kHz [b]	2.2
[[66]]	30	9.3	~ 9	CP	P	10 kHz	1.5

Table 1-1 (Cont.)

Ref	Resolution (μm)		Working Distance (mm)	Image Configuration	Image Formation	Speed	Diameter (mm)
	Lateral	Axial					
[[88]]	12	< 4	2	S-2D	D	2 kHz	5
[[73]]	NA	16	~ 1 – 7 / ~ 4 – 8	S	D&P	NA	4
[[83]]	16	25	3.5	F	D	2.8 kHz	2.4
[[82]]	20	10*	5-7	F	D	200 Hz	> 2
[[87]]	20	10	NA	F	D	2.4 kHz	5
[[81]]	NA	7.4	NA	F	D	43 kHz	2.2
[[75]]	10.3-12.5	9.3	1.4	F	P	250 Hz	1.65
[[58]]	7.6-10.4	10.5	0.78	F	P	250 Hz	0.82
[[57]]	23	18.2	5	F&S	P	19 kHz	2.6
[[79]]	33	12	5	F	G	NA	> 2.68
[[108]]	10	10	1 - 8.5	F/S	G	4 kHz *	2.7/4.6
[[92]]	17	10	NA	F	L	2.4 kHz	7.5*3 (oval)
[[109]]	12	10	NA	F	FB	NA	3.2
[[112]]	< 2	< 4	0.7	F-2D	D	4 frames/s	8

[a] muti-channel probe; [b] real time displaying speed; &: and; /: or; NA: Not available; *: Estimated using OCT system parameters; C: Circumferential scan; S: Side-imaging linear scan; CP: Circumferential with pull back scan; S-2D: Side-viewing two dimensional scan; F: Forward-viewing linear scan; F-2D: Forward-viewing 2D scan. P: Proximal actuation; D: Distal actuation; G: Grin Rod Lens; L: Lens; FB: Fiber bundle. The table is reprinted from ref [59] with permission.

Table **1-1** summarizes several key design parameters, such as resolution, working distance, image configuration, image formation, speed, and endoscope diameter for selected endoscopic OCT devices reported in the literature. In general, the diameters for the proximal actuated endoscopic OCT devices are typically smaller than those with distal actuation. Overall, endoscopic OCT can achieve micron level image resolution, thereby enabling visualization of tissue microstructures in vivo.

1.3.4 Intra-operative MRI for neurosurgery

Intra-operative MRI (iMRI), which allows surgeons to address the brain shift issue, is gaining popularity and has been applied to many stereotactic neurosurgeries, including brain tumor biopsy [113], catheterization [114] and deep brain stimulation [115]. Beside the excellent soft tissue discrimination and 3D visualization, high field (> 1.5 T) MRI can also perform a wide range of adjunctive imaging protocols, such as MR angiography that can potentially reduce the risk of hemorrhage and MR tractography that can locate specific white matter (WM) tracts. However, iMRI procedures still suffer from low spatial resolution and slow imaging speed. It takes several minutes to obtain one high resolution image (~ 1 mm), which cannot resolve small targets, such as subthalamic nucleus, for DBS surgery. It is also expensive and not ready for widespread use [116]. The MRI compatibility of the surgical tools also raises safety concerns. For example, in DBS surgery, the magnetic field may generate unwanted ablation and induced stimulation surrounding the electrodes [117]. Therefore, developing a cheaper and safer navigation technology with higher resolution is still an unmet clinical challenge.

1.3.5 Transcranial sonography

Transcranial sonography, which provides real-time intraoperative guidance, has started to be used in clinics [118, 119]. Comparing with iMRI, it is cost-effective, compatible with conventional surgical tools and provides full access to the patient during imaging. Doppler sonography is also available to prevent severe hemorrhage. However, depending on the echogenicity of brain structures, sonography may not provide direct visualization of targets and surgeons can only infer the location of targets from their neighboring structures [119]. The anatomical variability of the targets relative to neighboring structures may introduce inaccuracy and need to be carefully correlated by other imaging modalities. Also, in DBS surgery, the metallic electrodes would introduce echogenic artifact of tip diameter (0.1-1.5mm, depending on system parameters), which also need to be calibrated when interpreting the tip location [118]. The imaging quality depends on the skull thickness, which limits assessment of brain structures in about 10% of elderly whites [120]. Transcranial sonography, which provides large FOV and real-time imaging guidance may be a less demanding and cheaper alternative to iMRI. However, due to the limitations of resolution and contrast, it is necessary to use this technology with other refinement technology for precise guidance.

1.3.6 Optical intra-cerebral measurement

Near infrared (NIR) optical reflectance is capable of detecting gray/white matter transition and thus is useful to localize the gray matter (GM) nuclei surrounded by white matter (WM) lamina. The optical signal can be delivered and collected by thin optical fibers. Therefore it can be integrated with other targeting tools, such as a

microelectrode [121] and an electrical impedance probe[122]. The diffusive NIR signal recorded along the trajectories of 200 DBS implantation procedures, shows high sensitivity (98% thalamus, 88% STN) and specificity (100% thalamus and 79% STN) for brain nuclei detection[121]. However, in the case of inaccurate targeting caused by brain shifting, low negative predictive values (50% thalamus and 76% STN) reflect the challenge of judging if the target is missed. The NIR signal is also suitable for monitoring local blood perfusion and thus has potential to avoid hemorrhage. A study showed that laser Doppler perfusion monitoring (LDPM) has higher signal when the probe is close to a vessel and it is also capable of detecting pulsatile flow[123]. However, the detection of vessels neighboring the probe which are not in the direct path of an advancing surgical probe can provide a false-positive when the goal is to detect at-risk blood vessels. In fact, the same vessel was detected on both advancing and withdrawing process[123]. Therefore, we need to improve the spatial resolution of LDPM for rejecting the neighboring vessels and detecting the at-risk vessels in front of the advancing surgical tool.

1.4 Scope of Dissertation

The major limitation to an efficient, safe and accurate stereotactic neurosurgery is the lack of high-resolution and real-time imaging feedback in front of the advancing instruments. High resolution imaging feedback that is capable of detecting micro-landmarks is especially important for localizing mm or sub-mm brain targets. Furthermore, real-time feedback is necessary to avoid damaging at-risk blood vessels in front of advancing instruments.

Microelectrode recording (MER, section 1.2.2) is the current gold standard for locating deep brain targets, but it only provides feedback from brain nuclei and thus cannot be used to prevent hemorrhage or locate neural fiber tracks. Moreover, the mapping process usually takes several hours. On the other hand, intra-operative MRI (iMRI, section 1.3.4) imaging is gaining popularity for neurosurgery due to its great soft tissue contrast and volumetric 3D visualization. However, long exposure time (tens of minutes) and millimeter resolution make it difficult to use iMRI for real-time, high precision guidance.

Optical coherence interferometry in combination with miniature optical components has great potential for real-time and high-resolution guidance and only optical guidance can fulfill these two criteria simultaneously. Other imaging modalities, such as ultrasound, MRI or CT, do not have sufficient spatial and temporal resolution to overcome these challenges. Due to short optical wavelength (around 1 μm), the resolution (linearly proportional to the wavelength) of optical imaging can easily reach sub- 100 μm (~ 10 μm). Moreover, real-time imaging is achievable due to the ultra-short response time of optoelectonics detectors (~10 ns). However, one major barrier of using scattering based optical imaging is that signals from different depths are overlaid preventing imaging beyond superficial surface. The development of optical coherence tomography [124] using optical coherence interferometry solves this problem (please see details in chapter 2.1). By combining reference and sample arm signals, information from different depths can be resolved. With depth-resolved, micron-level and real-time imaging capabilities, OCT is used in many medical fields including: ophthalmology, cardiology and Barrett's esophagus

screening. Besides imaging, optical coherence interferometry can also be used as a sensor, which provides feedback from flowing blood cells. A simple optical sensor provides better cost to benefit ratio in some medical conditions. For example, if only the presence of an artery directly in front of the instrument needs to be detected, and the size of the vessel is unimportant, the sensor which has much smaller size (0.1 mm vs 1 mm) and lower system cost (3000 vs 30,000 USD) will be a better option compared to imaging optics.

In this dissertation, three optical intra-operative guidance tools which provide real-time and high-resolution feedback are developed for neurosurgery. These three translational devices include one transformative device and two complementary technologies for improving the current systems, iMRI and MER.

In chapter 3, development of a transformative OCT imaging device for neurosurgery guidance is described. The forwarding-imaging needle-type OCT probe that is capable of detecting micro-landmarks and Doppler flow in front of the needle in real time is a promising translational device for neurosurgery guidance. The feasibility studies and the performance tests have been performed on in vivo large animals.

In chapter 4, the integration of OCT imaging and iMRI is discussed. The combination of high-resolution and real-time optical imaging with MRI improves the accuracy of iMRI procedures by two orders (from 1mm to 0.01 mm). Moreover, OCT provides a different contrast which enhances the detection of MRI-occult tissue landmarks. These improvements will facilitate the capabilities of iMRI for high precision neurosurgery.

In chapter 5, a complimentary fiber sensor is developed to improve the safety of MER. MER is the current gold standard for locating deep brain nuclei, but it increases the risk of disastrous intracranial hemorrhage (section 1.2.1). The thin (0.125 mm) optical fiber sensor that is capable of detecting Doppler flow in front and providing real-time audio feedback can be integrated with MER electrodes to avoid hemorrhage. The feasibility studies and validation have been performed on in vivo larger animals.

Besides neurosurgery, real-time, non-labeling and high-resolution imaging is also a powerful tool for preclinical animal studies. Versatile OCT imaging protocols are designed to extract various physiological parameters simultaneously without injecting contrast dye. In chapter 6, we report the results of using OCT, Doppler OCT and speckle variance (please see details in chapter 2) simultaneously to monitor hemodynamic changes during an anti-cancer therapy, photo-immunotherapy. Versatile protocols not only enable measurement of tissue scattering, blood flow and vessel lumen size simultaneously, but also reduce motion artifacts.

Lastly, in chapter 7, the novelty and impact of each device is concluded. The limitations of each technology are discussed and the future improvements are suggested. Since the devices developed here are platform technologies, other potential applications will also be discussed in chapter 7.

Chapter 2: Optical coherence interferometry for imaging and sensing

Optical coherence interferometry that is capable of resolving sub-surface tissue structure and detecting cell motion in real time without contrast agent is gaining popularity in biomedical imaging and sensing. In this work, we will use optical coherence interferometry for surgical guidance and intra-vital animal imaging. Physics principle of optical coherence interferometry is introduced in this chapter.

2.1 OCT

Optical Coherence Tomography is an imaging modality capable of providing cross-sectional imaging of biology tissue with micrometer resolution in situ and in real time. How different OCT systems resolve the information from different depth by using the coherence property of light are introduced in this section.

2.1.1 Michelson Interferometer

It is important study Michelson interferometry with a monochromatic light source before we discuss OCT systems. Fig. 2-1 shows the schematic of a Michelson interferometer. When the monochromatic light reaches the beam splitter, some photons will travel to the reference arm and others will travel to the sample. The back scattering light from the sample E_S and the reflected light from the reference mirror E_R will be recombined on the detector. E_S and E_R can be expressed in phasor form such that:

$$E_S = E_s * e^{-i(2kl_s - \omega t)}, \quad E_R = E_r * e^{-i(2kl_r - \omega t)}$$

Here k is angular wavenumber and the factor of 2 arises due to the roundtrip propagation. l_s and l_r represent the optical path length of sample arm and reference arm respectively. ω is the angular frequency.

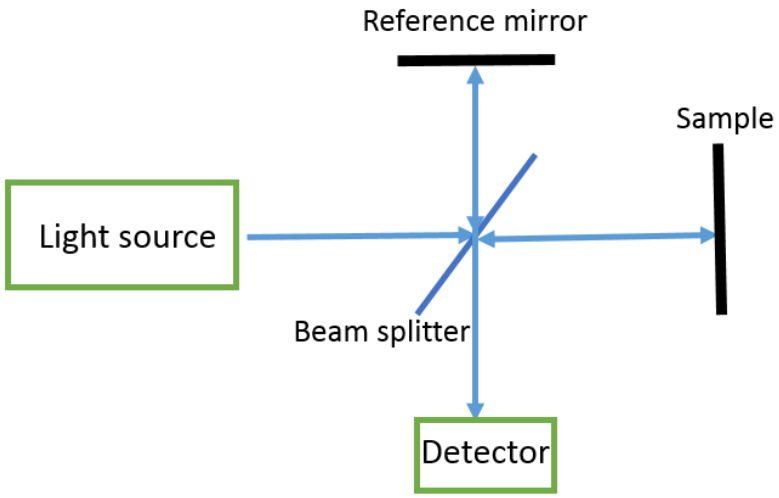

Fig. 2-1. Michelson Interferometry

The detector current I_d is linearly proportional to the energy density contributed from bother sample and reference arm:

$$I_d \sim |E_r + E_s|^2 = |E_r|^2 + |E_s|^2 + 2 * \mathrm{Re}(E_r E_s^*)$$

$$= |E_r|^2 + |E_s|^2 + 2 * \mathrm{Re}\left(E_r E_s e^{-i(k*2(l_s - l_r))}\right)$$

$$= |E_r|^2 + |E_s|^2 + 2 * E_r E_s * \cos(k * 2(l_s - l_r))$$

The first two terms are DC terms, which represent the power reflected back from the reference arm and sample arm respectively. The Last term is an interference AC term and its intensity depends on the optical path length difference between two arms. The interference current reaches its maximum (constructive interference) if the path length difference, $2(l_s - l_r)$, is equal to the integer number of wavelength. It is on

minimum (destructive interference) if the path length difference is equal to the integer number of half wavelength.

2.1.2 Time domain OCT

The basic structure of time domain OCT (TD-OCT) is a Michelson interferometer with a broad band (low coherence) light source (Fig. 2-2). With a monochromatic light source, the electromagnetic (EM) waves from two arms can interfere with each other no matter how big is the path length difference. However, EM waves can only interfere with each other within a very short range with a broad band light source. The signal from other region will be rejected (coherence gating) [125]. Therefore, we can obtain a depth-resolved tomography by scanning the reference mirror. In this section, we will discuss how a broadband light source provides the sectioning capability.

With a broad band light source, E_S and E_R will contain multiple frequency components and can be expressed as:

$$E_S = \int E_s(\omega) * e^{-i(2kl_s-\omega t)} d\omega, \quad E_R = \int E_r(\omega) * e^{-i(2kl_r-\omega t)} d\omega$$

And the AC term of the detector current becomes:

$$I_{d,AC} \sim Re(E_r E_s^*) = Re\left(\iint E_r(\omega')E_s(\omega) * e^{-i(2k'l_r-\omega' t)} * e^{-i(-2kl_r+\omega t)} d\omega' d\omega\right)$$

$$= Re\left(\iint E_r(\omega')E_s(\omega) * e^{-i(2k'l_r-2kl_s)} * e^{-i(\omega-\omega')t} d\omega' d\omega\right)$$

Because the detector response time (10^{-6}s) is much longer than the period of EM wave oscillation (10^{-14} s), collecting data from a detector is equal to integrate the above equation over time:

$$I_{d,AC} \sim Re\left(\iiint E_r(\omega')E_s(\omega) * e^{-i(2k'l_r-2kl_s)} * e^{-i(\omega-\omega')t} dt\, d\omega' d\omega\right)$$

Since $\int e^{-i(\omega-\omega')t}dt = 2\pi\delta(\omega-\omega')$, we can simplify the above equation to:

$$I_{d,AC}\sim Re\left(\int E_r(\omega)E_s(\omega) * e^{-i(2kl_r-2kl_s)}\, d\omega\right)$$

If we assume the power spectrum form the sample and reference are equal to a fraction of source power spectrum $P(\omega)$,

$$E_0(\omega)^2 = P(\omega)$$

$$E_r(\omega) = \sqrt{P_r E_0(\omega)^2}$$

$$E_s(\omega) = \sqrt{P_s E_0(\omega)^2}$$

Substituting above equations to the interference AC signal results in:

$$I_{d,AC}\sim Re\left(\sqrt{P_r P_s}\int E_0(\omega)^2 * e^{-i(2kl_r-2kl_s)}\, d\omega\right);$$

If power spectrum $E_0(\omega)^2$ is a rectangular function (Fig. 2-2B):

$$E_0(\omega)^2 = P(\omega) = P_0 * rec(\frac{\omega-\omega_0}{\Delta\omega})$$

The interference AC signal will be:

$$I_{d,AC}\sim Re\left(\sqrt{P_r P_s}\int P_0 * rec(\frac{\omega-\omega_0}{\Delta\omega}) * e^{-i\frac{\omega(2l_r-2l_s)}{c}}\, d\omega\right)$$

$$= Re\left(\sqrt{P_r P_s}\int P_0 * rec(\frac{\omega-\omega_0}{\Delta\omega}) * e^{-i\omega\tau}\, d\omega\right)$$

where $\tau = \frac{(2l_r-2l_s)}{c}$. The equation above shows that the AC term of detection current is equivalent to the Fourier transform of the source power spectrum $P(\omega)$ and is equal to:

$$I_{d,AC}\sim Re\left(\sqrt{P_r P_s}P_0 * \Delta\omega * e^{-i\omega_0\tau} * sinc(\frac{\tau}{2\pi/\Delta\omega})\right)$$

Since $P_0 * \Delta\omega$ is equal to the total energy (Fig. 2-2B), P_t, the equation can be rewritten as:

$$I_{d,AC} \sim \sqrt{P_r P_s} P_t * \mathrm{sinc}\left(\frac{\tau}{2\pi/\Delta\omega}\right) * \cos(\omega_0 \tau)$$

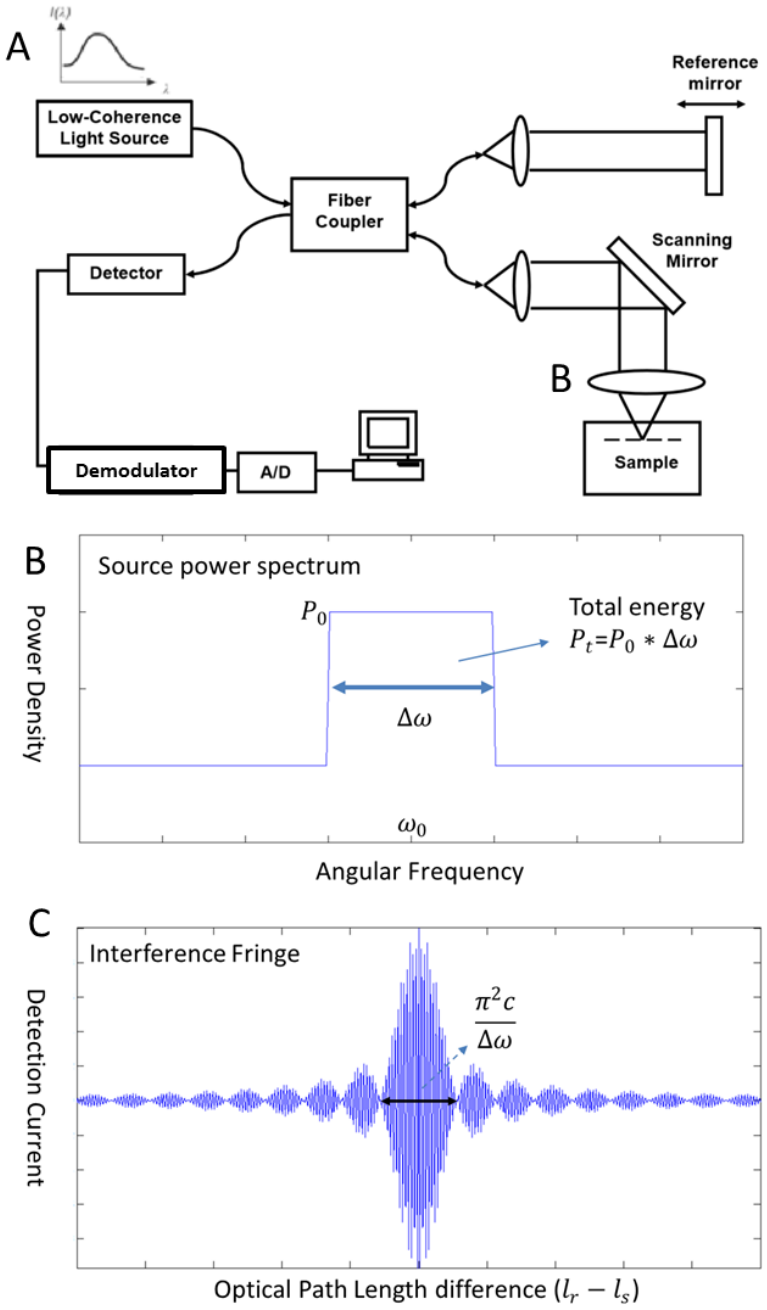

Fig. 2-2. Time domain OCT

(A) Time domain OCT System. From ref [59] with permission. (B) Power spectrum of light source. (C) The interference fringe on the detector.

This equation shows that the interference fringe will decay when τ (linear proportion to path length difference, $2l_r - 2l_s$) is away from zero (Fig. 2-2C). In other words, the back scattering signal from the sample that has big optical path length difference relative to the reference arm will be rejected. The equation above agrees with the equation reported in literature [126]. We can estimate the axial resolution by calculating the distance between the first zero points. When $\frac{\tau}{2\pi/\Delta\omega} = \pm\frac{\pi}{2}$, $I_{d,AC} = 0$. Therefore, if

$$\tau = \pm\frac{\pi^2}{\Delta\omega}, I_{d,AC} = 0$$

$$l_r - l_s = \pm\frac{\pi^2 c}{2\Delta\omega} = \pm\frac{\pi\lambda^2}{4\Delta\lambda}, I_{d,AC} = 0.$$

The estimated axial resolution is equal to $\frac{\pi\lambda^2}{2\Delta\lambda}$. Broader spectrum band width provides better axial resolution.

Fig. 2-2A shows the schematic of time domain OCT system. It contains a low coherence light source (Fig. 2-2B) and a Michelson interferometry. The reference mirror is mechanically scanned back and forth, and the interference signal is measured by a photodiode detector. Optical interference between the light from the sample and reference mirror occurs only when the optical distances between sample and reference paths within the coherence length $\frac{\pi\lambda^2}{2\Delta\lambda}$ (Fig. 2-2C). Sample signals from other regions are rejected. By translating the reference mirror, the axial profile of sample's reflectivity can be generated. If power spectrum is a Gaussian function, the axial resolution will be $\frac{2\ln 2*\lambda^2}{\pi\Delta\lambda}$. If central wavelength $\lambda = 1310$ nm and

bandwidth $\Delta\lambda = 100\,\mathrm{nm}$, the axial resolution will be 7.6 μm. This resolution is higher than conventional ultrasound, MRI and CT imaging.

2.1.3 Fourier domain OCT

Besides TD-OCT, there is another type of OCT system, Fourier-domain OCT (FD-OCT), which has better sensitivity and faster imaging speed [127-129]. In FD-OCT, the reference path is kept at one fixed distance and the spectrum of the interference signal is acquired. The axial profile is generated by Fourier transformation of the interference fringe in k space. FD-OCT imaging can be performed in two ways, typically referred to as "swept-source OCT (SS-OCT)" and "spectral-domain OCT (SD-OCT)."

Fig. 2-3 shows a SS-OCT system. It consists of a wavelength-swept light source and a Michelson interferometer. From section 2.1.1, we know that the detector current I_d is equal to:

$$I_d \sim |E_r|^2 + |E_s|^2 + 2 * E_r E_s * \cos(k * 2(l_s - l_r))$$

$$= I_r + I_s + 2\sqrt{I_r I_s} * \cos(k * 2(l_s - l_r))$$

This equation shows that the interference term of I_d is a cosine function of wavenumber k and $k = \frac{2\pi}{\lambda}$ (Fig. 2-3B & C). Since wavelength swept light source generates an EM wave with a specific wavenumber at a time, recording the detector current in time is equal to record the current in k space (Fig. 2-3B & C). Fig. 2-3B and C shows that the interval between two peaks of detector current in k space is inversely proportional to the path length difference. Therefore if path length

difference is small, the frequency of interference fringe in k space will be low (Fig. 2-3B).

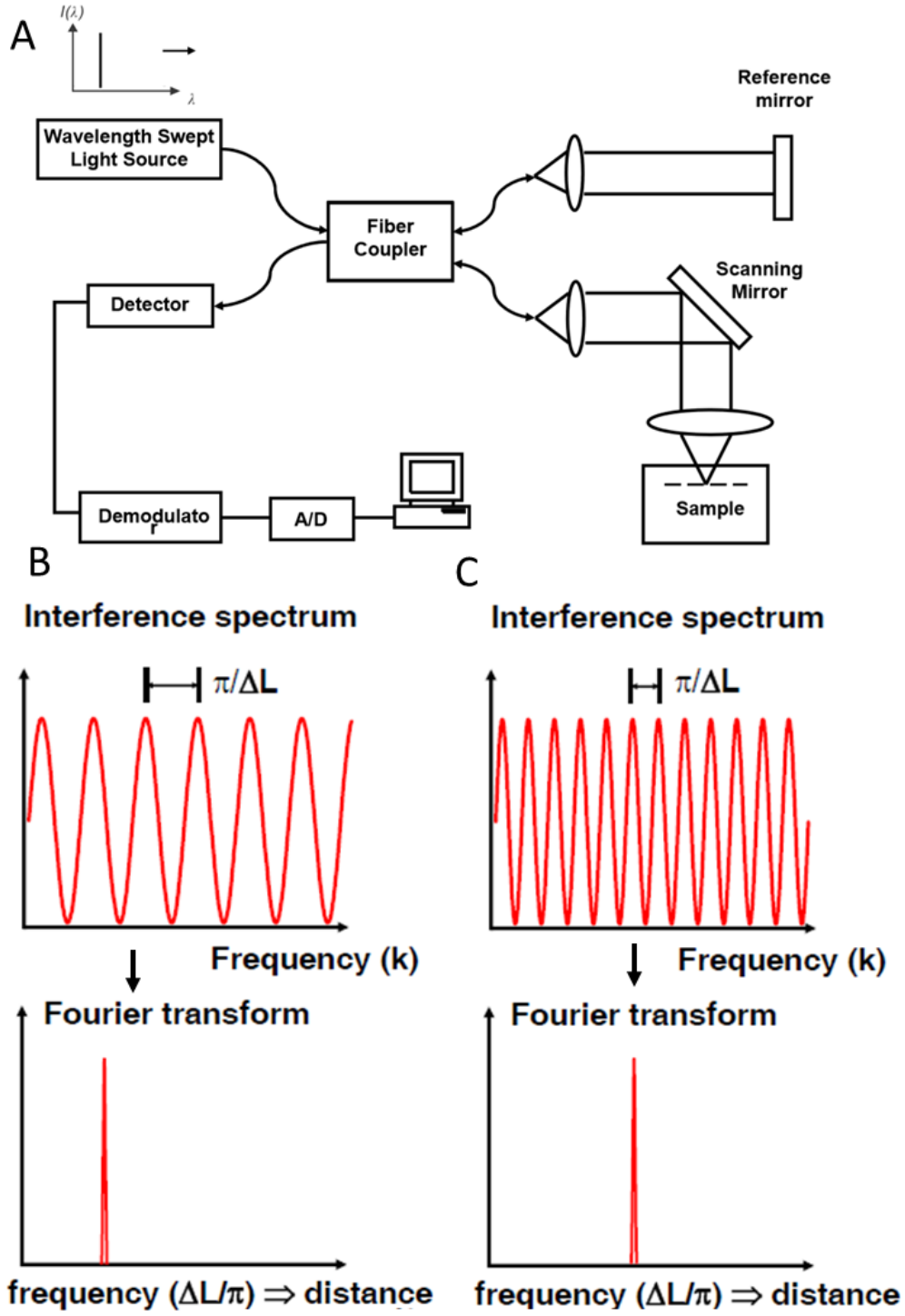

Fig. 2-3. SS-OCT system

(A) Schematic of a SS-OCT system. From ref [59] with permission. (B) Interference fringe from a shallow axial position. (C) Interference fringe from a deep axial position.

On the other hand, if the sample back scattering signal is from a deep axial position (large path length difference), the frequency of detector current in k space will be high (Fig. 2-3C). Therefore, a depth profile of the sample can be obtained by performing Fourier transformation of detector current in k space (in time).

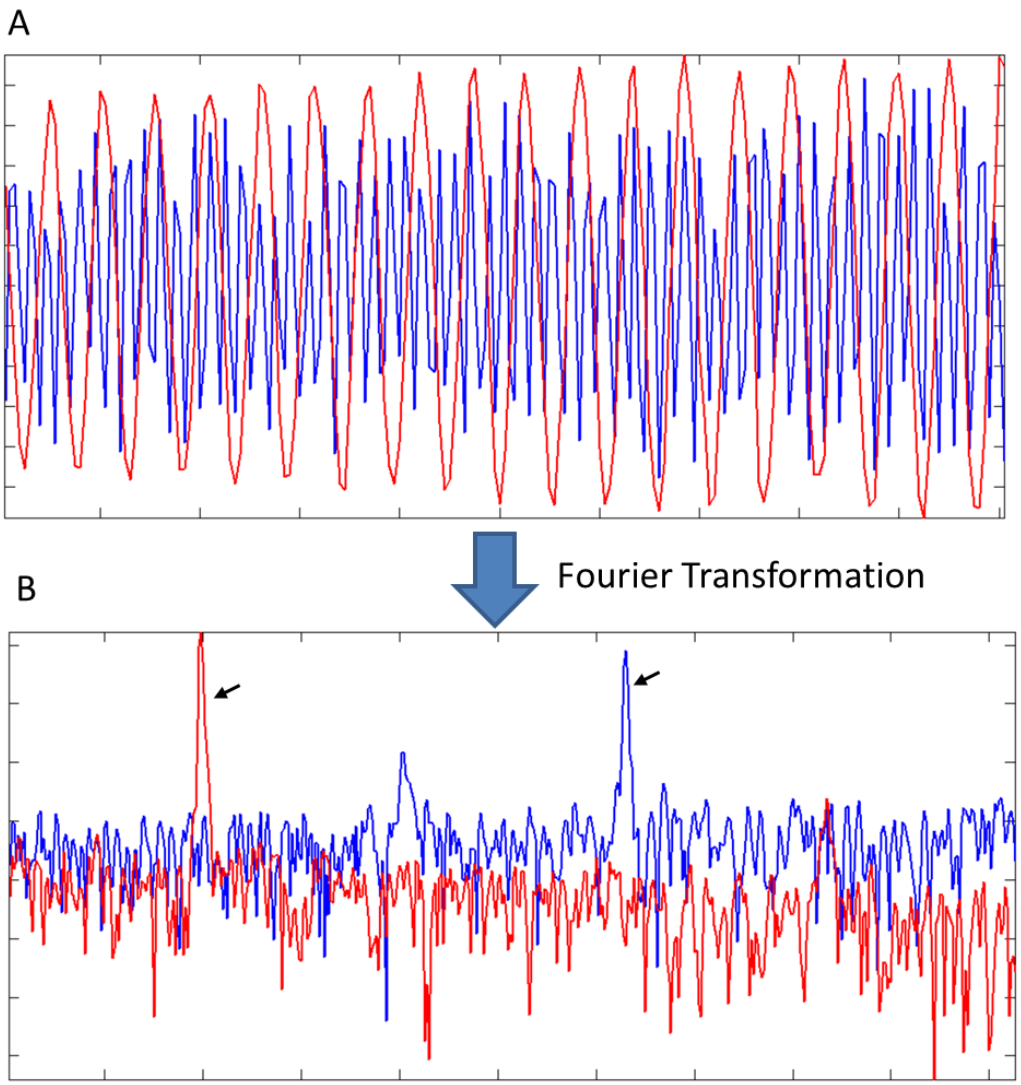

Fig. 2-4. Interference fringes of SS-OCT system.

(A) Measured interference fringe from two locations: red line form a shallower position and blue line from a deeper position. (B) Fourier transformation of the interference fringes. Black arrows indicate strong reflection from two different locations.

Fig. 2-4A shows measured interference fringes. The red line is from a reflective surface at shallower axial position and blue line is from a deeper position. As discussed above, the red line has lower frequency than the blue line. The location of reflective surface can be easily identified after Fourier transformation (Fig. 2-4B, black arrows). This measurement can also be used to quantify the pixel size and the axial resolution. If the distance (1.25 mm) and the number of pixels (216 pixels) between reflective interfaces are known, the pixel size can be calculated (5.8 μm per pixel). Furthermore, the axial resolution can also be measured by calculating number of pixels between 3dB decay points from the peak. The 3dB width in our measurement is two pixels and thus the axial resolution is 11.6 μm.

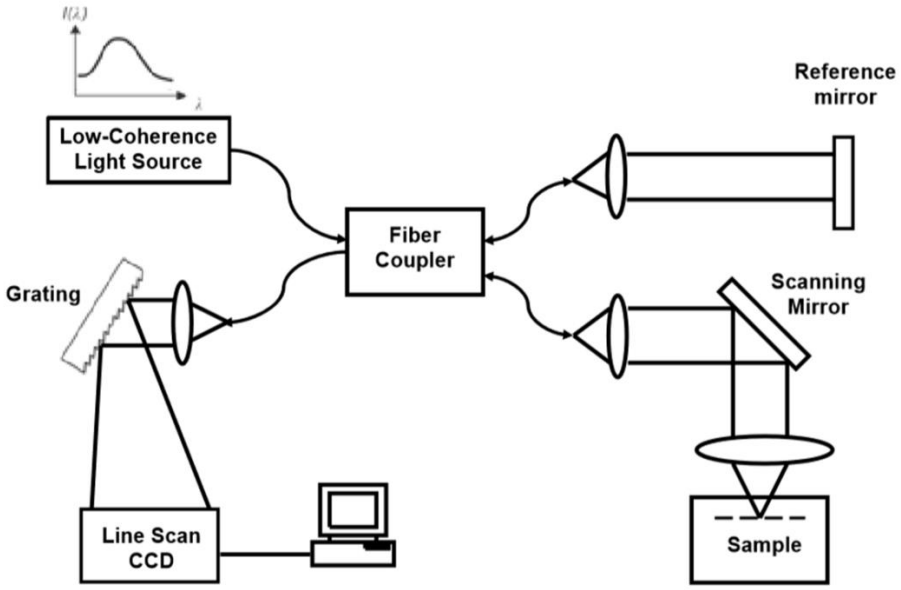

Fig. 2-5. SD-OCT system.

From ref [59] with permission.

Similar to SS-OCT system, SDOCT system resolves the depth information by Fourier transformation of interference fringe in k space (Fig. 2-3B & C). However, SD-OCT uses a different approach to obtain the interference spectrum. SD-OCT

system consists of a broad band light source and a spectrometer for detection (Fig. 2-5). Unlike SS-OCT system, which separates wavenumbers in time, the broad band light source sends EM waves with different wavenumber all together into the system, and then the information corresponding to different wavenumber k are diffracted by a grating to different spatial location and then recorded by an array CCD. The interference spectrum in k space is translated into spatial space in SD-OCT system. Then, Fourier transformation of the interference spectrum will give us the depth-resolved sample profile.

2.1.4 FD-OCT vs. TD-OCT

FD-OCT has two advantages over TD-OCT: faster imaging speed and superior sensitivity. Each axial pixel in TD-OCT is acquired only at the time when the reference mirror scans through the equidistant point in the reference arm, but in FD-OCT, all axial pixels are acquired at the same time with a static reference mirror. Therefore, FD-OCT has 10-100 fold increase in imaging speed compared to TD-OCT.

In this section, we will calculate and compare the sensitivity of TD-OCT and FD-OCT to demonstrate that FDOCT is intrinsically more sensitive than TD-OCT. From the discussion in section 2.1.2, we can derive the total detected power, P_d, in TD-OCT system:

$$P_d = P_R + P_S + 2\sqrt{P_R P_S} * \mathrm{sinc}\left(\frac{\tau}{2\pi/\Delta\omega}\right) * \cos(\omega_0 \tau)$$

If total scanning range of reference mirror is x_t and total scan time duration is T, TD-OCT system will spend a duration of $\frac{l_c}{x_t}T$ (l_c is the coherence length of the light source) at any given interface within the sample. Therefore, total number of

interference photons collected from this interface when the reference mirror is at equidistance point ($\tau = 0$) will be:

$$\text{Signal}_{\text{TDOCT}} = 2\sqrt{P_R P_S} * \frac{l_c T}{x_t} * \frac{\varepsilon}{h\upsilon}$$

where ε is quantum efficiency of the detector and $h\upsilon$ is quantum energy of a single photon. The shot noise is given by the square root of the total photon counts that are detected during that time duration. Since the total power $P_d$is dominated by the reference power P_R, the noise of TD-OCT is:

$$\text{Noise}_{\text{TDOCT}} = \sqrt{P_R * \frac{l_c T}{x_t} * \frac{\varepsilon}{h\upsilon}}$$

Thus, the signal to noise ratio of TD-OCT [126] is:

$$\text{SNR}_{\text{TDOCT}} = 10\log\left(\frac{\text{Signal}_{\text{TDOCT}}}{\text{Noise}_{\text{TDOCT}}}\right)^2$$

$$= 10\log\left(4 * P_s * \frac{l_c T}{x_t} * \frac{\varepsilon}{h\upsilon}\right)$$

On the other hand, the detected power of FD-OCT system corresponding to a specific wavenumber is

$$P_d(k) = P_r(k) + P_s(k) + 2\sqrt{P_r(k)P_S(k)} * \cos(k * 2(l_s - l_r))$$

In the following context, we will just discuss the SD-OCT system for simplicity. If we integrate the detected power over wavenumber in SD-OCT, we will obtain the total detected power same as in the TD-OCT system:

$$P_d = P_R + P_S + 2\sqrt{P_R P_S} * \text{sinc}\left(\frac{\tau}{2\pi/\Delta\omega}\right) * \cos(\omega_0 \tau)$$

This is not surprising; because the only major difference between SD-OCT system and TD-OCT system is the detection system. The detection system in SD-OCT diffracts the energy corresponding to different wavenumbers into different CCD pixels. Therefore, the integration over wavenumbers yields the same result. However, the exposure time in two system that contributes to the signal photon count are very different. In time domain system, the signal from a given sample interface is collected within the duration $(\frac{l_c}{x_t}T)$ while the reference mirror is at an equidistance point. In SD-OCT system, however, the signal is collected within the entire scan time duration (T). Therefore, we get:

$$\text{Signal}_{\text{SDOCT}} = 2\sqrt{P_R P_S} * T * \frac{\varepsilon}{h\upsilon}$$

$$\text{Noise}_{\text{SDOCT}} = \sqrt{P_R * T * \frac{\varepsilon}{h\upsilon}}$$

Subsequently, we obtain a SNR measure of SD-OCT [126]:

$$\text{SNR}_{\text{SDOCT}} = 10\log\left(\frac{\text{Signal}_{\text{TDOCT}}}{\text{Noise}_{\text{TDOCT}}}\right)^2$$

$$= 10\log\left(4 * P_s * T * \frac{\varepsilon}{h\upsilon}\right)$$

$$= \text{SNR}_{\text{TDOCT}} + 10\log\left(\frac{x_t}{l_c}\right)$$

Therefore:

$$\text{SNR}_{\text{TDOCT}} = \text{SNR}_{\text{SDOCT}} - 10\log\left(\frac{x_t}{l_c}\right)$$

In the case that x_t is 2 mm and l_c is 10 μm, we will get:

$$\text{SNR}_{\text{TDOCT}} = \text{SNR}_{\text{SDOCT}} - 23\ \text{dB}$$

A SD-OCT system is intrinsically more sensitive than a TD-OCT system (> 23 dB). This improvement is attributable to the fact that SD-OCT is capable of collecting information from all depth during the entire acquisition time.

2.2 Laser Doppler flowmetry

Besides structural information, optical coherence interferometry can also be used to obtain functional blood flow information. Fig. 2-6A shows the basic principle of Laser Doppler flowmetry (LDF). The light source generates photons with long coherence length, which means two photons can interfere with each other after travelling long separation distance. The coherence length l_c is inversely proportional to the wavelength bandwidth of light source $\Delta\lambda$:

$$l_c = \frac{\pi}{\Delta k}$$

$$= \frac{\lambda^2}{2\Delta\lambda}$$

If $\lambda = 1300$ nm and $\Delta\lambda = 0.5$ nm, the coherence length l_c will be 1.69 mm. If the separation between two light sources is not over 1.69 mm, EM waves can interfere with each other. When the photons reach the biology sample, some will interact with static tissues and bounce back into the system with no shift on the frequency (Non Doppler-shifted photons). On the other hand, some will interact with moving blood cells and have higher or lower frequency shift after the interaction (Doppler shifted-photons). If we recombine the Doppler-shifted with non-shifted photons on the detector, an interference fringe with the frequency proportional to the moving speed of blood cells will be generated. Fig. 2-6D models the interference between shifted and non-shifted photons.

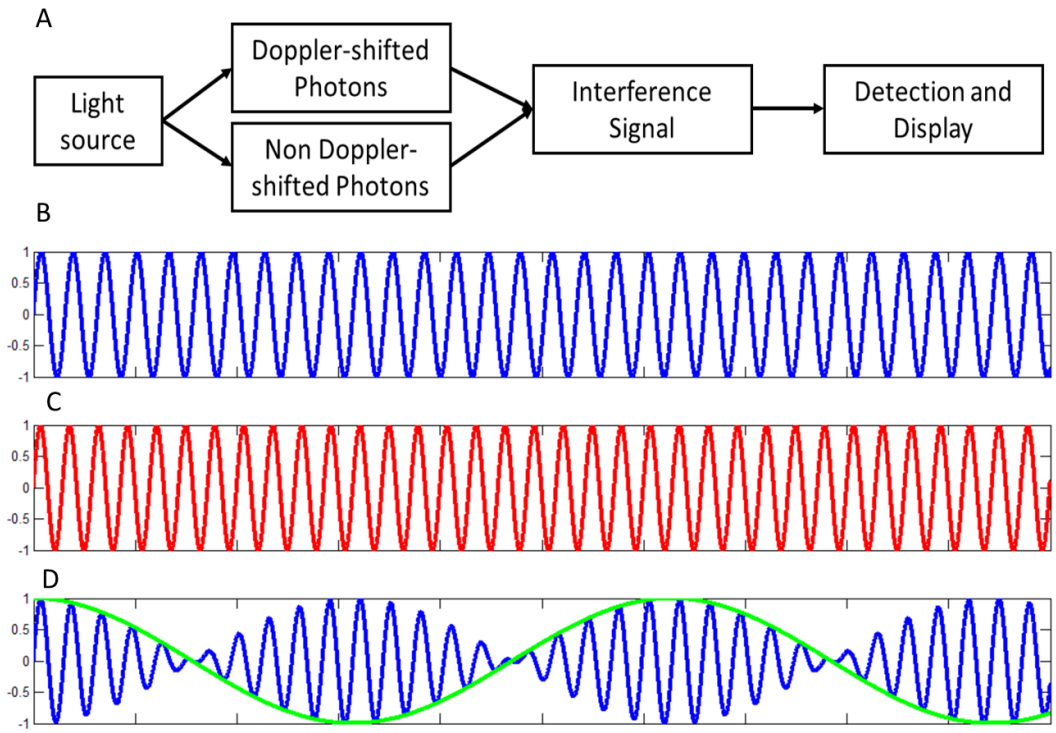

Fig. 2-6. Principle of Laser Doppler flowmetry.

(A) Principle of Laser Doppler flowmetry. (B) Non-shifted EM wave. (C) Frequency shifted EM wave. (D) Interference of Doppler-shifted and non-shifted EM waves. The green envelope illustrates the slow frequency component.

Fig. 2-6B shows a non-shifted EM wave (frequency F_0). Fig. 2-6C shows a Doppler shifted EM wave with higher frequency, $F_0 + dF$. Fig. 2-6D shows the result of combing two signals. The interference signal has two frequency components: $F_0 + \frac{dF}{2}$ and $\frac{dF}{2}$. The green envelope in Fig. 2-6D shows the slow frequency components ($\frac{dF}{2}$) and the blue line shows the high frequency components ($F_0 + \frac{dF}{2}$). Since F_0 of a conventional laser (wavelength between 400-1500 nm) is too fast ($3*10^{14}$ Hz for 1 μm wavelegth) to be measured by an optoelectronic detector, the only detectable signal is the slow signal (the green envelope). The detector current is linear proportional to the square of the interference signal (Fig. 2-6D) and thus the frequency of detector current, F_s, is:

$$F_s = 2 * \frac{dF}{2} = dF = \frac{2 * V}{\lambda}$$

V is the effective moving speed parallel to the illumination direction and λ is the wavelength of light source. In conclusion, LDF sends coherent photons into tissues and then recombine the Doppler shifted photons with non-shifted photons on the detector. On the detector, an interference fringe is recorded. The envelope of interference fringe is linear proportional to the moving speed of scattering particles (shown in the above equation). If we plug in numbers into the equation above: $V = 1 - 10$ mm/s for normal blood flow speed and $\lambda = 1$ μm, the frequency of the interference fringe F_s will be 2-20 KHz, which is in human audible range. In other words, we can send this signal to a speaker and interpret the blood flow speed by the frequency of the audio feedback.

2.3 Doppler OCT

Doppler OCT that allow measurement of blood flow speed at each location is an important OCT imaging protocol. Doppler OCT first began with the development of TD-OCT. Then, development of Fourier domain OCT (FD-OCT) significantly improves the sensitivity and imaging speed of Doppler OCT. In the following sections, we will introduce Doppler OCT for both TD-OCT and FD-OCT.

2.3.1 Time-domain Doppler OCT

In section 2.1.2, we derive the detector current in a TD-OCT system:

$$I_{d,AC} \sim \sqrt{P_r P_s} P_t * \mathrm{sinc}\left(\frac{\tau}{2\pi/\Delta\omega}\right) * \cos(\omega_0 \tau)$$

The axial resolution is inversely proportional to the wavelength bandwidth and the photons can only interference with each other if the separation of signal source is within coherence range $\frac{\pi\lambda^2}{2\Delta\lambda}$. In section 2.1.2, we only consider the interference between sample and reference arm and did not consider the interference between scatters in the sample and the interference between reference signals. If we consider these effects, the detector current I_d will be:

$$I_d \sim \int |E_r(\omega) + E_s(\omega)|^2 \, d\omega dt$$

$$= \iiint E_r(\omega')E_r(\omega) * e^{-i(2k'l_r - 2kl_r)}\delta(\omega - \omega')d\omega' d\omega$$

$$+ \iiint E_{s1}(\omega')E_{s2}(\omega) * e^{-i(2k'l_{s1} - 2kl_{s2})}\delta(\omega - \omega')d\omega' d\omega, \, l_{s1} = l_{s2}$$

$$+ \iiint E_{s1}(\omega')E_{s2}(\omega) * e^{-i(2k'l_{s1} - 2kl_{s2})}\delta(\omega - \omega')d\omega' d\omega, \, l_{s1} \neq l_{s2}$$

$$+2 * \mathrm{Re}\left(\iint E_r(\omega')E_s(\omega) * e^{-i(2k'l_r - 2kl_s)} * \delta(\omega - \omega')d\omega' d\omega\right)$$

$$= \int {E_r}^2(\omega)d\omega + \int {E_s}^2(\omega)d\omega + I_{hom} + I_{het}$$

The first term is the interference between reference EM waves. However, due to long integration time of the detector, this term is a DC term (doesn't change with the position of the reference mirror) representing the total power reflects from the reference mirror. The second term represents the interference between scatters in the sample locating at the same axial position ($l_{s1} = l_{s2}$). This is also a DC term representing the power reflects from the sample. The third term represents interference between sample scatters locating at different axial positions ($l_{s1} \neq l_{s2}$). This term is a function of $l_{s1} - l_{s2}$ similar to the function depicted in Fig. 2-2C. If $l_{s1} - l_{s2} \gg \frac{\pi\lambda^2}{2\Delta\lambda}$ (coherence length), this term will be zero. However, if two scattering

particles from the sample are within coherence range, they can interfere with each other and generate a homodyne interference (self-interference) term. Self-interference could occur at any location within illuminated area and should be removed to obtain depth-resolved Doppler tomography. The last term is the heterodyne interference term, which we have already discussed in section 2.1.2. Although I_{het} is much stronger than I_{hom} due to stronger reference power (this is also called heterodyne gain), researcher still used a phase modulator in reference arm to isolate the I_{het} signal from I_{hom} in frequency domain for a better signal to noise ratio [130]. With a phase modulator, I_{het} oscillates in time with a modulation frequency f_{het}. The temporal interference fringe can be represented as $I_{het,z}(t)$ when the scanning mirror is at equidistant point corresponding to sample depth z:

$$I_{het,z}(t) = A_z * \cos(f_{het}t + \phi_z)$$

A_z represents the sample backing scattering signal from an axial position z. ϕ_z represents a phase term that depends on path length difference and intrinsic backscatter spectrum. If we consider Doppler shift $f_D = \frac{2V}{\lambda}$, the above equation can be rewritten as:

$$I_{het,z}(t) = A_z * \cos((f_{het} + f_D)t + \phi_z)$$

On the other hand, the frequency of homodyne signal is f_D and thus can be easily separated from heterodyne signal by a frequency filter. After collecting the temporal signal shown above, Fourier transform will be performed to obtain f_D at the specific axial position. We can easily obtain the Doppler shift frequency of each axial pixel by translating the reference mirror and subtracting the measured frequency with the modulation frequency f_{het} .One drawback of this approach is that it requires a long

data collection time window for achieving sufficient frequency (speed) resolution. In other words, there is tradeoff between imaging speed and velocity resolution.

2.3.2 Fourier-domain Doppler OCT

In FD-OCT, an alternative approach uses phase sensitive Doppler analysis, offering advantage of decoupling spatial and speed resolution [131]. The discussion in section 2.1.3 shows that the depth profile can be obtained by performing Fourier transformation of the interference fringe in k space. The transformation result is a complex function $I(z)e^{i\phi(z)}$ with an amplitude $I(z)$ and a phase term $\phi(z)$. The phase difference between adjacent A-scans (or repetitive A-scans) at same axial position, $\Delta\phi(x,z)$ is linear proportional to the moving speed at the specific location, $V(x,z)$:

$$V(x,z) = \frac{\lambda}{4\pi n T}\,\Delta\phi(x,z)$$

λ is the central wavelength, n is the refractive index of the sample and T is the time interval between two A-scans. Averages of phase difference between repetitive A-scans are typically used to reduce noise [131] :

$$V(x,z) = \frac{\lambda}{4\pi n T} * \frac{1}{N-1}\sum_{n=1}^{N-1} \phi_{n+1}(x,z) - \phi_n(x,z)$$

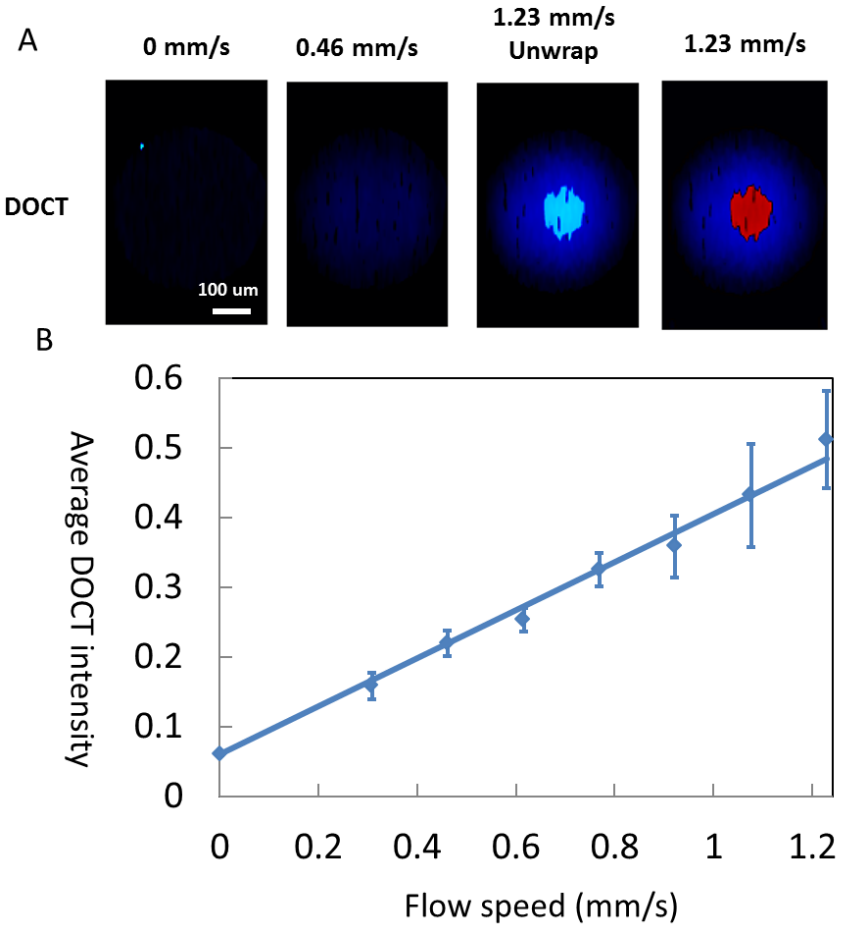

Fig. 2-7. Characterization of Doppler OCT using a swept source system.

N is number of repetitive scans. This method requires multiple A- scans at the same location to improve the signal to noise ratio. In our studies, spatial averaging without sacrificing the imaging speed is used to achieve high quality Doppler imaging. According to the Kasai autocorrelation equation [132], the equation above can be rewritten as:

$$V(x,z) = \frac{\lambda}{4\pi nT} * \frac{\frac{1}{M(N-1)}\sum_{m=1}^{M}\sum_{n=1}^{N-1} J_{m,n+1}Q_{m,n} - Q_{m,n+1}J_{m,n}}{\frac{1}{M(N-1)}\sum_{m=1}^{M}\sum_{n=1}^{N-1} Q_{m,n+1}Q_{m,n} + J_{m,n+1}J_{m,n}}$$

J and Q are defined as: $J + iQ = I(z)e^{i\phi(z)}$. The subscript m is the index of lateral position and n is the index of axial position. The equation above calculates the

average phase difference from a spatial window of M*N pixels. This methods can effective reduce Doppler noise without sacrificing the imaging speed. Appendix A shows the Matlab code for implementing this method (This codes is adapted from the contribution of our past group member, Dr. Jerry Wierwille). Fig. 2-7A shows the DOCT images under different flow speed. The parabolic flow inside the capillary vessel is clearly imaged. Fig. 2-7B shows the intensity of Doppler OCT is linearly response to the flow speed. It is worth to note that when the flow speed is over 1.23 mm/s, the phase intensity in the center jumps over 2π (represented in red color) degree. This is a well-known issue for phase sensitive Doppler imaging [133]. When the flow speed higher than the limitations corresponding to $\pm\pi$ phase difference, the phase will wrap around and the image will encounter a 2π disruption. If the phase only wrap around once, it can be easily unwrapped by add or subtract 2π to the phase jump (Fig. 2-7A, the "Unwrap" Doppler image). The Matlab code for unwrapping is attached in Appendix B.

2.4 Speckle variance

Speckle variance is an alternative method to obtain angiography. Fig. 2-8A shows a conventional OCT structure image of *ex vivo* mouse muscle tissue with an injected blood pool (no bulk flow). Fig. 2-8C-E is the zoom-in images of the blue box in Fig. 2-8A at adjacent time points with 0.125 second interval. Fig. 2-8C-E shows that the static muscle tissue (indicated by the white arrows) has a fixed speckle pattern. In contrast, the blood pool containing free-moving particles has a constantly changing pattern (indicated by the red arrows).

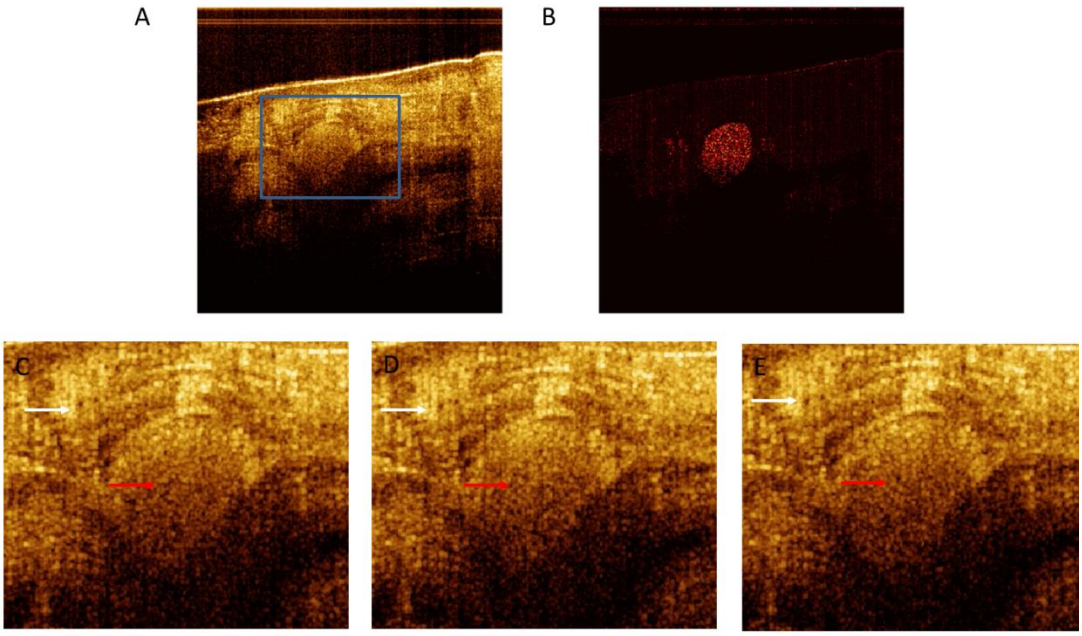

Fig. 2-8. Speckle variance between blood pool and static tissue.

(A) OCT structure image of *ex vivo* mouse muscle tissue with an injected blood pool. (B) Speckle variance image of Fig. 2-8A. The blood pool has much higher intensity than the static tissue. (C) The zoom-in images of the blue box in Fig. 2-8A at adjacent time points.

We can calculate the variance between image frames by [134]:

$$SV_{ijk} = \frac{1}{N}\sum_{i=1}^{N}\left(I_{ijk} - I_{mean}\right)^2$$

j and k are lateral and depth indices of the images and i denotes the slice index. I_{mean} is the average of the same set of pixels. The speckle variance image shown in Fig. 2-8B demonstrates that speckle variance imaging is capable of isolating the region with free moving particles from the static background, even when the scattering intensity of two objects are similar. Fig. 2-9A shows the test results of speckle variance (SV) imaging under different flow speed. SV intensity is independent of the bulk flow speed (Fig. 2-9B, red line). Thus, SV is not suitable for quantifying the speed. However, SV is capable of measuring the volume size occupied by free moving

particles even when the speed is low. Combing SV and Doppler OCT, we can quantify both flow speed and the lumen size simultaneously.

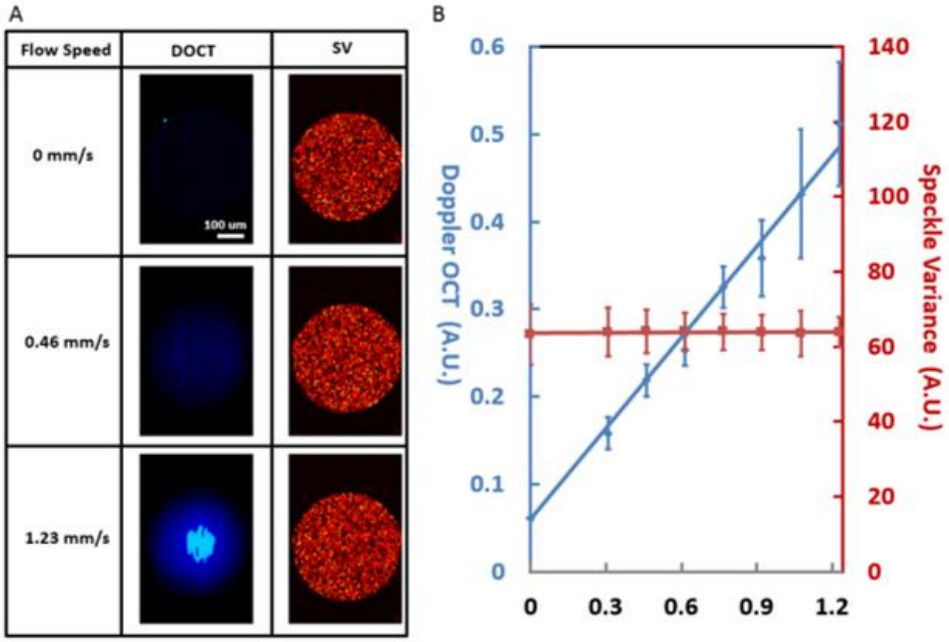

Fig. 2-9. Comparison between speckle variance and DOCT

(A) Cross-sectional DOCT and SV images of a vessel phantom (0.4 mm inner diameter) at various flow velocity. (B) Total intensity of DOCT and SV versus flow velocity.

2.5 Coherence-gated Doppler/LD/DOCT

Coherence-gated Doppler (CGD) is converted from time domain Doppler OCT system. The major differences between CGD (Fig. 2-10A) and DOCT (Fig. 2-10B) are indicated by the blue arrows. Firstly, we used a light source with a longer coherence length and extended the axial dimension of the detection volume from ~10 μm to 190 μm. By covering a larger detection volume, we can acquire ensemble information from the ROI and omit the requirement to scan the reference mirror. Secondly, we further extended the detection volume by omitting the phase modulation, which is commonly used in time-domain DOCT system[133, 135, 136]. The phase modulator in DOCT (Fig. 2-10B) enables heterodyne detection and rejects

the self-beating signal (the interference between sample photons). Equation below shows more details:

$$I \sim \left|E_R + E_S\right|^2 = E_R E_R^* + E_S E_S^* + 2\,\mathrm{Re}\left(E_R E_s^*\right) = I_R + I_{\mathrm{hom}} + I_{het}$$

I is the intensity on the detector; E_R is the electric field from reference arm and E_s is the electric field from sample arm; I_R is the reference intensity coming from the interference between reference photons; I_{hom} is the homodyne intensity coming from the interference between sample photons (self-beating signal); I_{het} is the heterodyne intensity coming from the interference between sample and reference photons.

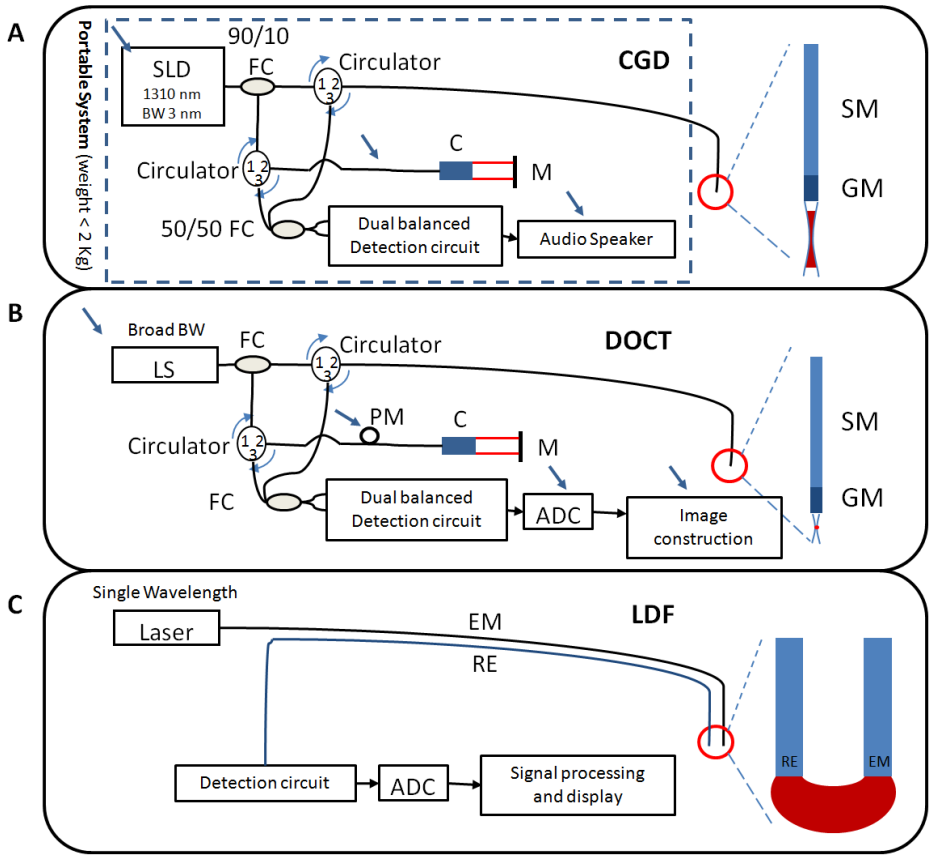

Fig. 2-10. System comparison between CGD/DOCT/LD

(A) CGD system (B) Doppler OCT system (C) LDF system. SLD: superluminescent diode, LS: light source, BW: wavelength band-width, FC: fiber coupler, C: collimator, M: mirror, PM Phase modulator, ADC: analog to digital converter, SM: single-mode fiber, GM, gradient-index fiber, EM: emission fiber, RE, receiver fiber. The detection volume of each system is shown in the probe drawing to the right in red. From ref. [137].

Because there is no Doppler shift between reference photons, I_R is a DC signal. On the other hand, due to the Doppler shift between sample photons and between sample and reference photons, I_{hom} and I_{het} are AC signals. In conventional time-domain OCT systems, due to the phase modulation in reference arm, I_{het} signal can be separated from the I_{hom} in frequency domain and I_{het} is the Doppler signal coming from the tissue within the coherence length surrounding the zero-delay plane. Therefore, if we select the heterodyne signal by frequency filtering, we can achieve high resolution flow imaging as demonstrated by time domain Doppler OCT system [130] . In CGD system, we omit the phase modulation and do not intend to distinguish the I_{het} and $I_{hom.}$ Therefore, we receive all the Doppler signals accumulated in the illuminate path instead of just collecting the signal surrounding the zero-delay plane. In terms of its use for self-beating detection, CGD and LDF systems are similar; both collect Doppler signals accumulated along the illumination path. However, CGD has better spatial resolution than LDF (Fig. 2-10C) due to the confocal probe design and the SLD's shorter coherence length. Moreover, we can optimize the sensitivity by tuning the reference power I_R [129]. Lastly, the interference fringe is directly converted to an audio signal without frequency demodulation. The frequency of the Doppler beating signal is proportional to the blood flow velocity: $\Delta f = \frac{2V\cos(\theta)}{\lambda}$. The velocity V of blood flow within medium-sized vessels is 10 mm/s [138]. The wavelength of light source λ used in the present study is 1.3 μm. The effective angle θ between the probe and blood flow varies, depending to the angle of approach, numerical aperture of the probe, and degree of multiple scattering within the tissue and blood. In practice, scattering within the tissue and blood ensures that the effective

Doppler angle is never exactly 90 degrees, so that flow is detectable even with orthogonal orientation between the probe and a medium-sized vessel. The peak frequencies of the Doppler signal Δf are typically 0.1 - 15.4 kHz, which is within human audible bandwidth. Therefore, expensive data acquisition or any further data processing is not required to interpret the signal. We can directly identify the flow speed by the pitch of sound and the size of vessel by the volume of sound.

Except the design shown above (Fig. 2-10A), other variations of CGD design for different applications are discussed below:

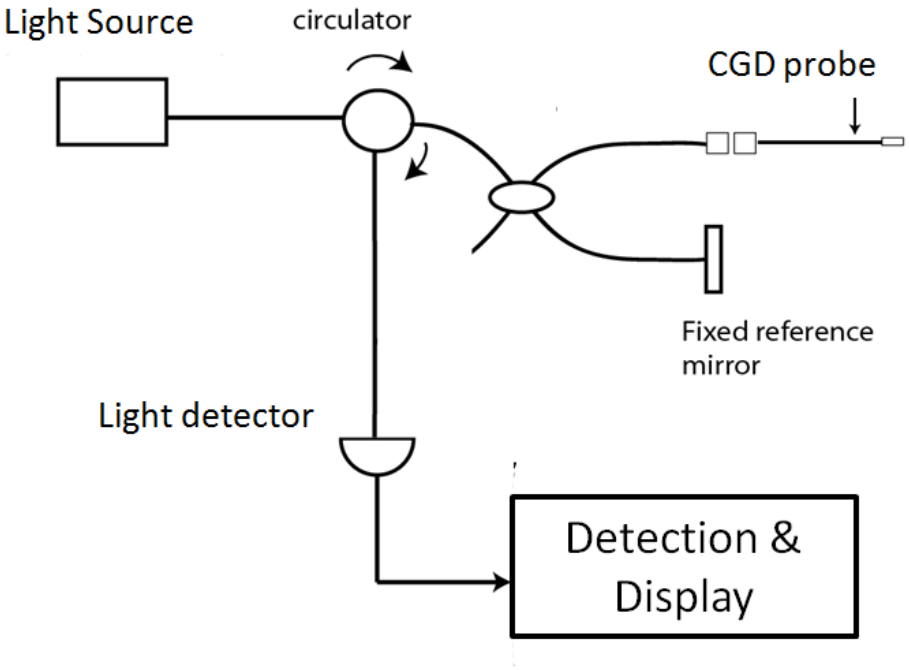

Fig. 2-11. CGD system without dual balanced detection.

1) Simple interferometer: If sensitivity is not an issue, we may not need the dual balanced detector. This design (Fig. 2-11) has one less circulator, fiber coupler and photo diode than our current design. It is simpler and cheaper.

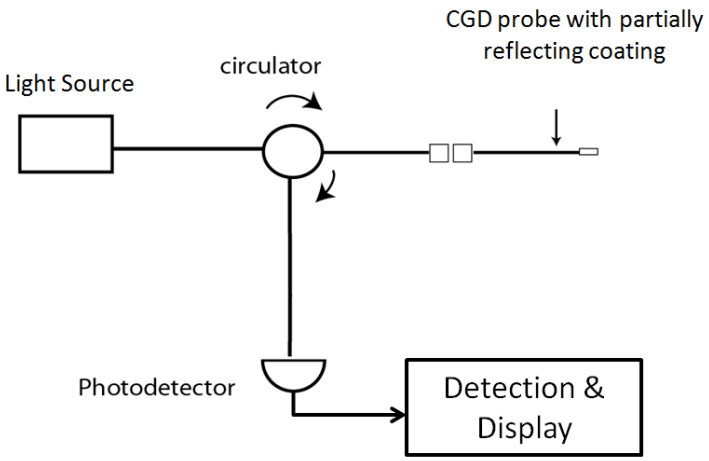

Fig. 2-12. CGD system with a common path fiber probe.

2) Common path fiber probe: Common path fiber design with partially reflective coating at the tip simplifies the system (Fig. 2-12). With an integrated reflector, an independent reference arm can be omitted. Eliminating the fine adjustment in reference arm makes the maintenance easier. The integrated reflector provides better dispersion compensation and better axial resolution.

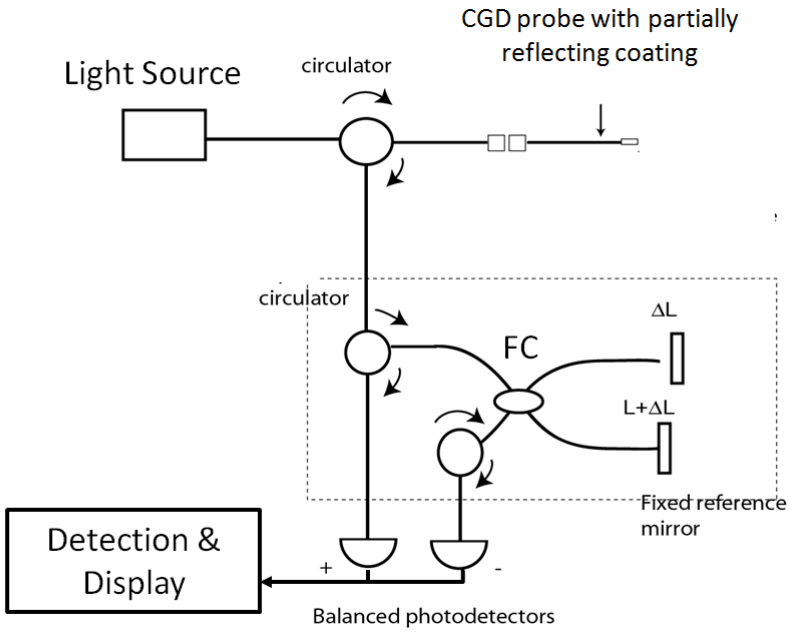

Fig. 2-13. Common path fiber probe with a secondary interferometer.

3) Common path fiber probe with a secondary interferometer: One limitation of the common path interferometer design is that axial position of the zero delay plane in the sample is fixed. This problem can be solved by implementing a second interferometer (The dashed box in Fig. 2-13). The zero delay plane in this design can be changed by translating the movable mirror in the interferometer for maximizing the sensitivity.

4) Heterodyne and Homodyne isolation: In order to enhance the coherence gated effect, we may need to separate the homodyne and heterodyne signal by implementing a phase modulator to reference arm. Homodyne signal comes from the interference between Doppler-shifted and non-shifted photons from the sample. This interference could origin from any place within light illumination path. On the other hand, the heterodyne signal comes from the interference between non-shifted reference photons and shifted sample photons. This signal only comes from certain sample region at equidistant position to the reference mirror. Heterodyne and homodyne signals are usually mixed together. For some applications, such as pulp vitality test, only the heterodyne signal from the pulp region should be collected and signals from surrounding tissues should be rejected. These two signals can be separated by introducing a phase modulator to the reference arm. This will shift the heterodyne signal to a higher frequency and allow us to separate it from low frequency homodyne signal. This technique could potentially improve the specificity by reducing the background noise.

Chapter 3: OCT needle probe for neurosurgery guidance[2]

3.1 Introduction

Although OCT imaging (section 1.3.1) has a great potential to transform neurosurgery guidance; it will not be possible to bring these great imaging capabilities to the bedside without a translational device. An effective image guidance probe for stereotactic procedures in the brain needs to satisfy three criteria. It must have a thin needle-like geometry (O.D. < 1 mm), forward-imaging ability to identify tissue landmarks, and the ability to detect blood vessels. Numerous forward-imaging probes have been developed for OCT [57, 80, 81, 95, 99, 139-149], but their distal-end designs (> 1 mm) are too large to fit into the thin guide catheter used for stereotactic brain surgery. Dr. Tang's group proposes a thin needle-type side-viewing OCT probe as a means for image guidance in DBS [40]. The probe has demonstrated that its resolution (15 μm) and sensitivity are sufficient to discern micro-anatomical landmarks in ex vivo human brains [40]. An in vivo small rodent study has demonstrated that the ability of detecting these landmarks in real time can guide the delivery of therapeutic agents or dissection to specific deep brain targets [43]. The weakness of this approach is that it cannot provide information on at-risk vessels in front of the advancing probe. Another novel design using a paired-angle-rotation scanning (PARS) probe [58, 150] achieves forward-imaging needle-based (O.D. = 820 μm) endoscopy by using two counter-rotating gradient-index (GRIN) lenses. Yet another group developed an elegant forward-imaging probe by relaying the scanning

[2] The content of this chapter is reproduced from "C.-P. Liang, J. Wierwille, T. Moreira, G. Schwartzbauer, M. S. Jafri, C.-M. Tang, and Y. Chen, "A forward-imaging needle-type OCT probe for image guided stereotactic procedures," Optics Express 19, 26283-26294 (2011)" with permission.

beam using a long GRIN rod lens, while keeping the endoscope itself stationary. This design provides fast dynamic focus tracking, which can perform high quality non-contact in vivo 3D imaging [151]. Two different dynamic ranges of GRIN rod lenses have been reported: 72 dB and 108 dB [152, 153]. In order to optimize the dynamic range, 8-deg-beveled glass windows and antireflection coating were applied to reduce the reflection from the end surface [151]. Previously reported GRIN-rod-lens-based probes are primarily for laryngoscopy or laparoscopy applications with probe sizes ranging from 2.7 – 4.58 mm [151-154]. To our knowledge, Doppler capability of the probes with O.D. smaller than 1 mm has not yet been demonstrated. This may be due to the difficulty of actuating the optics in such limited space. The limitations of existing approaches for OCT-guided stereotactic brain procedures motivated us to develop a GRIN-rod-lens approach that can satisfy the thin forward-imaging, needle-type criteria and the optical Doppler imaging criteria.

In this study, we demonstrated that the GRIN-rod-lens design can be miniaturized to a needle-imaging probe (O.D. = 740 μm). High-speed (100 frames/s) and high-sensitivity (>90 dB) OCT imaging was achieved by using this needle probe. The stationary GRIN-rod-lens also provides high quality DOCT imaging with 41 dB velocity dynamic range (VDR) and ±17 μm/s velocity resolution. The effectiveness and robustness of the system was demonstrated in studies of sheep brain in vivo and human brain ex vivo.

3.2 Materials and methods

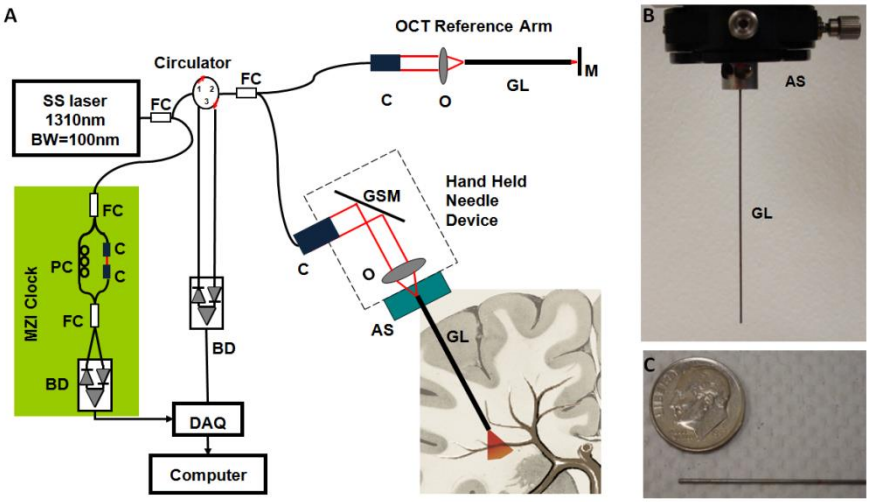

Fig. 3-1. Schematic and pictures of the handheld OCT device

(A) Schematic of the handheld OCT system. FC: fiber coupler; PC: polarization controller; C: collimator, BD: balanced detector, MZI: Mach-Zehnder interferometer (frequency clocks), DAQ: data acquisition board, M: mirror, GSM: galvonometer scanning mirror, O: objective lens, AS: alignment stages, GL: GRIN lens needle. (B) GRIN needle. (C) GRIN needle placed beside a U.S. dime. From ref. [41].

3.2.1 Forward-imaging OCT probe

Fig. 3-1A shows the schematic of the OCT and handheld needle imaging device. The swept-source OCT system previously developed by our group [155-157] utilizes a wavelength-swept laser as its light source. Spectrum bandwidth of the laser is 100 nm centered at 1325 nm (Thorlabs, SL1325-P16). The wavelength-swept frequency is 16 kHz with 12 mW output power; therefore, for 160 axial lines images, the frame rate is equivalent to 100 frames per second. A Mach-Zehnder interferometer (MZI) receives 3% of the laser output power and uses it to generate a clock signal with uniformly spaced optical frequency to trigger the sampling of the OCT signal in the analog-to-digital (A/D) converter. The sample and reference arms of a Michelson interferometer receives equal portions of the remaining 97% of the laser power. The galvanometer scanning mirrors deflect the sample arm light into the GRIN-rod

imaging needle (NSG America, LRL-050-P400) through a low numerical aperture (NA) lens. Careful NA matching between GRIN lens (NA 0.084) and coupling lens ensures maximum coupling efficiency. The distal end of the GRIN needle receives the scanning laser spot from the proximal end and relays the backscattered signal back to the interferometer. The diameter of the GRIN lens is 0.5 mm and the outer diameter including the stainless steel tubing is 0.74 mm. To reduce the risk of blood vessel laceration and mechanical resistance in the tissue, we created a blunt tip by attaching a transparent cap to the distal end of the GRIN lens. Fig. 3-1B shows the picture of the GRIN needle (GL) and Fig. 3-1C shows the GRIN needle placed beside a U.S. dime.

3.2.2 In vivo sheep brain deep vessel imaging

All procedures were approved by the Institutional Animal Care and Use Committee at the University of Maryland School of Medicine, and animals were treated in accordance with the PHS Policy on Humane Care and Use of Laboratory Animals, the National Institutes of Health Guide for the Care and Use of Laboratory Animals, and the Animal Welfare Act (7 U.S.C. et seq.). The effectiveness of the needle probe was evaluated by examining its ability to detect vessels below the surface of the parietal lobe of sheep (n=2, male, wt. ~ 100 kg). Anesthesia was induced with 5 mg/kg ketamine (IV) and maintained under 1-4% isoflurane in 100% oxygen. After the sheep was deeply anesthetized, craniotomy was performed. The dura and pia membrane on the surface were carefully removed. Then, the imaging needle was inserted at the speed of 0.05 mm/s by a motorized stage. OCT and DOCT were acquired simultaneously at an imaging speed of 8 frames per second (1024 A-

scans per frame) during the insertion. The velocity variance images were derived by a previously described method [133]. The variance signal is a surrogate of flow speed with a wider speed measurement range than DOCT signal and thus, less prone to alias problem existing in the DOCT images. Intensity threshold and a customized image segmentation algorithm were used to remove the noise in the variance images. The region of interest (ROI) is set in the area with high DOCT signal to noise ratio (SNR). A plot of the averaged variance signal in the ROI against time provides quantification of vessel pulsation. In one experiment, the OCT probe approached a vessel that was located within a deep sulcus and was held relatively immobile by the pia mater. In a second experiment, the OCT probe approached a vessel that was located within the brain parenchyma and could move with the brain tissue.

3.2.3 In vivo rat femoral vessel imaging

To demonstrate that the needle OCT device can differentiate artery from vein, we imaged the femoral vessels of Sprague-Dawley rats (n=4, male, wt. ~ 400 g). Anesthetized rats (ketamine 50 mg/kg and xylazine 5 mg/kg, intraperitoneal) in supine position had their femoral vessels exposed and placed directly under the needle OCT probe. The blood vessel color and relative position to the femoral nerve allow visual identification of the artery and vein. The imaging speed of the simultaneously acquired OCT and DOCT images was 8 frames per second.

3.2.4 Ex vivo human brain imaging

To demonstrate the capability of this needle OCT device to image highly-scattering biological tissues and to determine the feasibility of using anatomic

landmarks for locating the position of the imaging probe, we chose to image the human basal ganglia ex vivo. The basal ganglia is an appropriate region for this demonstration because it is the target of DBS for movement disorders [6] and because it contains high contrast structures that help in defining the anatomic location. An unfixed coronal section containing the basal ganglia was placed on a motorized stage and kept moist by phosphate-buffered saline (PBS). The OCT probe was gradually inserted into the brain tissues by movement of the stage at a constant speed of 0.45 mm/s. OCT images were recorded along with the needle insertion at 100 frames/s (160 A-scans per frame). We also reconstructed full-track OCT images for correlating OCT landmarks with brain structures. The reconstructed OCT images were formed by splicing sub-regions from raw OCT images. A band of pixels (0.44 mm width, 0.0045 mm length) located at 0.2 mm from the distal surface of the GRIN lens was excised from each raw OCT images and rejoined to form the reconstructed image along the track of insertion passage.

3.3 Results

3.3.1 Characterization of forward imaging OCT needle

The forward-imaging needle probe can resolve microstructure with great sensitivity as shown by imaging of a lemon (Fig. 3-2A). The major barrier to optimize the sensitivity is the high reflection from both surfaces of the GRIN rod lens. We tackled this problem by attaching a high refractive index cap (n=1.56, which is close to the refractive index of GRIN lens n=1.61) at the distal end, and using oblique illumination at the proximal end to minimize specular reflection. The sensitivity was

quantified by measuring the attenuated reflection from a high reflector (mirror). The attenuation from the neutral density filter is 36 dB and the mirror reflection is 54 dB. Therefore, our sensitivity is 90 dB. With careful dispersion matching at the reference arm by another GRIN-rod lens (with the same specification as the one used in the sample arm), the axial resolution was optimized. We characterized the axial resolution by measuring a reflective mirror (Fig. 3-2B). The axial resolution defined by the full width half maximum (FWHM) of the reflection surface is 17 μm in air (or 12 μm in tissue assuming an index of refraction of 1.4). The transverse resolution was measured by scanning a laser spot across a sharp edge of a reflective metal line on a US Air Force target (Fig. 3-2C). The distance between 10-90% intensity is 13 μm. The field-of-view (FOV) is limited by the diameter of GRIN rod lens. For a 0.5 mm diameter GRIN lens, the FOV is 0.44 mm.

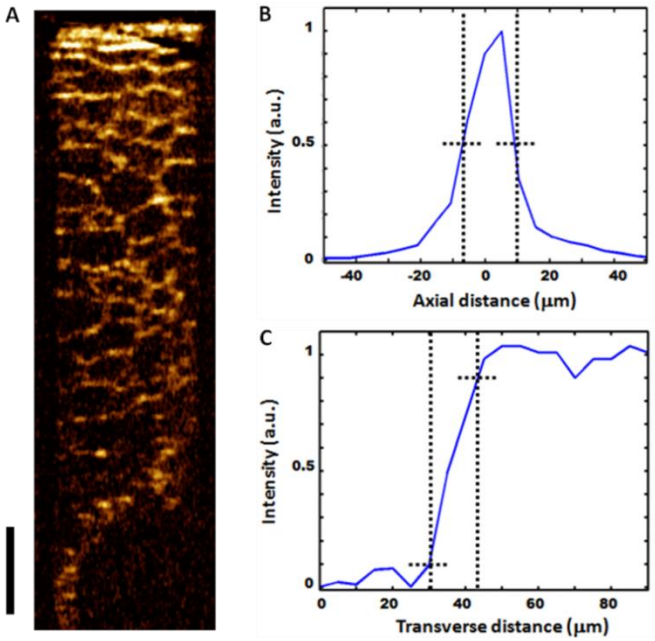

Fig. 3-2. Resolution test of the forward-imaging OCT probe

(A) An OCT image of lemon acquired by a forward-imaging OCT probe. The scale bar is 0.25 mm. (B) The axial intensity plot of a highly reflective mirror. The axial resolution determined by FWHM is 17 μm in air (or 12 μm in tissue). (C) The intensity plot across a sharp edge on a US Air Force target. The transverse resolution determined by 10-90% positions is 13 μm. From ref. [41].

3.3.2 In vivo sheep brain deep vessel imaging

The blood vessel DOCT imaging from an anesthetized sheep by the needle probe shows the feasibility of vessel detection in vivo. Fig. 3-3 shows OCT and DOCT superimposed images at different time points of a vessel as it was detected, monitored, and then compressed by the advancing probe. The OCT images in Fig. 3-3 shows that the speckle size in the lumen of vessels is much smaller than the speckle size of the wall making the boundary of the vessel wall easy to identify. The colormap scale for the DOCT signal is analogous to the colormap used for ultrasound Doppler signals. Red to yellow represents increasing flow speed in one direction whereas blue to cyan represents increasing speed in the opposite direction. However, the alias rings in these images do not indicate the change of flow direction. Instead, the abrupt change of color represents higher velocity that is "wrapped." "Wrapping" occurs because the velocity exceeds the velocity dynamic range (VDR). When velocities exceed this limit in either direction, they "wrap" to values at the other end of colormap [133]. The superimposed image further verified the boundary of lumen and indicated that this system can provide measurement of the vessel size (~ 0.2 mm in diameter) that is verified by both OCT and DOCT. Fig. 3-3A shows a vessel was detected in front of the probe. Fig.3-3 shows the probe was approaching the vessel. Fig. 3-3B shows an image of the probe that was stopped right before hitting the vessel. Fig. 3-3 shows the vessel pulsation while keeping the probe still. The periodic changes observed in the flow speed images strongly suggest that the vessel is a pulsating artery. Fig. 3-3C shows the needle probe compressing the vessel. Fig.3-3 shows that, with the probe advancing gradually, the lumen of vessel becomes more and more constricted and the

Doppler signal also decreases accordingly. Fig. 3-4 shows that the pulsation can be quantified by flow velocity variance. Flow velocity variance varies monotonically with flow velocity and has a wider measurement range [36]. Therefore, it provides more accurate estimation of the flow speed than the aliased DOCT signal. However, it is prone to large error in regions with low SNR, so we set our ROI in a region having stable DOCT signal (the black rectangle in the variance image). Both DOCT and variance images show a dramatic difference between peaks and valleys. The larger red signal area in the DOCT images indicates higher flow velocity at the peaks. Also, the variance images show stronger signal corresponding to the higher flow velocity at peak. The average of the ROI variance signal versus time shows clear pulsation pattern. The heart rate is 80 beats per minutes. The high SNR Doppler signal enables us not only to detect the vessel but also to monitor the physiological change of the blood flow.

An example of the vessel being pushed aside by the probe is shown in Fig. 3-5. A vessel was detected 0.93 mm in front of the probe by its Doppler signal (Fig. 3-5). As the probe approached to the vessel, the vessel is gradually pushed aside (Fig. 3-5A&C) and finally out of the field of view (Fig. 3-5D). We also notice that the high blood flow speed in this large vessel made the Doppler alias rings smaller than the pixel size resulting in randomized Doppler signals. Although DOCT cannot provide quantitative flow data in this case, it still acts as a sensitive detection tool.

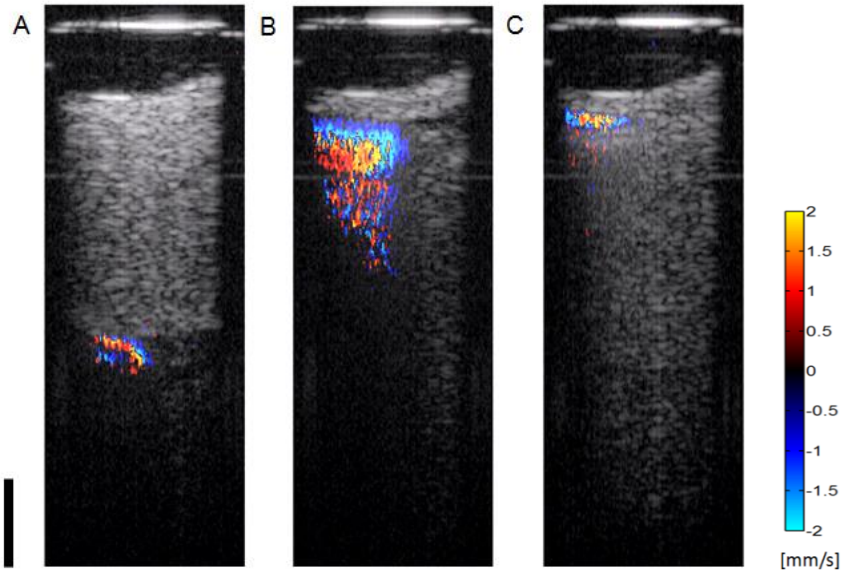

Fig. 3-3. A high-risk case of contacting a brain vessel.

Compression of a vessel by the OCT probe. All the images are from the same vessel. The bright line on the top of the images is the junction between GRIN rod lens and the transparent cap. The front curved surface of cap had direct contact with the tissue. The scale bar in all the figures is 0.25 mm. (A) The OCT/DOCT superimposed image shows a vessel 0.65 mm in front of the probe. (B) The superimposed image from shows a vessel right in front of the probe (C) The superimposed image from shows the vessel was compressed by the probe. From ref. [41].

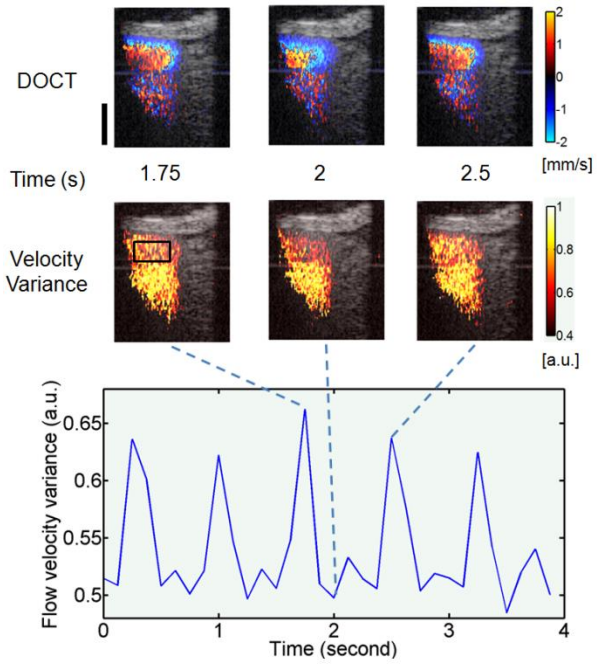

Fig. 3-4. Quantification of pulsation by flow velocity variance.

The first row shows Doppler images at different time points specified in the second row. The third row shows the corresponding velocity variance images. The black rectangle shows the ROI. The value of flow velocity variance in the plot is the average value of ROI. The dashed lines indicate the time points of the corresponding image set. The scale bar is 0.2 mm. From ref. [41].

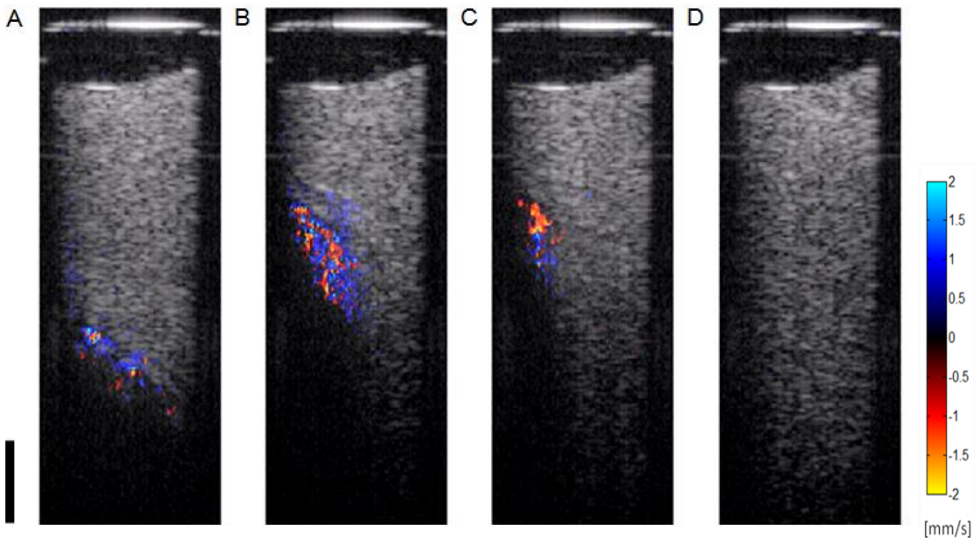

Fig. 3-5. A low-risk case of contacting a brain vessel.

The images from A-D are in sequence as the probe was advancing. The scale bar in the figure is 0.25 mm. The OCT/DOCT superimposed image of a vessel (A) 0.75 mm in front of the probe, (B) 0.35 mm in front of the probe with the vessel was being pushed aside, (C) 0.35 mm in front of the probe with the vessel was pushed further away from the probe, and (D) after the probe had passed the vessel. From ref. [41].

3.3.3 In vivo rat femoral vessel imaging

Imaging the rat femoral vessels shows the feasibility of vessel type differentiation by the OCT needle probe. The color and appearance of the rat femoral artery and vein distinguish them unequivocally by visual inspection. Fig. 3-6A and 3-6B show both OCT and OCT/DOCT superimposed images of a rat femoral artery. Fig 3-6C and 3-6D are the images of the femoral vein. The bright lines at the top of images represent the end surface of the imaging needle. The speckle size and superimposed images allow us to differentiate the lumen and the vessel wall easily. The images show that the arterial wall is much thicker than the venous wall. Another distinguishing feature is the black outline surrounding the arterial lumen shown in Fig. 3-6A. This black outline is a muscular medial layer of endothelial lining lacking highly scattering elastin or collagen. In contrast, the medial layer in the vein typically contains more

elastin and collagen [158]. Therefore, in Fig. 3-6C, we do not find this black layer. Furthermore, the steeper flow speed gradient in the artery leads to much denser alias rings in Doppler images (Fig. 3-6B vs. 3-6D). Therefore, the wall thickness, black inner lining and flow speed are three important parameters for differentiating the vessel types.

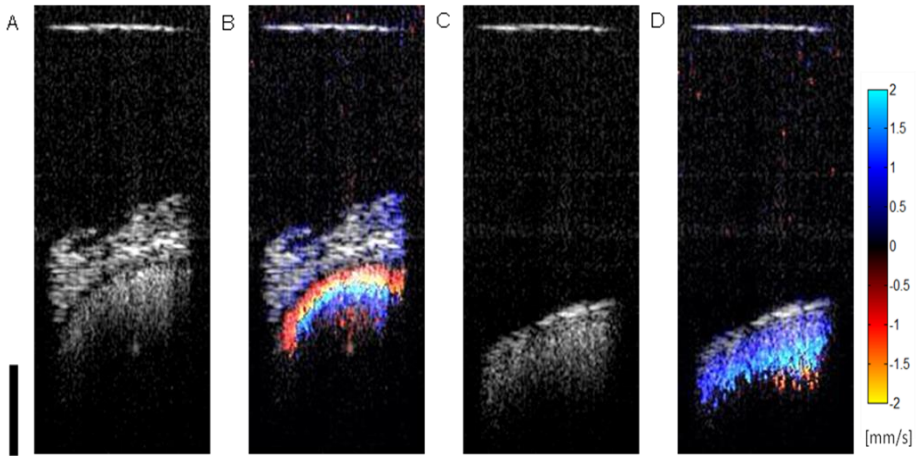

Fig. 3-6. OCT and OCT/DOCT superimposed images of rat femoral vessels

The scale bar represents 0.25 mm. (A) OCT image of femoral artery. (B) Superimposed image of femoral artery. (C) OCT image of femoral vein. (D) Superimposed image of femoral vein. From ref. [41].

3.3.4 Ex vivo human brain imaging

The images of the human basal ganglia ex vivo illustrate the potential for neurosurgical guidance. Fig. 3-7 shows a camera image of human brain tissue and the full-track reconstructed OCT image. In the camera image of brain tissue, note the white appearance of fiber tracts surrounding the gray matter nuclei and the striation of white fiber bundles within the putamen. The reconstructed OCT track was obtained by pushing the probe from right to left 2 mm below and parallel to the surface of the brain slice. This figure illustrates the high degree of contrast between gray and white matter generated by OCT. The transition between the thin white fiber capsule, the

gray matter putamen, and the lamina to the GPe can be clearly identified. These OCT-detectable structures are useful anatomic landmarks that can be used in stereotactic surgery [40, 43, 159]. The structures identified in this passage includes: extreme capsule (ex), claustrum (Cl), external capsule (ec), putamen (PUT), lateral medullary lamina (lml). The white matter typically has much higher intensity with shallower penetration depth. Also, the characteristic white matter striations in the putamen display high contrast and can be easily identified. Because the needle was inserted 2 mm below and parallel to the surface of the brain slice, the number and the size of the fiber tracts in the camera image are different from the fiber tracks in OCT image. Reconstruction of the full-track OCT image allows better identification of the probe location. This information can assist in the guidance of therapeutic tools to deep brain targets with micrometer precision.

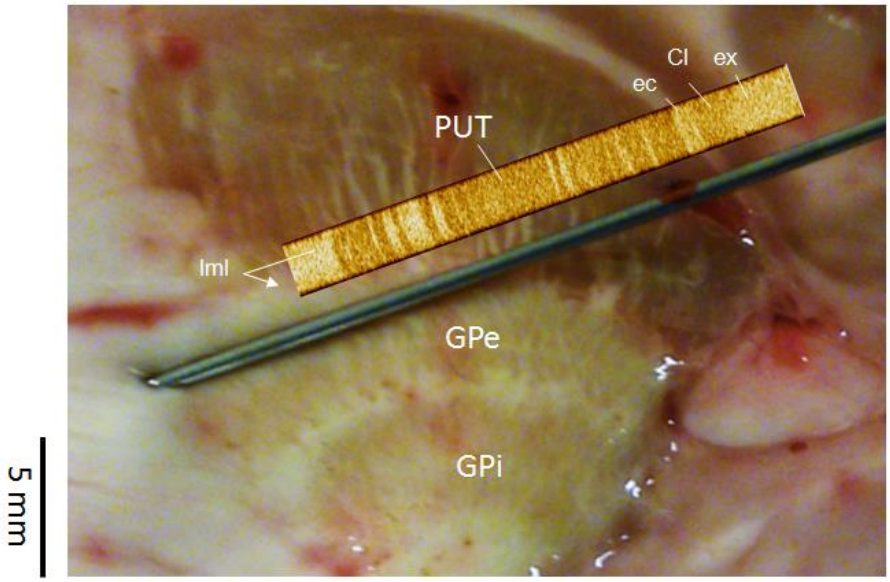

Fig. 3-7. Full-track OCT image of a human basal ganglia.

The probe on top of the brain tissue shows relative dimension and the direction of insertion (from top right to bottom left). The full-track OCT image is placed proximal to the insertion passage. Major structure are labeled: extreme capsule (ex), claustrum (Cl), external capsule (ec), putamen (PUT), lateral medullary lamina (lml), globus pallidus externa (GPe) and globus pallidus interna (GPi). The width of the reconstructed OCT images in this figure is expanded for better visualization. The real width is 0.44 mm. From ref. [41].

3.4 Discussion

An image-guidance probe for stereotactic neurosurgery needs to address multiple challenges. The fundamental challenge is to provide information on what is in front of the probe in real time for a procedure that is otherwise blind. The primary clinical objective is to avoid lacerating blood vessels in front of the advancing probe. A secondary objective is to obtain information on the position of the probe tip relative to anatomic landmarks. This has to be accomplished with a thin needle-like geometry that will fit inside existing stereotactic apparatus.

The GRIN-rod-lens approach provides a solution to the multiple requirements for stereotactic neurosurgery. By using motion-free GRIN rod lenses as relay optics, the high speed A-line scanning rate of the laser system can be fully exploited without compromising the needle size. This high speed forward-imaging capability allows us to promptly avoid the at-risk vessels (Fig. 3-3) and locate the tip position (Fig. 3-7). Moreover, stable and high speed A-line scanning is critical for optimizing the flow VDR [133]. Unstable and slow A-line scanning rates will degrade VDR and hinder vessel detection by DOCT. Our system not only detects vessels but also monitors the physiological changes of the blood flow (Fig. 3-4). Since there is no complex actuation at the distal end, this probe is one of the thinnest forward-imaging OCT probes. The diameter of the probe is a compromise between providing sufficient field of view and minimizing tissue injury. A GRIN lens diameter of 0.5 mm and field of view of 0.44 mm allows easy recognition of vessels, and the overall diameter of 0.74 mm is smaller than the inner diameter of existing stereotactic cannulae. Our current GRIN rod lens has a length of 12 cm. A portion of the rod lens (2.5 cm) is used for

interfacing the rod lens with the scanning head. Therefore we can insert 9.5 cm deep inside the brain. The current probe length is more than adequate to reach all existing targets of DBS in the human. It can also be used for brain tumor biopsy, ventricle identification, etc. Also, the length could be further extended by splicing several pieces of GRIN rods together.

Evaluating the system in a living large mammalian brain provides correlates to the conditions of clinical stereotaxis. While useful information can be obtained from studies in phantoms, rodents and ex vivo human tissue, these substitute samples cannot provide adequate simulation of the live human brain surgery. There are no vessels in the rat brain that are comparable in size to those in the human brain. Large animal brain imaging in vivo also provided an opportunity to determine the extent of a potential problem for DOCT. The brain moves in conjunction with respiration and heart beat. We found that this was problematic for imaging surface vessels, but not for intraparenchymal vessels. The surgeons can bypass surface vessels because they can directly visualize them. Once the probe entered the brain parenchyma, the movement problem is greatly decreased, possibly because the probe appears to stabilize the tissue directly in front of it. Additionally, vessels within the parenchyma can be easily pushed to the side by the probe (Fig. 3-5), whereas vessels in deep sulci (Fig. 3-3) that are tightly attached to the pia mater are not easily pushed aside by the probe. Vessels in sulci are really surface vessels that are buried by the cortical folds. This is consistent with anecdotal experience of neurosurgeons who meticulously avoid entering cortical sulci.

Besides detecting the vessels, the probe can also monitor the pulsation (Fig. 3-4) and differentiate the vessel type (Fig. 3-6). These capabilities could be valuable for screening the vessels posing high risk in neurosurgery. We acknowledge that the aliasing problem may hinder using DOCT signal to quantify blood flow; however, we can work around this problem by using velocity variance [133] or axial Kasai algorithm [160]. Also, the high speed Fourier domain mode locking laser should be able to increase the velocity detection limit by one to two orders [65, 161].

In addition to detecting the at-risk vessels, this forward-imaging needle-type OCT probe can be an important complementary technology for current stereotaxic neurosurgery. Prior studies have demonstrated the ability of catheter-based OCT to provide information on the position of the probe relative to neighboring anatomic landmarks [40, 43]. Although the forward-scanning probe does not provide as much field of view as with the rotating side-imaging approach [40], the needle probe can be used to provide real-time feedback on the degree to which the brain has shifted due to the surgery induced CSF leak. This is accomplished by establishing the probe tip relative to critical landmarks such as a prominent gray matter-white matter junction (Fig. 3-7). Since the stereotactic system provides the expected position, any deviation between the expected and actual location of a landmark provides the surgeon useful information on the degree to which the brain has shifted during surgery. Secondly, it can often provide optical signatures of specific anatomic structures (i.e. the pencils of fibers in the putamen). The use of image guidance probes in conjunction with pre-operative MRI or CT images will give the surgeons greater confidence on the probe location. However, for diagnosis of other pathologies, a wider FOV may be desired.

A possible way is to reconstruct a wider FOV image using manual scanning and optical tracking [162]. The next phase of this project will be to miniaturize the overall proximal size and integrate a functional imaging modality. Besides the application in stereotactic procedures, this device can potentially be applied to many other image-guided interventions and for the detection of blood flow involving difficult to reach structures.

3.5 Conclusion

The forward-imaging needle-type OCT probe is a promising complementary technology for current stereotaxic neurosurgery. With real time OCT/DOCT forward imaging capability, it may be possible to avoid laceration of at-risk intraparenchymal vessels and infer probe location relative to OCT detectable landmarks. The device described here may be adapted to multiple intervention procedures in addition to stereotactic neurosurgery.

Chapter 4: Concurrent Magnetic Resonance Imaging (MRI) and Optical Coherence Tomography (OCT)[3]

4.1 Introduction

As described in the last chapter, OCT is a great complimentary technology for stereotactic neurosurgery, but small field of view (FOV) limits its usage. MRI is the most widely used neuroimaging tool with large FOV. Combining high resolution OCT with large FOV MRI will allow the neurosurgery being performed more efficiently and accurately. The goal of this study is to develop a MRI compatible OCT imaging system and validate the multi-scale MRI/OCT imaging for neurosurgery guidance.

The superior tissue contrast and versatile imaging protocols of intra-operative MRI (iMRI) make it a promising guidance tool for various surgeries [116, 163, 164]. However, sending a patient into the constrictive MRI bore interrupts the surgical rhythm and thus the number of imaging studies in one procedure is limited to two or three times. On the other hand, the iMRI system with big opening and better accessibility to the patient suffers from poor imaging quality. In order to take full advantage of MRI guidance, MRI-compatible robotic systems that can operate inside the restrictive MRI bore with near real-time MRI guidance have been developed [165-167]. These systems are promising, but their targeting capability is still limited by the resolution of MRI. Moreover, the artifact surrounding surgical tools (such as metallic electrode or biopsy needle) obscures the important region of interest (ROI)

[3] The content of this chapter is reproduced from "C.-P. Liang, B. Yang, I. K. Kim, G. Makris, J. Desai, R. Gullapalli, Y. Chen, "Concurrent multiscale imaging with magnetic resonance imaging and optical coherence tomography", J. Biomed. Opt. 18(4), 046015 (2013)" with permission.

and makes it difficult to achieve sub-mm accuracy. In this study, we integrate an OCT imaging system to the MRI-compatible robot developed by Dr. Jaydev Desai's group at the University of Maryland[166] and use the microscopic OCT information to deliver a biopsy needle with unprecedented accuracy. The innovative MRI-compatible robot enables us to teleoperate the needle device within the constrictive MRI bore and performs OCT under continuous MRI monitoring. The MRI-compatible robot opens a new possibility of concurrent multi-modal imaging that could potentially have huge impact on biomedical imaging. The combination of macro-scale MRI morphology and micro-scale OCT architecture in a concurrent and co-registered manner paves a new avenue to the iMRI interventions required sub-mm precision.

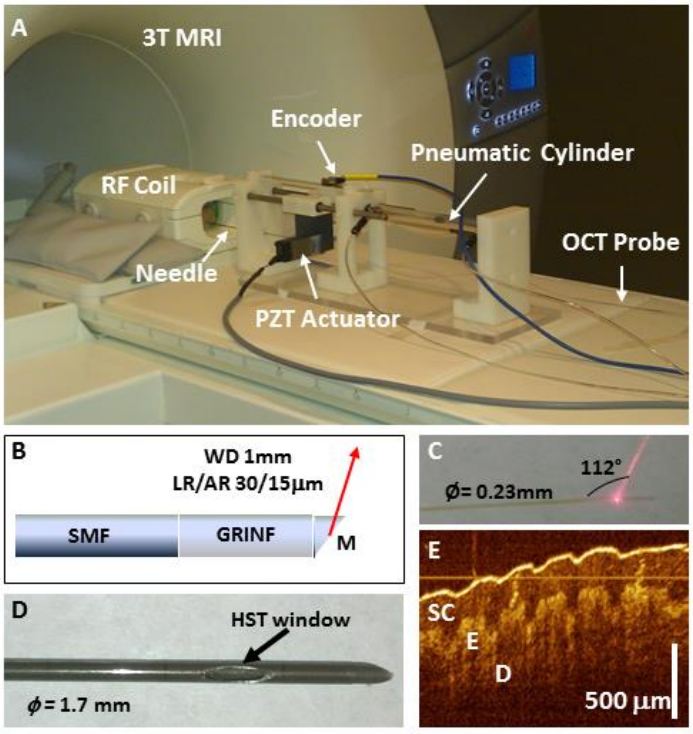

Fig. 4-1. MRI/OCT system

(A) Picture of the MRI/OCT imaging system. (B) Side-viewing OCT probe consisted of a single-mode fiber (SMF), a gradient index multi-mode fiber (GRINF), and a micro-mirror (M). (C) Photo of the

OCT probe. (D) MRI-compatible titanium needle probe for OCT imaging, with the side-window covered by transparent heat shrink tubing (HST). (E) OCT image of a human finger with microstructures including stratum corneum (SC), epidermis (E), and dermis (D). From ref. [168].

4.2 Materials and methods

Fig. 4-1A shows the picture of the integrated MRI/OCT imaging system, which includes a MRI-compatible robotic device previously invented by our collaborator Dr. Jaydev Desai's group [166]. To work within a strong magnetic field (3T MRI, SIEMENS), we actuate the robot by a pneumatic cylinder instead of a conventional motor. By pressurizing or depressurizing the air chambers in pneumatic cylinder (the pressure is controlled by a pneumatic directional control valve (MPYE-5-1, FESTO) connected to an air compressor), we can move the needle forward or backward. The MRI incompatible pressure control units, including the control valve and the air compressor are outside the MRI room and are connected to the robot through long plastic tubes. The position of the needle is recorded by an encoder with 12.7 μm resolution for feedback control. The smallest step size that is achievable by the pneumatic robot is 1 mm and the response time for 1 mm displacement is 0.2 second. Regarding to the OCT system, the spectrum bandwidth of the swept source OCT laser is 100 nm centered at 1325 nm (SL1325-P16, Thorlabs). Therefore the calculated axial resolution is 7.7/5.9 μm in air/water. The wavelength-swept frequency is 16 kHz with 12 mW output power. The OCT system [41] sitting outside the MRI room is connected to a side-viewing OCT probe (Imagewire, St. Jude Medical) through an 8-mm-long single mode fiber. The side-viewing probe consists of a single-mode fiber for light transmission, a gradient index (GRIN) multi-mode fiber for light focusing and a micro-mirror for beam deflection (Fig. 4-1B & C). The OCT probe (O.D. =

0.23 mm) is placed in a 16 gauge (O.D. = 1.7 mm) titanium biopsy needle (Invivo). A side window is created on the needle to allow the laser beam from the OCT probe to reach the sample and the window is also encapsulated with a transparent heat shrink tubing (HST) for preventing tissue collection (Fig. 4-1D). The measured working distance from the outer surface of the needle probe is 0.2 mm. The HST deteriorates the transverse resolution from 20 μm to 30 μm and the axial resolution remains 15 μm. The sensitivity drop introduced by the HST is minimized to 1-2 dB by filling the needle with water for index matching. The OCT probe is linearly actuated forward and backward along the long axis of the needle by an MRI-compatible PZT actuator (Bending actuators, Piezo Systems) attached at the proximal end. We only use the information from the pull-back direction, because it is difficult to insert a flexible fiber linearly from a distal site. Although we only use half of the information, the tissue is under oversampling. With 1mm/s needle insertion speed and 18.3 mm/s sampling rate (15 Hz frame rate and 1.22 mm scanning range), the overlap between OCT images is 94%. However, oversampling can provide us additional information, such as the tissue deformation, elastography and Doppler flow. On the other hand, the spiral scanning may be more efficient, but it is also more complex and expensive to build an MRI-compatible rotary motor. Instead, if the tissue is relative homogeneous in transverse direction, a simple PZT bender that allows us to detect the transition between layered structures is sufficient. Fig. 4-1E shows an example OCT image of a human finger. The microstructures beneath the skin surface, including stratum corneum (SC), epidermis (E), and dermis (D) can be clearly identified. Sweat glands

are also visible as spiraling columns in the SC region. The PZT actuator and the OCT needle probe are moved in tandem driven by the pneumatic actuator.

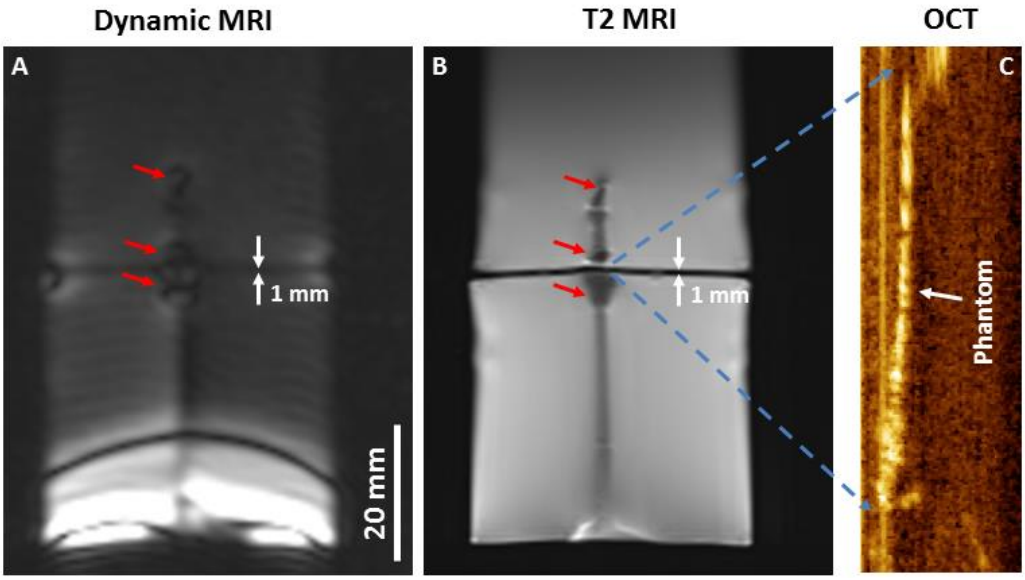

Fig. 4-2. Co-registration of MRI and OCT images using a custom-made phantom.

(A) Dynamic MRI and (B) high-resolution T2 MRI images of the OCT needle and the plastic sheet phantom (indicated by white arrows). The artifacts from sharp edges on the needle tip and the side window are indicated by red arrows. (C) Concurrent OCT image of the plastic sheet phantom. OCT FOV covers the entire 1 mm thickness of the phantom for co-registration of OCT images with low-resolution dynamic MRI and high-resolution T2 MRI images. From ref. [168].

We use a custom-made phantom to co-register the MRI and OCT images. A plastic sheet (thickness = 1 mm) with holes that are large enough for the OCT needle to pass through is immersed in a water-filled container. The OCT needle goes through a hole on the phantom until the side window lines up with the plastic sheet so that the reflection from the plastic sheet is visible in OCT image (Fig. 4-2C). The OCT laser beam is pointed downward (i.e., the plane containing the OCT needle central axis and OCT beam is normal to the MRI table). In MRI images (Fig. 4-2A & B), the plastic sheet (white arrows), the needle and the artifacts from the needle tip and the side window (red arrows) are clearly visible. Since the OCT imaging window has been aligned with the plastic sheet (Fig. 4-2C), the sheet in the MRI images indicates the

corresponding location of the OCT window. Therefore, we can locate the OCT window in MRI image and measure the distance from the OCT window to the needle tip. Although the encoder can track the needle position with 12.7 μm resolution, the accuracy of co-registration cannot be better than the resolution of MRI (~ 1mm). It may be difficult to achieve sub-mm co-registration, but the targeting precision is only limited by how accurate OCT can determine the boundary surrounding the target and it is not limited by the resolution of MRI.

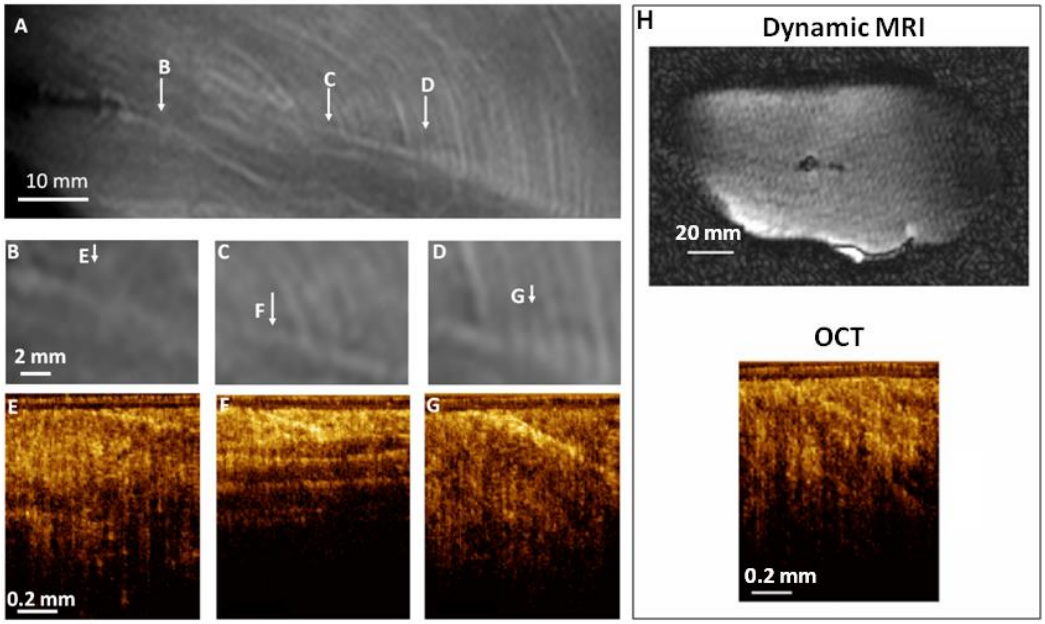

Fig. 4-3. Co-registered MRI/OCT images of chicken breast tissues ex vivo.

(A) High-resolution T2 MRI image with arrows "B", "C", "D" indicating the positions of corresponding enlarged MRI images shown in (B-D). (E-G) The OCT images corresponding to the location "E", "F", "G" shown in (B-D). (H) Concurrent dynamic MRI and OCT imaging of chicken breast tissue during needle insertion. From ref. [168].

4.3 Results and discussion

In the first study, we demonstrate the multi-scale imaging on the chicken breast tissue ex vivo. We place the chicken breast in a wrist coil (SIEMENS) for MRI imaging. High-resolution T2 MRI images (4 minutes per frame) are acquired before

needle insertion to plan the trajectory and after needle insertion to verify the final location. Although high-resolution T2 MRI can resolve the millimeter-scale structures (Fig. 4-3A), the long image acquisition time (several minutes) makes it impossible for real-time guidance. Fig. 4-3B-D show the enlarged MRI images of the area indicated in Fig. 4-3A by “B”, “C”, “D”. Fig. 4-3E-G are the corresponding OCT images to the area indicated by “E”, “F”, “G” in Fig. 4-3B-D. The correlation between MRI and OCT is based on the calibration shown in Fig. 4-2. Fig. 4-3 shows the MRI and OCT images extract from the same location. However, due to huge difference on resolution and contrast, MRI and OCT images may look very different. At the position “B”, the needle is in a homogeneous muscle tissue and its corresponding OCT image (Fig. 4-3E) also shows similar feature. At the position “C”, the needle is very close to a fibrous connective tissue. The corresponding OCT image (Fig. 4-3F) shows the same structure with few finer fibers beneath it. At position “D”, the OCT image reveals fine connective tissues within muscular tissues. Fig. 4-3H shows the concurrent dynamic MRI and OCT imaging during needle insertion. Low-resolution dynamic MRI (1 frame/s) provides the general needle location and the real-time OCT (15 frames/s) reveals the microstructures surrounding the needle. Therefore, the operator can estimate in real-time the distance to the target from the dynamic MRI image and decide whether the needle reaches the target based on the OCT tissue architecture. The nonlinear motion is obvious while the needle was being inserted into the chicken breast and it affects the uniformity of some OCT images. The encoder cannot correct the distortion caused by the deformation of the needle or the tissue. Therefore, the speckle cross-correlation function [169, 170] that can measure the distance between

A-lines directly from the OCT image and correct the imaging distortion should be integrated with the future system to improve the uniformity.

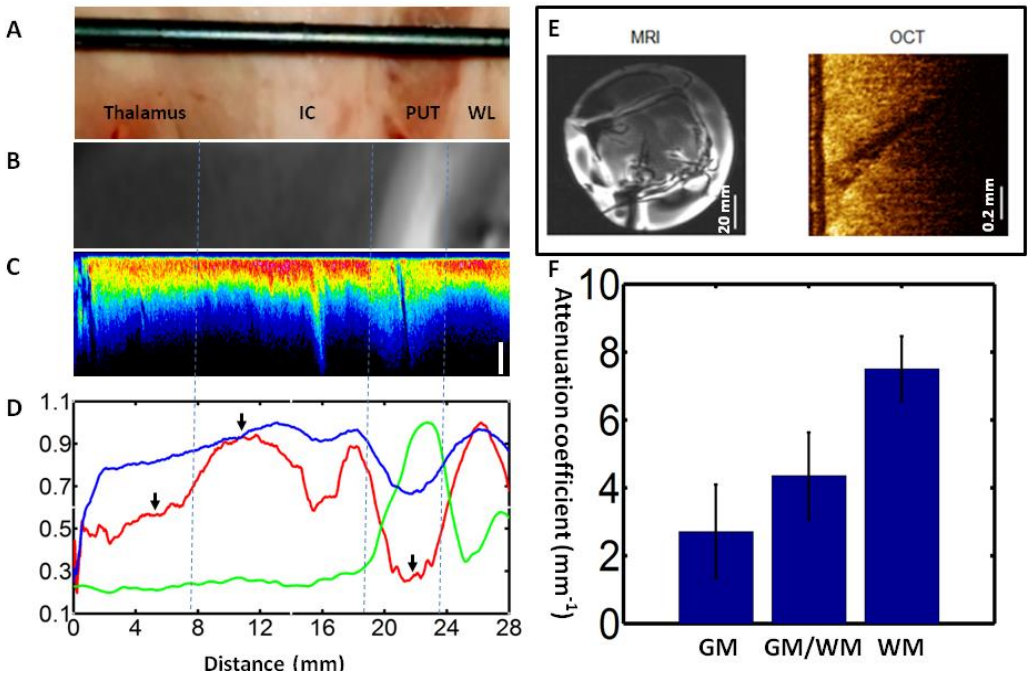

Fig. 4-4. Co-registered MRI/OCT images of human basal ganglia ex vivo.

(A) Photo of the human brain tissue containing basal ganglia. Different tissues types are visible, including white matter lamina (WL), putamen (PUT), internal capsule (IC), and thalamus. The OCT needle probe is sitting on top of the tissue indicating the insertion track (the actual insertion track is beneath the tissue surface). (B) T2 MRI image of the brain slice. (C) Full-tack OCT with co-registered lateral position with MRI. The axial dimension is expanded for better visualization. The scale bar for the axial dimension is 0. 5mm. (D) Plot of normalized MRI intensity (green), normalized OCT backscattering intensity (blue) and normalized OCT attenuation coefficient. (E) Concurrent dynamic MRI and OCT imaging of human brain tissue during needle insertion. (F) The attenuation coefficient of GM (PUT), GM/WM mixture (thalamus) and WM (IC). The p values between data sets are smaller than 0.0001. From ref. [168].

We image an ex vivo human basal ganglia to validate MRI/OCT for neurosurgery guidance. Intra-operative MRI (iMRI), which provides large FOV and direct visualization of brain targets in operation, has been applied to stereotactic neurosurgery, including brain tumor biopsy [113], catheterization [114] and deep brain stimulation [115, 164]. However, the resolution and the contrast of MRI are not good enough to detect certain nuclei in basal ganglia [117]. On the other hand,

researchers have used OCT to locate these nuclei in hurman brain ex vivo [40] and in rat brain in vivo [43] . We place a slab of frozen human brain tissue containing basal ganglia in a gelatin holder filled with saline at room temperature and wait until it is completely thawed. Then, we acquire a few pre-operative T2 images (4 minutes per frame) to plan the trajectory. We monitor the advancement of the needle by the dynamic MRI (1 frame/s) and OCT imaging (15 frames/s) in real time (Fig. 4-4E). We can easily identify the boundary between the gray matter (GM, low intensity with deep penetration) and the white matter (WM, high intensity with shallow penetration) while most of structures are occult in the dynamic MRI (Fig. 4-4E). Fig. 4-4A shows a picture of a brain tissue. In the high-resolution MRI image (Fig. 4-4B), the transitions between the GM nucleus, putamen (PUT, white on T2 image) and its surrounding WM bundles, white matter lamina (WL) and internal capsule (IL) (dark on T2 image) are clearly visible. We reconstruct a full-track OCT image (Fig. 4-4C) from the OCT video and correlate it with the large-scale MRI morphology. From each frame of the OCT video, we select a band of A-lines with 66.67 μm width (1mm/s sampling rate, same as the needle insertion speed) from the same location. Then, we stitch these bands together to form Fig. 4-4C. We align the per-operative MRI to the intra-operative OCT images by matching them respectively to the dynamic MRI images. The accuracy of the alignment is limited by the resolution of dynamic MRI images, which is 2 mm. In Fig. 4-4D, we plot the normalized MRI intensity (green line), normalized OCT backscattering intensity (blue line) and the normalized attenuation coefficient (red line). The normalized OCT attenuation coefficient and OCT surface scattering in Fig. 4-4E are smoothed for better visualization by a moving

average filter with 2.35 mm average width. In the full-track OCT image, the transitions between PUT and its surrounding WM bundles (WL & IC) are obvious and are well correlated with the MRI image. The full-track OCT shows that the GM nucleus (PUT) has lower backscattering intensity, deeper penetration depth and thus smaller attenuation coefficient (Fig. 4-4D), while myelinated WM tracks have higher backscattering intensity, shallower penetration depth and larger attenuation coefficient. This result agrees well with previous studies [159]. It is worth note that the transition from IC to thalamus is not visible in MRI image. The thalamus is a GM nucleus containing uniformly distributed WM fibers. The mixture of WM and GM gives it a very low contrast to the surrounding WM tracks in MRI image. However, we can easily identify the boundary between IC and thalamus in OCT image. Compared to the PUT, high level of WM in thalamus reduces the optical penetration depth and increase the attenuation coefficient (Fig. 4-4D). Also, the backscattering intensity from the thalamus is not as high as in the WM bundles. This result agrees with a previous study [40]. Fig. 4-4D shows that the transitions between PUT and its surrounding tissues are obvious in both imaging modalities, but only OCT provides good contrast between IC and thalamus. Fig. 4-4F shows that the attenuation coefficient of thalamus (GM /WM mixture) is between IC (WM) and PUT (GM) and the difference is statistically significant ($p<0.0001$). The attenuation numbers in Fig. 4-4F are calculated from a 1 cm wide unsmoothed data at the location indicated by the black arrows in Fig. 4-4D. This result suggests that OCT can discern the MRI-occult nuclei in basal ganglia with a different contrast. Contrast in MRI images depends on the magnetic property of the tissue. The signal from protons with shorter

T2, (for example, protons in lipids) will decay faster than protons with longer T2 (For example, protons in water) and will appear with lower signal intensity. Therefore, the white matter, which consists of densely packed lipid membranes, has lower intensity than other tissues in T2 image. Lipids are also strong optical scatters and give bright intensity in OCT image [40, 41, 159]. Densely packed axon fibers in white matter region contain high concentration of lipids and thus has strong OCT signal with shallow penetration depth. Although the source of the contrast of both imaging modalities comes from two different physical phenomena, OCT is able to produce images at a very high resolution over a small field of view. Such high resolution is currently not possible with MRI. However, the two techniques can complement each other, where MR images provides guidance to an OCT catheter to a specific location from where high resolution images could be obtained. The combination of the two technologies enables one to span the resolution scales afforded by each of the modalities.

In conclusion, we develop a multi-scale MRI/OCT imaging system with tele-operated robot from Dr. Jaydev Desai's group that has potential to improve the accuracy and efficiency of iMRI procedures. Real-time OCT images can fill the gap between pre- and post- operative MRI images and thus allow operators to reach the target more efficiently. Moreover, high-resolution OCT imaging provides microstructural information and different contrast that can be useful for detecting MRI-occult tissue landmarks. Therefore, combining large FOV MRI with high-resolution OCT is a promising guidance tool for high-precision surgery. Future works

will include the investigation of the impact of physiological motion (breathing, etc.) and biofouling (bleeding, etc.) on targeting accuracy under in vivo conditions.

Chapter 5: Coherence-gated Doppler: a fiber sensor for precise localization of blood flow[4]

5.1 Introduction

The needle-type forward-imaging OCT probe (chapter 2) and MRI/OCT imaging system (chapter 3) are promising tools that can potentially transform the neurosurgery guidance, but we also need a simpler device that can be integrated with conventional guidance tools and improve their safety.

Detecting blood vessels in front of a surgical probe in real-time is an important capability during interventional procedures. This may provide the ability to minimize laceration of vessels during stereotactic neurosurgery, avoid vessels during local anesthesia procedures deep inside the body, and locate vessels during central venous/arterial cannulation. Ultrasound is currently used for real-time image guidance and blood vessel localization for some of these interventional procedures. However, in some cases, such as neuraxial blockade, ultrasound guidance is especially challenging because of the complex encasement of bones that allows only a very narrow acoustic window for the ultrasound beam [171]. Furthermore, the guidance efficacy in some cases is still unsatisfactory due to limited resolution (~ 1 mm) and the need for complex hand-eye coordination [172]. Optical sensors that can be integrated with surgical tools and detect blood vessels in front of instruments provide a solution to these challenges.

[4] The content of this chapter is reproduced from "**C.-P. Liang**, Y. Wu, J. Schmitt, P. Bigeleisen, J. Slavin, M. S. Jafri, C.-M. Tang, and Y. Chen, "Coherence-gated Doppler: a fiber sensor for precise localization of blood flow," Biomed. Opt. Express 4, 760-771 (2013)" with permission.

An effective optical sensor needs to be small, flexible and rugged for integration with minimally invasive instruments. It also needs to have high lateral resolution (< 100 μm) to detect clinically significant blood vessels. Ideally, it should also have sufficient axial detection range to detect blood vessels millimeters ahead. Various optical technologies have been developed to monitor the blood flow. Laser Doppler flowmetry (LDF) has been used in neurosurgery [123], dermatology [173] and dentistry [174] to collect blood flow information. However, the resolution (mm-cm) of the two fiber design in a conventional LDF system is too coarse to allow location and avoidance of many vessels in the brain. Petoukhova et al. improved the axial resolution of LDF to 50 μm by using coherence-gating effect [175]. Although this approach successfully obtained depth-resolved information from the human skin [176], the lateral resolution is not sufficient (few mm [175]) for neurosurgery. Also the two fiber design with wide separation in LDF system is not compatible with minimally invasive procedures. In contrast, Doppler optical coherence tomography (DOCT) creates a very small imaging spot (10 μm) with a single fiber [135]. By scanning this spot, the flow information in the region of interest (ROI) can be mapped out with great resolution. However, in many clinical applications, it is not necessary to obtain high resolution images of blood vessels and accept the tradeoffs associated with imaging. Often what is needed is simply to determine whether there is a blood flow at a precise location in front of a surgical probe. We developed a technology to serve in such situations.

Coherence-gated Doppler (CGD) is a real-time movement sensing technology that can be thought of as a hybrid between optical coherence tomography (OCT) and LDF.

The system design is derived from time-domain DOCT or optical Doppler tomography (ODT) [135] with several important simplifications and modifications. By converting the DOCT imaging system to the CGD sensing system, the reference phase modulator, reference path length scanning, signal digitization and demodulation processing can be omitted. CGD only requires a simple electronic circuit to convert the Doppler beating signal to an audio signal. From the pitch and volume of the audio signal, we demonstrate that the simple CGD system enables us to differentiate tissue, vein and artery in live animals and also demonstrate that the CGD probe can potentially predict the creation of hematomas in neurosurgery.

5.2 Material and methods

5.2.1 System setup

Fig. 5-1A illustrates the design of the CGD system. The light source is a superluminescent diode (SLD) at 1310 nm (Qphotonics QFLD-1300-10S).The wavelength bandwidth of the light source is 3 nm, and thus the coherence length is 190 μm in water. The fiber (FC) coupler splits the photons to sample (90%) and reference arms (10%). The optical fiber circulator sends the illumination light from port 1 to port 2 and the backscattering light from port 2 to port 3. Both back scattering light from the sample and the reference mirror go to another fiber coupler (50/50) and the photons from each arm are re-distributed to two output fibers. The interference fringe from output fibers go to a dual balanced detection system, which rejects the common mode noise. After further amplification and frequency filtering (10 -20,000 Hz), the electronic signal is converted to an audio signal and broadcast by a speaker.

We also collect the signal by a data acquisition (DAQ) card (National Instrument NI-6259) and process it with a computer (optional). The sampling rate of data acquisition is 400 kHz. The fiber probe consists of a single mode fiber (SM) and a GRIN multimode fiber (GM) for focusing (St. Jude Medical). The focal distance is 1.5 mm and the lateral resolution is 40 μm. Fig. 5-1B and Fig. 5-1C illustrates DOCT and LDF system respectively. Please see the comparison between systems in chapter 2.5.

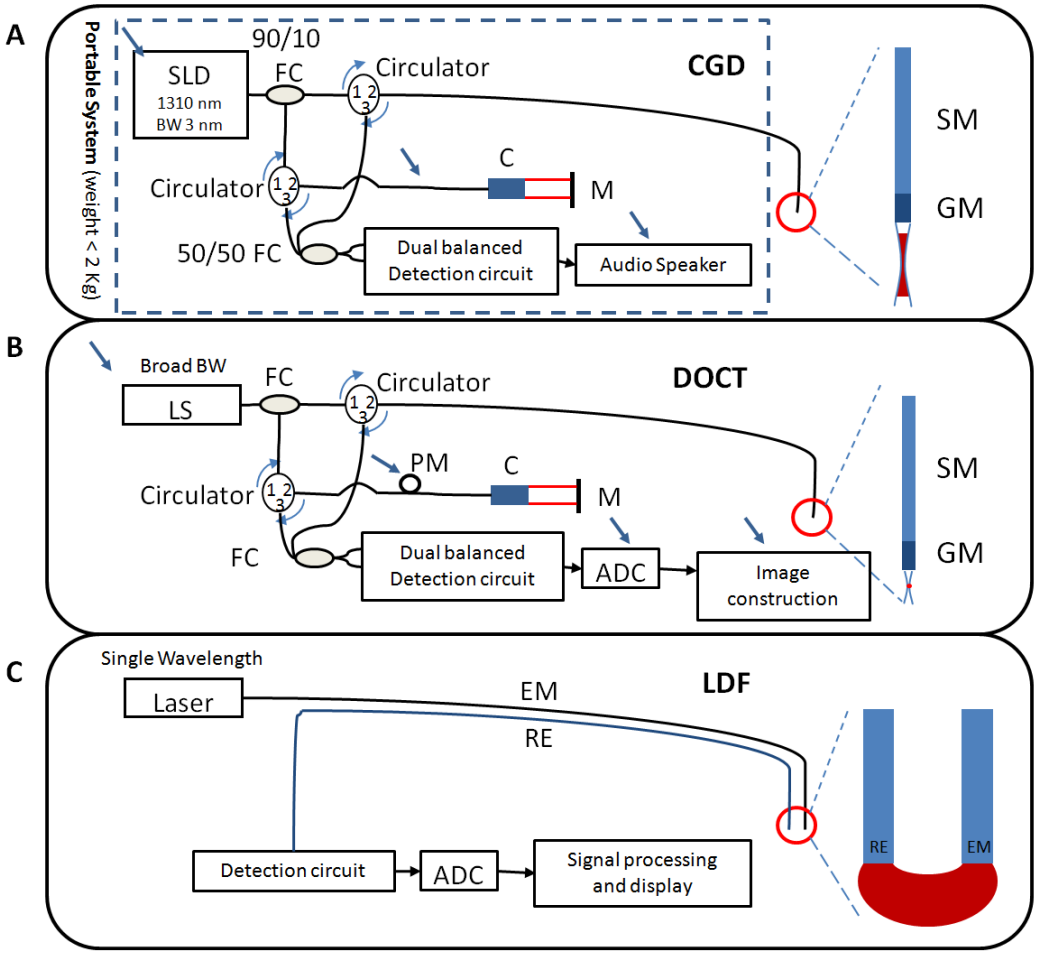

Fig. 5-1. System comparison between CGD/DOCT/LD

(A) CGD system (B) Doppler OCT system (C) LDF system. SLD: superluminescent diode, LS: light source, BW: wavelength band-width, FC: fiber coupler, C: collimator, M: mirror, PM Phase modulator, ADC: analog to digital converter, SM: single-mode fiber, GM, gradient-index fiber, EM: emission fiber, RE, receiver fiber. The detection volume of each system is shown in the probe drawing to the right in red. From ref. [137].

5.2.2 Data processing

The interference between two electric fields with Doppler frequency difference will generate a fluctuating AC signal, whose frequency is equivalent to the Doppler frequency difference. Therefore, the frequency of CGD waveform is equivalent to the Doppler frequency shift, which is linear proportional to the moving speed. The sign of signal does not reflect the flow direction. From the interference fringe, we can only measure the flow speed (the frequency) and the volume of moving scatters (the amplitude), but no information on the flow direction. To quantify the performance of the system, we record the interference fringe by a DAQ card (sampling rate 400 kHz) and calculate the M1 (first moment) factor, $\int \omega * P(\omega) \mathrm{d}\omega$ which is linearly proportional to the average concentration of the scatter multiplied by the root mean square of the velocity [177]. P(ω) is the power spectrum of the interference fringe. The power spectrum of the CGD waveform is calculated by taking Fourier transform and square the amplitude. The time domain window for Fourier transform is 0.1 second and the integration window on frequency domain is 0- 20 kHz. The M1 factor is used to characterize the linearity of speed measurement and detection volume. We also study the similarity of the time domain signal by autocorrelation. Firstly, we square the CGD waveform signal to avoid the cancelation between positive and negative signal. Then, we use the entire signal in the 5 seconds window to calculate the autocorrelation coefficient (Acorr) at different time shift (0-5 seconds). We also calculate the spectrogram from the CGD waveform. The theoretical minimum resolvable frequency is 0 Hz (DC) and the maximum resolvable Doppler frequency is 15MHz (3dB bandwidth), which is limited by the dual balanced detector (Thorlabs

PDB145C). This frequency is corresponding to a flow speed of 9.75 m/s which is well above the fastest blood flow speed in human body (~ 1 m/s) [178]. In practice, the maximum frequency is determined by the sampling rate of data acquisition. In our study, the sampling rate is 400 kHz and thus the maximum frequency is 200 kHz (Nyquist limit). The minimum resolvable frequency is determined by the time window of short time Fourier transform (STFT), which is 0.1 second. Therefore, the resolution in frequency domain is 10Hz. The minimum (10 Hz) and maximum (200 kHz) frequency are corresponding to Doppler velocity of 0.0065 mm/s and 130 mm/s respectively. The signal frequencies within human audible range (< 20 kHz) are displayed. A median filter is applied to improve visualization.

5.2.3 Capillary phantom

We constructed a vessel phantom by injecting 2% Intralipid solution through a capillary tube (I.D. = 0.4 mm), with the flow speed controlled by a motorized pump (Newport CMA-25CCCL). The velocity dynamic range, limited by the pump system, was 0.2-5 mm/s.

5.2.4 In vivo rat femoral vessel detection

All animal procedures were approved by the Institutional Animal Care and Use Committee (IACUC) at the University of Maryland, and animals were treated in accordance with the PHS Policy on Humane Care and Use of Laboratory Animals, the National Institutes of Health Guide for the Care and Use of Laboratory Animals, and the Animal Welfare Act (7 U.S.C. et seq.). Anesthetized (ketamine 50 mg/kg and xylazine 5 mg/kg, intraperitoneal) Sprague-Dawley rats (n = 2, male, wt. ~400 g) in

supine position have their femoral vessels exposed. The blood vessel color and relative position to the femoral nerve allow visual identification of the artery and vein. We place the CGD probe 3 mm away from the exposed vessels and translated the probe laterally to acquire information from tissue, vein and artery. The audio signal is recorded by a voice recorder (Sony, ICD-PX720).

5.2.5 In vivo deep sheep brain vessel detection

The effectiveness of the CGD probe was evaluated by examining its ability to detect vessels below the surface of the male sheep brain (wt. ~100 kg). Anesthesia is induced with 5 mg/kg ketamine (IV) and maintained under 1-4% isoflurane in 100% oxygen. After the sheep is deeply anesthetized, craniotomy is performed. The dura and pia membrane on the surface are carefully removed. Then, the CGD probe is inserted by hand. The inset of Fig. 5-2 shows the CGD probe placed in a 30 G needle and Fig. 5-2 shows the picture of a CGD probe being inserted into sheep brain in vivo. We also placed an US probe (Edge model, FUJIFILM SonoSite, Inc.), directly on top of the brain tissue to monitor the relative position between CGD probe and blood vessels. The US images are synchronized with CGD audio by the corresponding time marks.

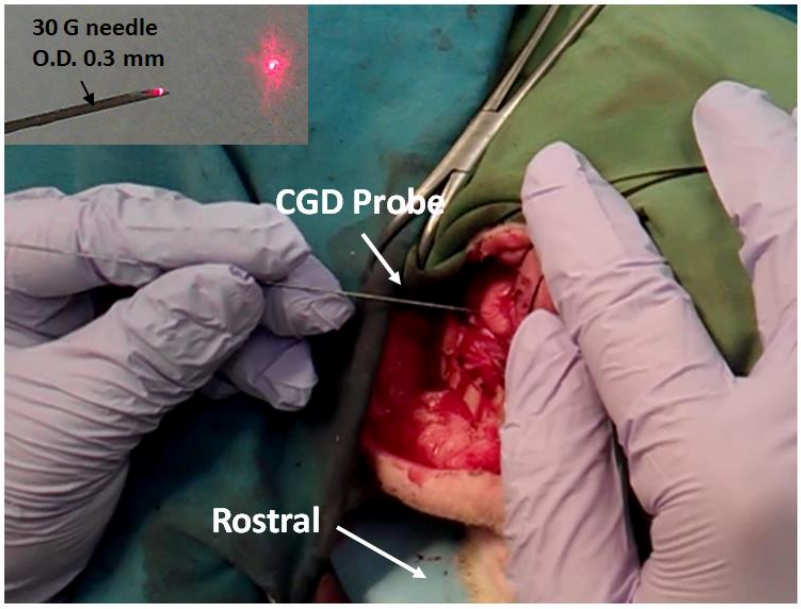

Fig. 5-2. A CGD probe during insertion into sheep brain.

From ref. [137].

5.3 Results

5.3.1 CGD system characterization

Fig. 5-3 shows the linearity of the flow speed, as measured by the capillary phantom. CGD shows good linearity and the R-squared value is very close to 1. We also tested whether the CGD probe can resolve a capillary in a highly scattering environment. The vessel phantom was immersed in 2 % Intralipid solution, and the flow speed parallel to the probe is 1.5 mm/s. The inset of Fig. 5-4A shows the DOCT B-scan image of the capillary. We scanned the CGD probe across the vessel and Fig. 5-4A shows the CGD probe can easily profile the parabolic flow in this 0.4 mm capillary (CGD probe is 0.4 mm away from the top surface of capillary). This result shows the great targeting capability of a CGD probe in a highly scattering environment. Also we characterized the axial detection range by placing the CGD probe at different axial positions from the capillary (Fig. 5-4B). At the zero point, the

CGD probe contacted the capillary and signal is close to the background signal level. From 0.18 - 0.71 mm the signal is significantly higher than the background level.

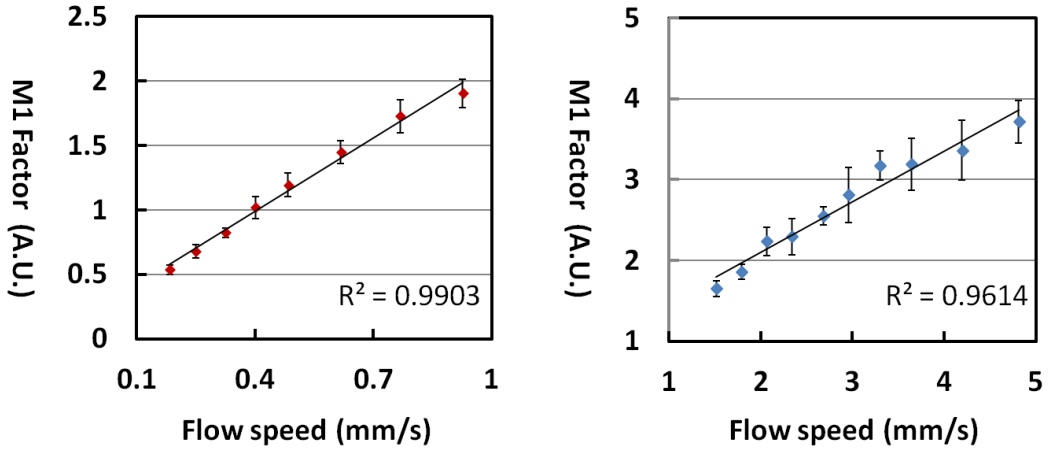

Fig. 5-3. Linearity of flow speed measurement within two ranges.

From ref. [137].

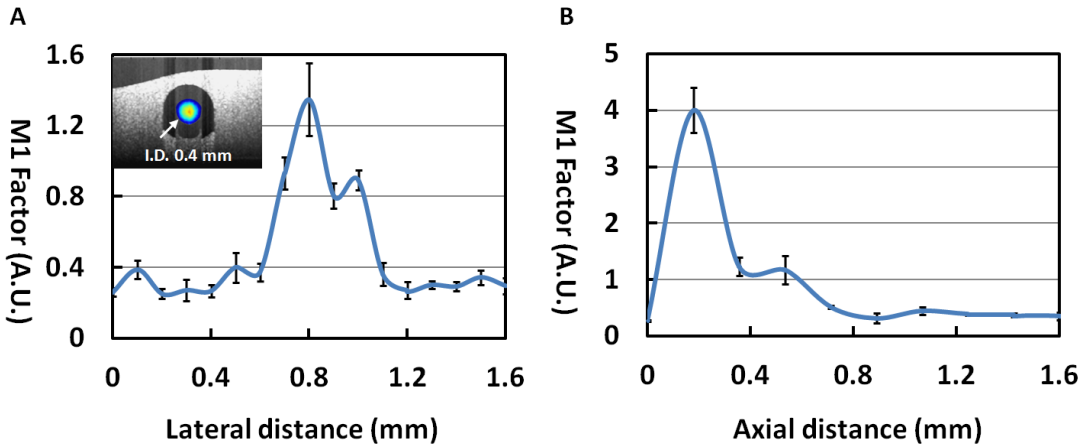

Fig. 5-4. Lateral and axial spatial specificity test of the CGD probe.

(A) Signals measured while scanning the CGD probe (0.4 mm away from the top surface of capillary) laterally across a capillary tube immersed in 2% Intralipid solution. The inset shows a DOCT B-scan image of the phantom. The flow speed in the capillary is 1.5 mm/s parallel to the CGD probe. (B) Axial detection range. Moving a CGD probe axially away from a capillary immersed in 2% Intralipid solution. From ref. [137].

5.3.2 Rat femoral vessel flow measurements

To test the feasibility of vessel detection and differentiation, we place the CGD probe on top of exposed rat femoral vessels (Fig. 5-5A). The femoral artery and vein can be clearly distinguished by their appearance (i.e. color, size, and pulsatile

movement). They are separated from each other by 1 mm. The CGD signals of the muscle tissue, vein and artery are also clearly apparent (Fig. 5-5B-D). Because the surrounding muscle tissue is not moving, its Doppler signal shows few high frequency components. After DC filtering, it has much smaller amplitude than the signal from the vessels. Also, we can see that the bulk motion generated a sharp peak, which represents large volume of scatter moving all together. The signal from the vein (Fig. 5-5C) shows steady flow of blood cells, with frequency characteristics different from those of the pulsating artery (Fig. 5-5D). The pulsating voltage represents the variation of the volume of moving blood cells during a pulsation cycle. Note that the CGD probe can easily differentiate two vessels that are only 1 mm apart at the distance 3 mm away from the sample. This result demonstrates that the CGD probe can differentiate the neighboring vessels at a distal location far from the zero-delay plane (the zero-delay plane is matched with the focal plane at 1.5 mm distance from the fiber surface). Unlike heterodyne detection which can only obtain the signal close to the zero-delay plane, homodyne detection enables us to obtain the signal along the illumination path. This capability provides us longer buffer distance before hitting the vessel, which can be beneficial for avoiding hemorrhage. The amplitude of artery is smaller than vein, because the thicker arterial wall allows less photons to interact with the moving blood cells.

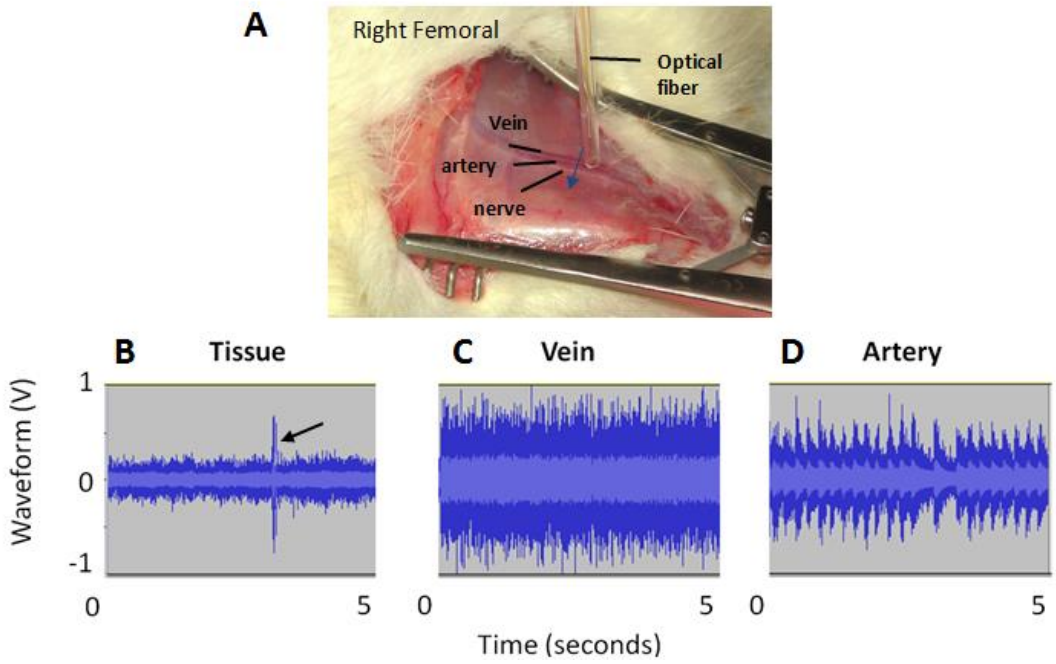

Fig. 5-5. In vivo rat femoral blood vessel test.

(A) Exposed rat femoral vessels and CGD probe inside a large outer guide. CGD probe is 3 mm away from the sample. Voltage waveform from (B) rat femoral tissue, (C) vein, and (D) artery. Arrow indicates bulk motion. From ref. [137].

5.3.3 Sheep brain vessel detection

Next, we tested the performance of the CGD needle probe (Fig. 5-2) for detecting vessels deep in the sheep brain. Fig. 5-6 shows the voltage waveform and the spectrogram from tissue (Fig. 5-6A), vein (Fig. 5-6B), and artery (Fig. 5-6C). When the CGD probe is surrounded by highly scattering brain tissues, any relative motion between the probe and the brain generates very strong Doppler signal. The spectrogram shows that the signal is strong (large volume of scatters) with focused frequency range (uniform speed). In contrast, the signal from a vein is more homogeneous in the frequency domain. The waveform of an artery shows the pulsation pattern, and the spectrogram reveals the speed variation during a pulsation cycle. When the insertion motion (tissue movement with respect to the CGD probe

during insertion) signal is mixed with the artery signal, it may be challenging to differentiate them in the spectrogram. However, if we study the similarity of the time domain signal by autocorrelation (Acorr), we can see the clear difference between the bulk motion and the artery. We find that the difference of the frequency distribution between different spikes in the bulk motion spectrogram generates irregular fluctuation on Acorr, which is distinctively different from the periodic Acorr of the artery. In Fig. 5-6A, from 4.5 second to 5 second (indicated by the red arrows), the probe is static and the motion is significantly lower than the signal in other time period. Acorr of the vein remains in a constant level due to the homogeneity of the signal.

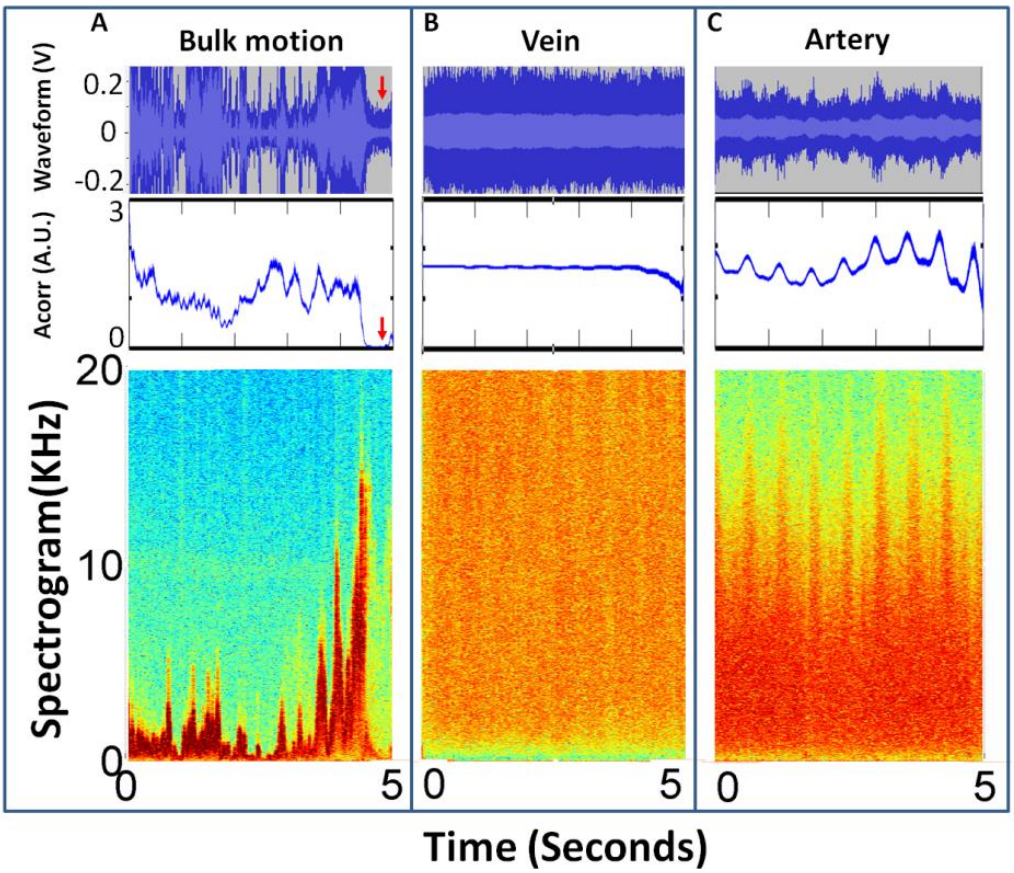

Fig. 5-6. CGD waveform, autocorrelation coefficient and spectrogram of brain vessels.

(A) Inserting the probe, (B) a vein, and (C) an artery in sheep brain in vivo. The red arrows indicate the time point when the CGD probe is static relative to the brain tissue. From ref. [137].

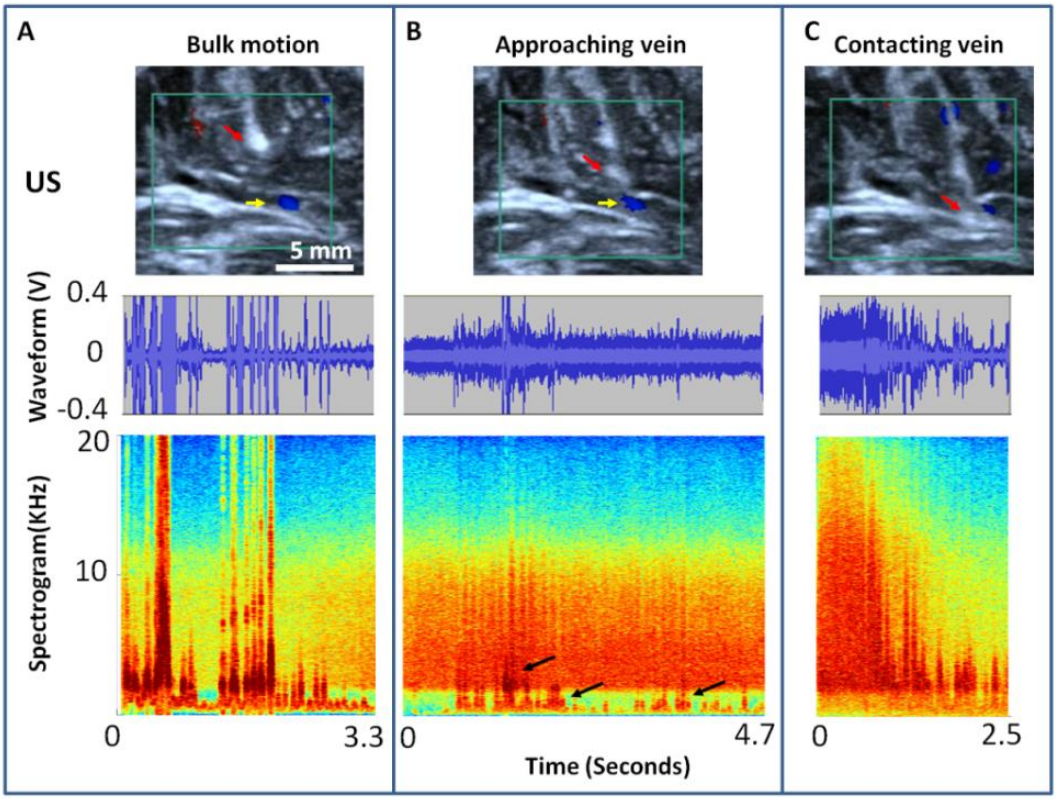

Fig. 5-7. Ultrasound imaging with the CGD flow detection in sheep brain in vivo

Ultrasound monitoring with Doppler detection of the CGD probe as it approaches a vessel (yellow arrows) in a sheep brain in vivo. The CGD probe tip appears as the bright white spot (red arrows). The target vein is the blue spot in the insets in top panel. (A) Insertion motion away from the vein, (B) approaching the vein, and (C) pressing on the vein resulting in the disappearance of the ultrasound Doppler signal as well as the CGD signal. From ref. [137].

5.3.4 US-guided CGD vessel detection

To verify that the CGD probe can detect blood vessels in highly scattering tissues, we pushed a CGD probe toward a blood vessel in the sheep brain under US guidance. Fig. 5-7A shows the situation when the probe (indicated by red arrow) is 1-4 mm away from the vessel (indicated by yellow arrow). The signal is dominated by insertion motion. The blood flow signal was initially detected at distance 3 mm in front of needle. Similar to the signal from the brain vessel data (Fig. 5-6A) the insertion motion has high intensity and focused frequency distribution. As the probe approaches the vessel (< 1mm), the blood flow signal shows a uniform frequency

distribution (Fig. 5-7B). Fig. 5-7B also shows the situation when the blood flow signal is mixed with insertion motion signal (indicated by black arrows). Lastly, when the CGD probe comes in contact with the vessel, the blood flow signal initially becomes stronger followed by a loss of the CGD flow signal. The probe is advanced until it constricts the flow and the ultrasound signal is lost; the CGD signal also attenuates.

5.4 Discussion

We have developed a thin (0.125 μm) and flexible CGD fiber probe that can detect at-risk blood vessels with real-time audio feedback up to 3 mm in front of advancing needle in brain tissue in vivo. The diffuse optics design of laser Doppler flowmetry (LDF) with sample volume in the mm to cm range often includes signal from surrounding tissues and thus is not ideal for applications required high spatial specificity. The CGD probe with confocal optics design enable us to target a 0.4 mm capillary (Fig. 5-4A) and differentiate blood vessels that are only 1 mm apart (Fig. 5-5). On the other hand, Doppler optical coherence tomography (DOCT) has high spatial resolution (~ 10 μm), high temporal resolution (40 Hz) and wide flow speed dynamic range (7 μm/s to 52 cm/s) [160], but it requires extensive post processing and an expensive system to obtain the high resolution images. In contrast, CGD is a simple, robust and low-cost sensing system, which provides an audio signal that is rich in content, yet is easy for the operator to interpret (Fig. 5-5 & Fig. 5-6). Real-time temporal resolution (10 Hz) and broad electronic detection bandwidth (10-20,000 Hz) allows us to differentiate the signals from artery, vein and motion artifact (Fig. 5-6 & 5-7).

In order to achieve the best balance between the depth sensitivity and resolution, we carefully choose the 190 μm coherence length (CL). In ideal case, we hope to detect a blood vessel few millimeters away with sub-mm lateral specificity. Shorter CL provides higher resolution but also limits the depth detection range. We have used an SLD with 43 nm bandwidth at 1.325 μm center wavelength and found that it can only detect a vessel within 60 μm depth range, which is too short to prevent hemorrhage. Therefore, we further relax the detection range to 0.5 mm (Fig. 5-4B) by increasing the CL to 0.19 mm. In the animal study, Fig. 5-7 shows that it can detect a blood vessel that is 3 mm away due to longer transportation mean free path in the brain. On the other hand, if we further relax the CL to mm level, it may further improve the depth detection range, but may also include diffuse photons from the background tissue resulting in poor spatial specificity. We have to maintain the lateral resolution at sub-mm level in order to avoid the millimeter-sized blood vessels. Therefore, a light source with CL close to the mean free path of scattering tissues (~ 0.1 mm [179]) provide us the best balance between the detection range and the resolution.

We also choose the confocal probe design for optimal depth sensitivity. Without beam focusing and the confocal effect, a collimated beam may allow us to detect a blood vessel further ahead. However, in the scattering tissues, most of signal obtained by a parallel emitting probe will be from the tissue that is immediate proximal to the probe surface. On the other hand, a focused beam can deliver higher intensity to the deep tissue and thus provide better sensitivity at the distance further away from the

probe. Therefore, a focused beam provides longer buffer distance before hitting the blood vessel than a collimated beam and thus has better chance to avoid hemorrhage.

CGD is best suited for situations that require multitasking rather than tasks requiring precise image guidance. As shown in Fig. 5-5B, if the probe is static relative to the tissue, the amplitude of audio signal is low. When the probe reaches blood vessels, a high volume of flowing scatterers generates a much louder signal, and the artery shows a clear pulsatile pattern. From the spectrum analysis (Fig. 5-6), we find that the insertion motion has a narrow frequency distribution, while the movement of red blood cells in vessels is associated with a more homogeneous frequency distribution. The audio signals from blood vessels are more like white noise, which is clearly distinctive from the loud chirpy sounds associated with needle insertion (Fig. 5-6). The pulsatile nature of arterial flow clearly distinguish venous and arterial flow. Acorr analysis also shows the clear difference between insertion motion, vein and artery (Fig. 5-6). The downside of the Acorr analysis is that it requires a long time window (couple seconds) that includes several heart beats and thus it cannot be implemented in real-time system. However, in real surgery, most of instruments are advanced slowly and provide us long acquisition time. Also, since most of bulk motion signal are from the relative movement between the probe and the tissue, stopping the probe is actually the most effective way to suppress the motion signal (Fig. 5-6A 4.5 to 5 seconds). Therefore, we envision that the probe should be advanced slowly if a suspicious vessel is detected and then we can use the Acorr to analyze whether it is a pulsating artery. We will perform more animal experiments in the future to evaluate the false positive rate.

One limitation of CGD is that it can only provide a semi-quantitative distance measurement based on the volume of audio signal. The strength of volume, however, also varies with the tissue scattering coefficient and the number of moving scatters. Therefore, we may detect blood vessels further away in the gray matter (low scattering) than in the white matter (highly scattering) and detect a large blood vessel further ahead than a small vessel. However, in the clinical settings, if there is a blood vessel with strong signal sitting ahead, we should stop the probe no matter how far it is from the vessel. In the future, we will perform more animal studies to determine the criteria for stopping the probe.

It is worth to note that CGD may not detect small vessel (~ 10 μm) at 90 deg angle when the probe is very close to the vessel. The mean free path (MFP) in brain tissue is around 0.15-0.3 mm [159]. Beyond this ballistic scattering regime, multiple scattering events effectively randomize the photon propagation direction resulting in random incident angles to the moving blood cells. Therefore, we should be able to detect the laminar flow from any angle at the distance > 0.3 mm to the blood vessel. When the probe is proximate to the vessel, however, the illumination becomes more directional and the effective incident angle depends on the scattering property of blood cells. If the diameter of the vessel is comparable to the MFP of blood (~ 7 μm [180]) , we will not be able to acquire the Doppler signal at 90 degree. For vessel that is much larger than 7 μm, multiple scattering between blood cells will randomize the incident angle and enable us to acquire the Doppler signal from any angle. In the practical situation, we hope to stop the probe at the position > 0.3 mm away from the

high-risk blood vessels that are millimeters in size. Under this circumstance, we should not encounter the angle issue.

CGD probe is a great complimentary technology to tomographic techniques. We can use the wide filed-of-view tomographic imaging such as ultrasound to deliver the CGD probe to the region of interest and perform precise targeting with high precision (<0.1 mm) CGD local information/feedback. Fig. 5-7 shows that the CGD probe is capable of detecting blood vessels that are on average 3.4 ± 1.3 mm from the tip of the probe. With millimeters axial detection range and lateral tissue confinement, we can aim the probe to a brain vessel for tens of seconds (Fig. 5-7).The signal was found to become stronger when the CGD probe contacted the blood vessel. Further advances of the CGD probe resulted in the loss of both the CGD and the US Doppler signal and an ultrasound pattern suggestive of a hematoma is then formed in proximity to the blood vessel. On the other hand, many needle-based procedures are still performed without imaging guidance due to the limitations of technology. For example, in stereotactic neurosurgery, the skull blocks most of ultrasound signal and it is difficult to fit the ultrasound probe to the small opening along with surgical instruments. Therefore a thin CGD probe (<30 G) that can be easily integrated with surgical instruments and provide real-time feedbacks on local blood flow in front of the probe tip has great potential to improve the safety of these “blind” procedures. CGD probe is thin (~ 0.125 mm) and can be embedded within the outer tubing of the needle and can aim at the ROI by using forward or side viewing probes. Integrating fiber sensor with needle has been published previously [181]. A similar design can be adapted for CGD probes.

5.5 Conclusion

Coherence-gated Doppler (CGD) provides the means for detecting blood flow with higher spatial resolution and with a smaller, more robust probe than conventional laser Doppler flowmetry at a cost of shorter depth of view. This tradeoff favors interventional procedures that require insertion of thin probes deep into tissue and where small vessels need to be detected with high precision.

Chapter 6: Real-time Monitoring of Photo-immunotherapy Using Optical Coherence Tomography

6.1 Introduction

Photo-immunotherapy (PIT) is a cell-specific cancer therapy with minimal side effects which is based on an armed antibody conjugate that induces rapid cellular necrosis after exposure to near-infrared (NIR) light. This novel treatment is developed by Dr. Hisataka's group from NCI. The conjugate consists of a hydrophilic photosensitizer phthalocyanine dye, IR700, which is covalently bound to a humanized monoclonal antibody. When exposed to NIR light, the conjugate induces highly selective and rapid cancer cell death both in vitro and in vivo [16, 17]. It has been hypothesized that selective destruction of the perivascular layers of cancer cells by PIT leads to expansion of the tumor vessel diameter and results in a 24-fold increase in the accumulation of various nanomaterials in the tumor bed. This effect is most marked for nano-sized molecules including nano-scale anti-cancer drugs and thus reflects a relative increase in permeability of vessels for larger molecules [18]. This effect has been termed super-enhanced permeability and retention (SUPR) to differentiate it from the more modest enhanced permeability and retention (EPR) that is commonly seen in tumors. Histology and fluorescence imaging with fluorescently labeled macromolecules, confirms that high concentrations of non-specific nanomaterials can permeate into the tumor bed after PIT. However, little is known about the specific effects of PIT on vessel size and blood flow changes at a microscopic level. In this study, we used intra-vital optical coherence tomography (OCT) to monitor the dynamics of the tumor vasculature during PIT.

6.2 Material and methods:

6.2.1 Tumor model and PIT

All in vivo procedures were conducted in compliance with the Guide for the Care and Use of Laboratory Animal Resources (1996), U.S. National Research Council, and approved by the local Animal Care and Use Committee. Six- to eight-week-old female homozygous athymic nude mice were purchased from Charles River (NCI-Frederick). Two million A431 cells were injected subcutaneously in the right dorsum of the mice. Tumors reaching approximately 50 mm^3 in volume were selected for study. The conjugate of panitumumab (antiEGFR antibody) and IR700 was synthesized as previously reported [17]. Briefly, panitumumab (1mg, 6.8nmol; Amgen, Thousand Oaks, CA, USA) was incubated with IR700 (IRDye 700DX NHS ester; 60.2μg, 30.8nmol, 5mmol/L in DMSO; LI-COR Bioscience, Lincoln, NE, USA) in 0.1 mol/L Na2HPO4 (pH 8.5) at room temperature for 30 min. The mixture (Pan-IR700) was purified with a Sephadex G50 column (PD-10; GE Healthcare, Piscataway, NJ, USA). The protein concentration was determined with a Coomassie Plus protein assay kit (Thermo Fisher Scientific Inc., Rockford, IL, USA) by measuring the absorption at 595 nm with spectroscopy (8453 Value System; Agilent Technologies, Santa Clara, CA, USA). The concentration of IR700 was measured by absorption with spectroscopy and the number of IR700 molecules per panitumumab was adjusted to approximately 4. One hundred micrograms of Pan-IR700 was injected intravenously via the tail vein of a mouse 24 hours before PIT. The A431 tumor was treated with continuous NIR irradiation by 690nm laser system (BWF5-690-8-600-0.37; B&W TEK INC., Newark, DE, USA) at a power density of 167

mW/cm^2 for 10 min (100J/cm^2). As controls, tumors in tumor bearing mice were irradiated by NIR without Pan-IR700 administration.

6.2.2 OCT imaging system

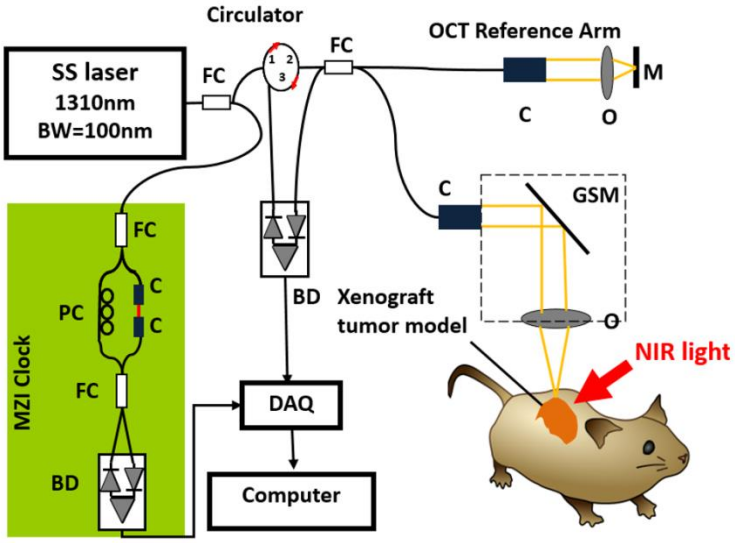

Fig. 6-1. Schematic of swept source OCT system.

SS laser: swept source laser. FC: fiber coupler. PC: polarization controller. BD: balanced detector. C: collimator. O: objective lens. GSM: galvo scanning lens. M: mirror.

One unique feature of OCT compared with conventional optical imaging modalities is its capability to resolve the information from different depths by using an interferometer. The interference fringe from different depths reveals the scattering intensity from the specific depth and has a characteristic oscillation frequency. By resolving signals with specific frequencies, a depth-resolved OCT image can be obtained. Fig. 6-1 shows the schematic of the swept-source OCT (SS-OCT) setup. The SS-OCT system[155-157] utilizes a wavelength-swept laser as its light source. Spectrum bandwidth of the laser is 100 nm centered at 1325 nm (Thorlabs, SL1325-P16), which gives 10 μm axial resolution in tissue. The wavelength-swept frequency is 16 kHz with 12 mW output power; therefore, for 1000 axial line images, the frame

rate is equivalent to 16 frames per second (8 frames/s if only one direction is used). A Mach-Zehnder interferometer (MZI) receives 3% of the laser output power and uses it to generate a clock signal with uniformly spaced optical frequency to trigger the sampling of the OCT signal in the analog-to-digital (A/D) converter. The circulator sends the photons from port 1 to port 2 and reflected light from port 2 to port 3. The sample and reference arms of a Michelson interferometer receive equal portions of the remaining 97% of the laser power. The galvanometer scanning mirrors deflect the sample arm light into the sample through an objective lens, which provides 15 μm lateral resolution. The backscattering light from the tissue is recombined with the reflected light from the reference mirror, and the interference fringe is detected by the dual-balanced detector. The signal will be acquired by the data acquisition card (DAQ) and then be sent to the computer for image construction and display.

6.2.3 Phantom studies

Fig. 6-2A-B shows the results of the phantom study. Two imaging protocols, DOCT [182] and SV [134] are tested with a vessel phantom. The vessel phantom is a capillary tube with 0.4 mm inner diameter. Intralipid solution (1% volume concentration) was pushed through the tube at various speeds controlled by an injection pump (Fisher Scientific, Single Syringe Pump). Fig. 6-2A shows that SV can accurately map the lumen of vessel, but DOCT reaches a detection limit at low velocities. SV is capable of mapping out the vessel lumen, even when the bulk flow speed is zero. On the other hand, Fig. 6-2B shows that DOCT changes linearly with the flow velocity, but SV doesn't vary with the flow velocity. Therefore we utilize

DOCT to measure the flow velocity and SV to measure vessel diameter. The standard deviation is calculated from 10 different images under a specific flow velocity.

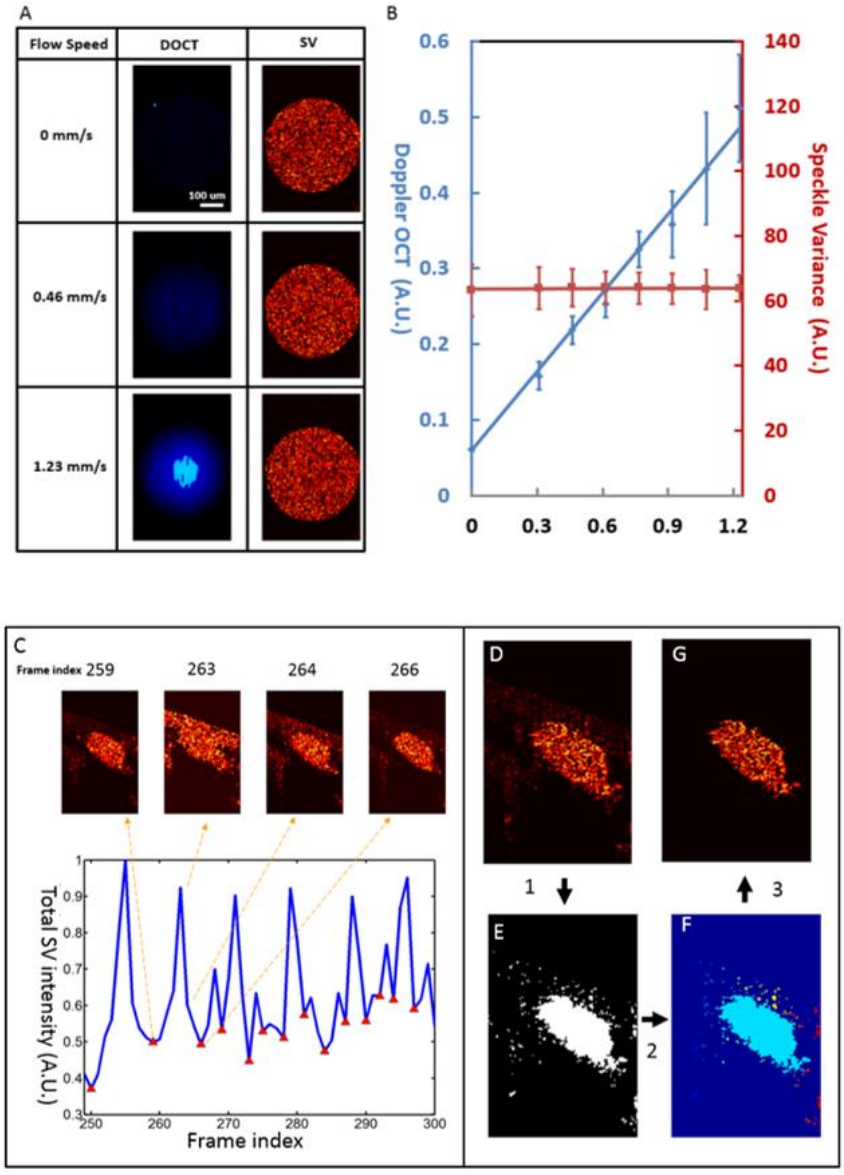

Fig. 6-2. Phantom studies and image algorithms

(A) Cross-sectional DOCT and SV images of a vessel phantom (0.4 mm inner diameter) at various flow velocity. (B) Total intensity of DOCT and SV versus flow velocity. (C) Real time motion detection using SV images (6 frames/s). Frame 259 and 266 shows the SV images when the tissue is at rest. Frame 263 and 264 shows the SV images when the tissue is moving. By locating the local minimum (indicated by the red triangles), we can isolate images with no motion. (D-G) Automatic ROI selection procedure. Fig. 6-2D is the original image with blood vessel and background noise. Fig. 6-2E is binary conversion of Fig. 6-2D. Fig. 6-2F is an image with all the connected pixels labeled with a specific color. Noise is dramatically reduced when choosing the ROI with the largest area. Fig. 6-2G is the final image without the background noise.

6.2.4 Bulk motion and ROI

During the in vivo experiment, tissue bulk motion can significantly degrade the image quality. For example, in Fig. 6-2C, when the tissue is moving (frame 263 & 264), the SV contrast between the tissue and vessel is poor. When the tissue is at rest (frame 259 & 266), the signal from the static tissue is reduced and the vessel is detectable. In Fig. 6-2C, we plot the total SV signal against the frame index. Since SV is decoupled with the blood velocity and only relates to the motion of scatters, the local maximum is not related to the pulsation but only reflects that the tissue is moving. Therefore, by searching the local minimum (marked by red triangles), we can easily distinguish images with good vessel/tissue contrast from those disturbed by bulk motion and eliminate those frames with motion degradation. DOCT images from frames with bulk motion are also removed from analysis.

In order to accurately measure the vessel lumen, we implemented an algorithm which isolates the vessel signal from the background noise. Fig. 6-2D-G demonstrates the procedure using representative images. In the first step, we convert the image to a binary image (Fig. 6-2E). In the second step, we used a MATLAB built-in function to label the connected components (Fig. 6-2F). Fig. 6-2F shows that the connected pixels are then labeled in one color. The color with the largest area is selected as the region of interest (ROI). In the final step, we overlay this ROI with the original image to isolate the vessel signal from the background (Fig. 6-2G). Since OCT cannot penetrate the entire diameter of large vessels, we cannot use the area of the cross section to represent the size. Thus, the length of the blood vessel along each

row is determined and the median measurement is chosen to represent the vessel size. Matlab code for ROI selection and bulk motion removal is attached in appendix B.

6.2.5 Statistical analysis

Data are expressed as mean + standard deviation. Statistical analyses were carried out using MATLAB. Student t test was used to compare vessel size and flow speed of treated tumors to the untreated control. $P < 0.05$ was considered to indicate a statistically significant difference.

6.2.6 Histopathologic evaluation

Excised tumors underwent histopathologic examination after formalin fixation and paraffin embedding. All samples were then serially sectioned at 40 μm intervals and stained with hematoxilin-eosin (H&E) or PECAM-1 (CD31, endothelial maker; company).

6.3 Results

Fig. 6-3A-D shows the diameter and the blood velocity of a PIT-treated tumor blood vessel. OCT provides the structure information. DOCT provides the blood velocity information and SV provides the size of the open lumen. The first 60 seconds, are obtained as a baseline before PIT. At 60 seconds, NIR irradiation(100J/cm^2) is turned on and blood velocity quickly drops below the detection limit. The open space in the vessel lumen also decreases with time, but remains open after 600 seconds of light irradiation. After 600 seconds, the NIR light is turned off and post-treatment data is obtained for another 60 seconds.

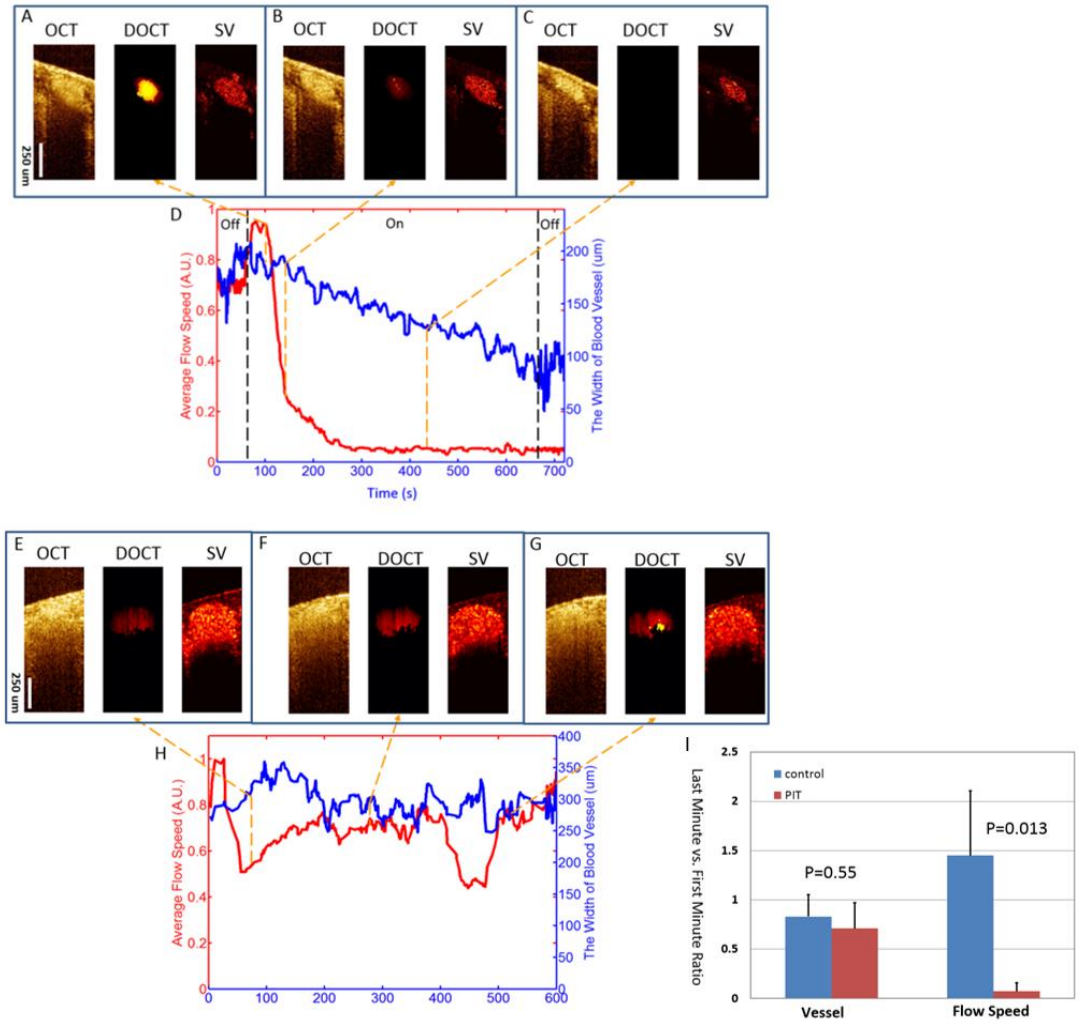

Fig. 6-3. Vascular changes in a PIT-treated and control tumor blood vessel.

(A-C) Representative OCT/DOCT/SV images at different time points (indicated by the orange dashed lines) during the PIT treatment. (D) Time plot of the blood velocity (red line) and the vessel width (blue line). In the first 60 seconds (indicated by the black dashed line), the laser light is off to obtain baseline information. After 60 seconds, NIR laser light is turned on for 10 minutes (60-660 seconds). The dosage is 100 J/cm^2. In the last 60 seconds (660-720 seconds), the light is turned off to obtain post-treatment information (indicated by the second black dashed line on the right). (E-G) Representative OCT/DOCT/SV images at different time points (indicated by the orange dashed lines) of a control tumor blood vessel (with NIR light, but no PIT drug) (H) Time plot of the blood velocity (red line) and the blood vessel width (blue line) of the control vessel. The dosage is 100 J/cm^2. (I) Ratio of vessel size and blood velocity in PIT-treated and control tumors (control is NIR irradiation but no PIT drug). The vessel size of PIT-treated vessels (n=4, from 3 mice) is slightly smaller than its size in the first minute, but it is not statistically significant (P>0.05) compared to the control (n=5, 3 mice). On the other hand, the blood velocity of PIT-treated blood vessels drops significantly in the end of treatment compared to the beginning and it is statistically different from the control (P<0.05).

The vessel size and the velocity remain at a relatively constant level after irradiation. At the beginning of irradiation, the DOCT image (Fig. 6-3A) demonstrates that blood velocity is high and the SV image shows a large lumen.

After 83 seconds of irradiation, the DOCT image (Fig. 6-3B) shows that the velocity has significantly decreased, but the size of the lumen remains almost unchanged. The blood velocity drops below the detection limit after 372 seconds of irradiation, but the lumen remains open (Fig. 6-3C).

Control experiments were performed on rats that did not receive the antibody-photosensitizer conjugate but underwent light exposure. Fig. 6-3E-H shows that blood velocity and lumen size during the 600 seconds of NIR irradiation fluctuate moderately, which is probably due to physiologic variation and motion, but there is no sustained blood velocity drop in the controls. Indeed, the images show that the blood velocity and the lumen size remains essentially the same throughout the measurement period.

To quantify the effect of PIT, the ratio of blood velocity and lumen size at the beginning and end of PIT (comparing the first and last minute during irradiation) was determined (Fig. 6-3I). PIT-treated group consisted of 4 tumor vessels from 3 different animals. Control experiments (with irradiation but no drug) were performed on 5 tumor vessels from 3 different animals. The lumen size of PIT-treated tumor vessels decreased with time (ratio is smaller than 1) but it is not statistically different from the control vessels (T test, $P>0.05$). On the other hand, the drop in blood velocity in PIT-treated blood vessels was statistically different compared with the control group ($P<0.05$). We conclude that while there are small non-significant

changes in vessel lumen diameter, there is a measurable acute decrease (more than one order of magnitude) in blood velocity in PIT-treated vessels.

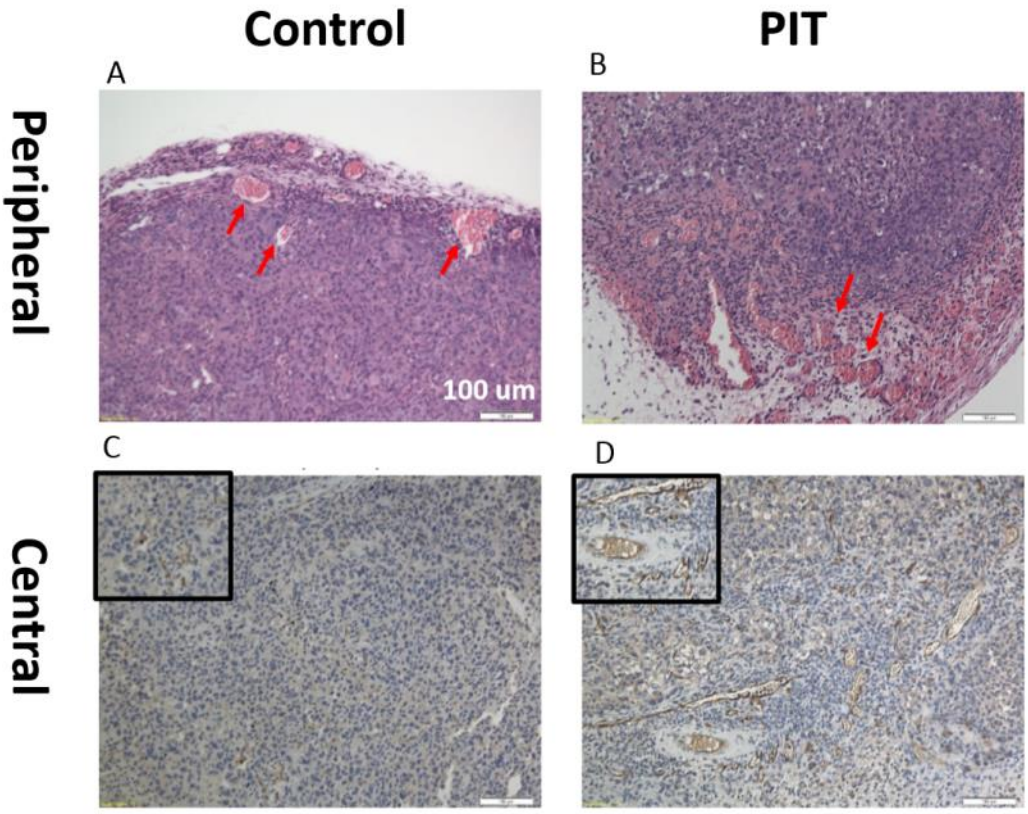

Fig. 6-4. Histology of the control and PIT treated tumor vessels.

(A) Histology (H&E staining) of control peripheral tumor vessel. Intact blood vessels are indicated by the red arrows. (B) Histology (H&E staining) of PIT-treated peripheral tumor vessel. Intact blood vessels are indicated by the red arrows. (C) Histology (PECAM1 staining) of control central tumor vessel. The inset shows a zoom-in image. (D) Histology (PECAM1 staining) of PIT-treated central tumor vessel. The inset shows a zoom-in image. The scale bar represents 100 μm.

Fig. 6-4A-B demonstrates the histology of peripheral tumor blood vessels. With H&E staining, the red blood cells do not display a nucleus and can be found in the well-preserved blood vessels (indicated by the red arrows). The vessels in both control and PIT-treated tumor have well defined boundaries and are easily identifiable indicating that the vessels are not destroyed by PIT. This data is

consistent with the in vivo result, which suggests blood vessels are not damaged. On the other hand, PECAM-1 staining (Fig. 6-4C-D), which labels the endothelial cells of blood vessels (brown color), demonstrates that the PIT-treated capillaries in the deep tumor bed are markedly dilated compared with the control vessels.

6.4 Discussion

There are several advantages of using OCT in this setting. It allows us to monitor tumor vascular responses without the injection of a contrast agent or the implementation of an artificial tumor window chamber. Motion gating with speckle variance successfully overcomes the challenge of bulk motion artifact and permits in situ imaging without interfering with the tumor. This method requires fast imaging speed to obtain images not degraded by bulk motion from a breath cycle. Since the normal mouse respiratory rate is around 3 breaths per second, according to the Nyquist sampling theory, imaging speeds >6 frames/s are necessary to record the entire cycle. High imaging frame rate limits the number of A-lines per image (more A-lines per image, slower frame rate) and thus limits the field of view. We used 1000 A-lines per image within a 715 μm field of view (FOV) to achieve reasonable DOCT sensitivity. FOV could be increased by two orders to 71.5 mm while maintaining the same frame rate by using a laser source with two-orders faster wavelength sweep rate [183]. In addition, high-speed lasers can potentially enable 4D tissue images. Besides FOV, the spatial resolution could be further improved to observe the small vessel dilation. Micro-OCT [184] with a resolution of 1 μm in three dimensions will enable the detection of small vessel dilation in vivo.

Unlike in most other ablative therapies, both in vivo SV imaging (Fig. 6-3A-C) and histology images (Fig. 6-4B) verify that the peripheral tumor blood vessels remain intact during PIT treatment. Furthermore, speckle variance confirms that the vessels are filled with free moving blood cells and are not thrombosed. An obstructed vessel would result in the absence of free moving scatters and the vessel would lose its variance contrast relative to static tissue, none of which was observed. The vessels are open and filled with free moving blood cells. However, the central and peripheral vessels respond very differently. Due to the limitation of spatial resolution and penetration depth, only big (>100 μm) peripheral tumor vessels are observed in vivo with OCT. These big peripheral vessels do not dilate (Fig. 6-3I), while the deep capillaries are markedly dilated (Fig. 6-4D). This heterogeneous response may be due to the difference in vessel structure. The thick peripheral vessels typically have full structures including muscular bundle in the wall, which make them less likely to change during PIT.

Fig. 6-3A-D demonstrates that the blood velocity in peripheral tumor blood vessels drops significantly during PIT treatment, while the lumens of the vessels remain open. Blood velocity is maintained in control animals who received the conjugate but no light irradiation (Fig. 6-3D, 0-60 seconds) and the controls who received light irradiation but no conjugate (Fig. 6-3H). This blood velocity drop may be due to the increase of blood pool volume as a consequence of dilated central vessels. A much larger central blood pool volume as well as possible decreased intravascular pressure in the peripheral vessels could slow the blood to the periphery.

In conclusion, PIT treatment acutely reduces blood speed while the blood vessel are undamaged or thrombosed. Slow blood flow speed implies long drug circulation time. On the other hand, dilated central vessels may lead to slow periphery flow and increase in drug pool volume in tumor vessels.

In our next project, we will use multiphoton microscopy to observe the diffusion of the antibody-IR700 conjugate and estimate cancer cell viability in situ. This study will help elucidate how PIT destroys the perivascular barrier and enhances the delivery of anticancer drugs.

Chapter 7: Conclusion and future direction

7.1 Optical coherence tomography for neurosurgery

Intra-operative neurosurgery guidance has seen significant advancements since the introduction of micro electrode recording (MER) and intra-operative MRI (iMRI). Despite the great guidance capabilities of these technologies, the fundamental limitations of MER and iMRI leave lots of room for improvement. MER is an accurate tool for locating brain nuclei by observing the distinctive neuron firing patterns, but it also increases the risk of disastrous intracranial hemorrhage, requires long operation hours, and is not capable of targeting white matter tracks. iMRI, in contrast, is capable of locating different tissues (lesions, nuclei and white matter tracks) and avoiding hemorrhage. However, iMRI imaging suffers from low spatial resolution (1 mm), slow imaging speed (tens of minutes) and high cost. Therefore, iMRI is mostly used as a pre-/post-operative imaging tool and intra-operative guidance tools such as MER are still necessary during the surgery.

Optical coherence tomography is a promising real-time guidance tool, because it is capable of imaging brain nuclei [40], lesion [185], fiber tracks [42] and brain blood vessels [41] simultaneously in real time. Dr. Tang's group is the first to demonstrate that OCT can detect important tissue landmarks for neurosurgery guidance [40]. Moreover, they also demonstrated that a side-viewing OCT probe can guide the injection of therapeutic agents to deep brain targets *in vivo* in small rodents [43].

7.1.1 OCT needle probe

By collaborating with Dr. Tang's group, we developed the next generation of OCT probes for neurosurgery guidance[41] (chapter 3). Two fundamental improvements make this probe another step closer to clinical use: forwarding imaging and Doppler flow tomography. Forwarding imaging capability that enables the detection of blood vessels in front of the advancing probe is crucial for avoiding hemorrhage. There are various forward-imaging OCT probes which have been developed before this work, but they are too bulky to be integrated into neurosurgical tools. We overcame this challenge by relocating the actuator for laser scanning from the distal to proximal end and relaying the laser spot into the tissue through a static GRIN rod lens. This approach not only solves the size issue but also significantly improves the phase stability which results in high quality Doppler tomography. To the best of our knowledge, this is the first forward-imaging probe that can perform OCT and Doppler OCT simultaneously. Please see technique details in chapter 3.

Currently, the major roadblock of the clinical translation of this device is that the sensitivity is not comparable to MER. OCT contrast between the small nuclei targets and their surrounding tissues is not high enough. Polarization-sensitive OCT (PSOCT) can potentially solve this problem by providing additional birefringence contrast. In literature, six fold improvement of contrast has been reported[42]. Moreover, PSOCT enables us to measure the orientation of fiber tracks, which in combination with full brain micro-tractography[186] will further improve the accuracy of targeting . The tractography shows that the neural fibers at different location have different

orientation. Therefore if we can color code the fiber tracks in our full-track measurement , we will be able to better localize the probe.

System wise, the device needs to be further minimized (Fig. 7-1) for the integration with a stereotactic frame. A needle guidance that could be hand-held by the surgeon is important for some applications. In the future, we can use microelectromechanical (MEMS) mirrors (Mirrorcle) to replace the bulky scanning mirrors, a high precision ferrule (Vitrocom) to replace the alignment stage and a small GRIN lens to replace the objective lens. Previously, we relied on an alignment stage to achieve oblique illumination to reduce the strong reflection from the proximal end surface of the GRIN needle, which significantly degrades the imaging quality. In the new design, we can process the end surface with an anti-reflection coating and angle-cutting to solve this issue[151]. The GRIN rod lens that relays the scanning laser spot and collimates the laser beam is generally considered as polarization isotropic component and the PM fiber design allows us to actuate the sample arm without affecting the power distribution between two polarization channels. With these design changes, we can build a needle-type, forward-imaging and hand-held PSOCT probe.

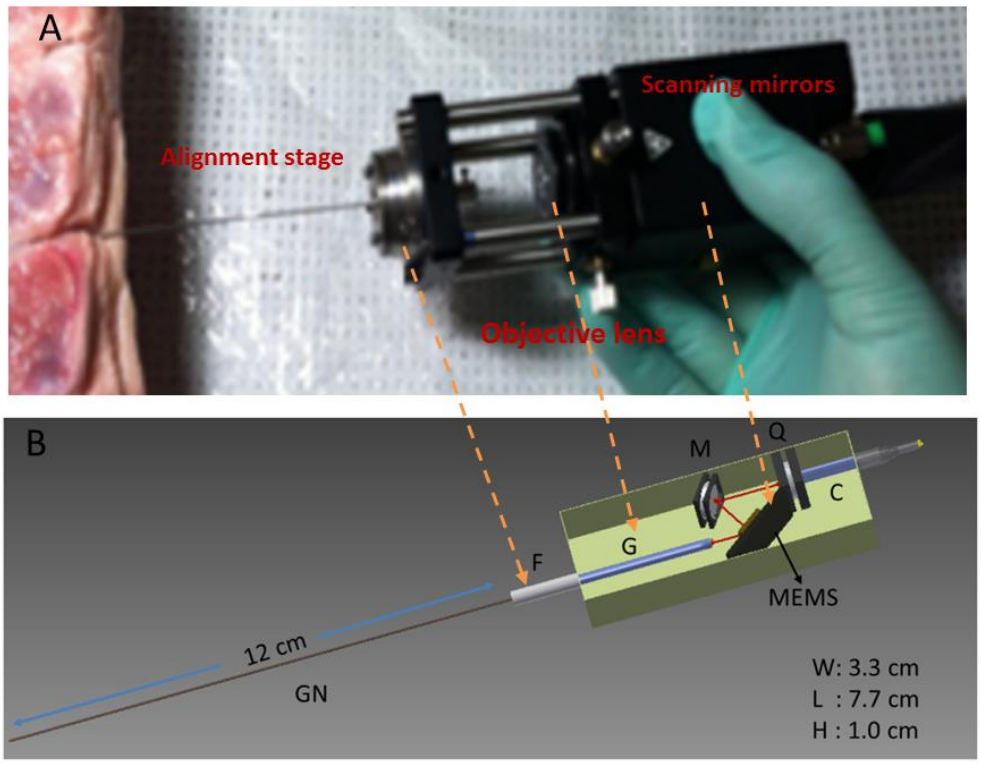

Fig. 7-1. Miniaturization of OCT needle probe

(A) Current OCT needle probe. (B) Schematic of miniaturized PSOCT probe. The collimator, C, will collimate the laser beam. After passing through quarter waveplate, Q, and being reflected by the mirror, M, the laser beam will be projected on MEMS mirror, which will deflect the laser beam to the proximal end of GRIN rod lens, G, and scan the laser beam to perform 2D or 3D imaging. A high precision ferrule will align the focused spot from G to the GRIN needle, GN. Then, GN will relay the scanning laser spot into tissue.

Besides neurosurgery, the OCT needle probe can be applied to other needle-based procedures requiring high-resolution visual feedback. For example, regional anesthesia, including neuroaxial and peripheral blocks, are traditionally performed using blind, landmark based approach. Together, they account for 6 million procedures annually in the US. Due to lack of visual feedback to guide needle navigation, failure rate of epidural anesthesia is up to 20% [171], and the complication rate of peripheral nerve block approaches 10%, with the real potential for permanent nerve damage [187]. Ultrasound and ionizing fluoroscopy are the two major imaging modalities being used to monitor the needle insertion. However, for

neuroaxial blocks, ultrasound guidance is especially challenging because of the complex, articulated encasement of bones that allows only a very narrow acoustic window for the ultrasound beam [171]. Fluoroscopy, on the other hand, has no soft tissue contrast, and therefore cannot identify blood vessels and nerves which are important to locate/avoid while inserting the anesthesia needle.

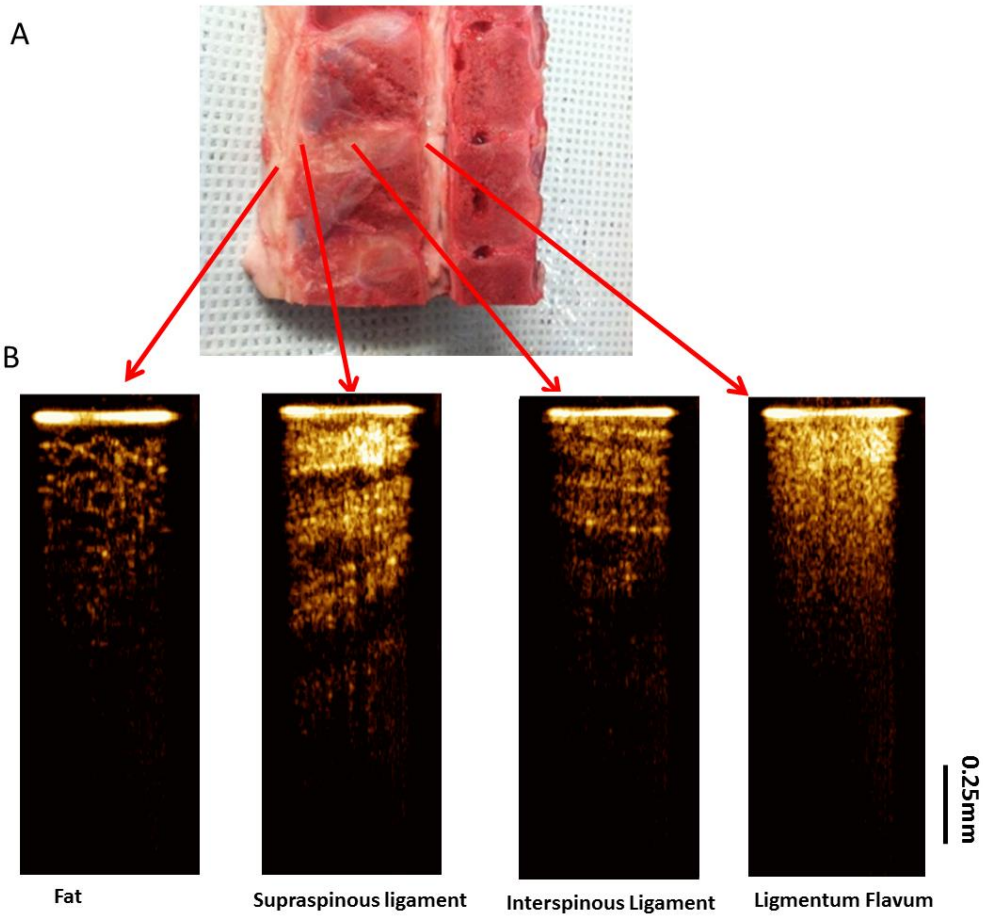

Fig. 7-2. OCT needle probe for regional anethesia

(A) Picture of a spine tissue cut along the sagittal plane. (B) Tip-front OCT images of fat, supraspinous ligament, interspinous ligament and flavum.

Fig. 7-2 demonstrates the potential of using OCT needle probe for epidural anesthesia. Fat tissue is featured with pockets of adipocytes. Ligaments are featured with bright and dark stripes due to birefringence effects. The supraspinous and interspinous ligaments can be differentiated by their fiber orientation and the

thickness of fiber bundles. Flavum has bright (hyper-reflective) and homogenous scattering intensity. These soft tissue images can assist anesthesiologist to locate the position of needle.

7.1.2 MRI/OCT

Although OCT imaging devices provide useful visual feedback, its field of view (FOV) is limited (1-2 mm) due to tissue scattering. Therefore, many efforts have been made to combine OCT with volumetric imaging modalities, such as ultrasound [188]. However, combing OCT with MRI, one of the most powerful tool for neurosurgery, had not been done before this work [168] (chapter 4). There are two main technical challenges: (1) To create an MRI-compatible OCT imaging system without electrical motors or wires close to the region of interest and (2) To move or insert the probe inside the constrictive MRI bore.

We solve these issues by incorporating a piezoelectric based OCT imaging system with an MRI compatible robot (from Dr. Jay Desai's group [166]). The *ex vivo* human brain imaging demonstrates that OCT is a great complimentary technology to iMRI guidance. MRI/OCT multi-scale imaging achieves unprecedented 20 μm resolution, which improves the accuracy of conventional MRI imaging (~ 1mm) by two orders. More importantly, OCT provides real-time (15 frames/s) structural information between the gap of high-resolution MRI images (exposure time is over 15 minutes). In addition to the accuracy improvement, OCT provides a different contrast based on optical scattering which enables the detection of MRI-occult tissue landmarks.

The barriers for *in vivo* imaging includes: 1) lack of degrees of freedom and 2) OCT imaging distortion. The first issue can be solved by integrating the OCT system with an MRI robot with multiple degrees of freedom (a novel robot system developed by Dr. Jaydev Desai's group) [189]. The second issue occurs because the flexible fiber is actuated at a distal site. Non-uniform scanning can be corrected by speckle correlation [170], which measures the distance between adjacent A-lines by studying the correlation of intrinsic speckle patterns. Moreover, it is possible to incorporate Doppler OCT imaging with an advanced correction algorithm [190].

With the improved degrees of freedom and imaging quality, we can perform an *in vivo* study to test the system performance under the influence of physiological motion (breathing, etc.) and biofouling (bleeding, etc.).

7.1.3 Coherence gated Doppler

In some medical conditions, it is not necessary to obtain visual feedback and accept the tradeoffs associated with imaging, such as bulky device size (~ 1mm) or mechanical vibration noise from the actuator. For microelectrode recording (MER), for example, what is needed is a miniature sensor that can be easily integrated with the MER electrode and detect the at-risk blood vessels in front. Previously, laser Doppler (LD) probe has been used to monitor blood perfusion in human brain *in vivo* [123]. However, diffuse optics probe design of LD provides poor spatial specificity (mm-cm) and makes it difficult to be used for avoiding blood vessels.

Coherence-gated Doppler (CGD) is a novel design, which is constructed by converting time domain OCT imaging system to a sensing system [137] (chapter 5). CGD has two unique features specifically designed for avoiding intracranial

hemorrhage: 1) CGD has a much better lateral spatial resolution (< 100 μm) than LD (mm-cm) and 2) CGD has much longer axial detection range (mm) than OCT (10 μm). These properties enable CGD to pick up the signal from the blood vessels few mm ahead without mixing it with the signal from surrounding vessels.

The biggest challenge we currently face with CGD is motion artifacts. While the probe is inside highly scattering tissues, probe movements associated with surgical procedures will create a strong Doppler signal. This issue can be alleviated by moving the probe slowly. However, this is not practical in some cases. Another method to solve this issue is calculating cross-correlation between adjacent signal segments in time. The motion signal is fragmented and inhomogeneous in the frequency domain (chapter 5, Fig. 7-6) and thus has low cross correlation between signal segments. In contrast, the vessel signals are consistent and homogeneous in frequency domain and therefore adjacent signal segments are highly correlated. Therefore, calculating the signal cross-correlation between adjacent time segments should allow us to extract the vessel signal from the motion background. One tradeoff of this approach is that we need to reduce the temporal resolution to collect enough data for calculating the cross correlation. In the future, we should also perform more *in vivo* studies to determine the criteria of hazardous blood vessels, which should be avoided to reduce the risk of symptomatic hemorrhage.

Besides avoiding vessels, CGD or LD can also be used to target vessels. Over 6 million central venous and 8 million arterial catheters are placed each year [191]. Due to lack of feedback, failure rates are often high, requiring multiple needle insertions for successful cannulation. Depending on the anatomic site and operator

experience, up to 33% of needle-based interventions are associated with complications, of which some are fatal [192]. The likelihood of complication is also related to the number of failed attempts. Compared to successful ocannulation after the first attempt, the incidence of mechanical complications after 3 attempts or more are six fold higher [192]. Such mechanical complications include bleeding, hematoma, pneumothorax, and vascular injury.

Fig. 7-3 demonstrates the potential of using OCT/LD probe for targeting blood vessels. LD can detect blood flow beyond the OCT field of view (up to 5 mm) and provide audio feedback. When the probe is close to the blood vessel (within 1mm range), OCT is capable of providing Doppler imaging to confirm whether the probe has contacted or punctured the vessel. The first column of Fig. 7-3B depicts a cartoon and OCT/LD feedback when the blood vessel is out of range of the OCT imaging. The OCT image has relatively long penetration depth associated with muscle tissue and the DOCT detects no flow. However, the LD is more sensitive and can detect clear pulses. By following the audio feedback from LD system, we will approach the blood vessel. The second column depicts OCT/LD feedback when the probe is contacting the vessel. OCT is capable of differentiating the vessel wall (indicated by the red arrow) and DOCT can detect a flow signal beyond the vessel wall. Shallow penetration depth is observed for the OCT images when the probe is contacting the blood vessel. The last column depicts OCT/LD feedback when the probe has punctured the blood vessel and the vessel wall is no longer visible with OCT and the flow signal is much stronger in the DOCT image.

When an interventional radiologist, cardiologist, neurosurgeon, etc advances a catheter in the vascular system he doesn't really know if the tip is in the middle of the lumen of the vessel or pushing against the side of vessel that has a kink in it. He is forced to inject contrast dye and expose the patient and him to extra x-rays. There is increasing attention to how much radiation the patient and the physician are allowed to receive. Furthermore, the amount of contrast agent given to the patient is proportional to the risk of inducing renal failure, a serious concern and frequent complication.

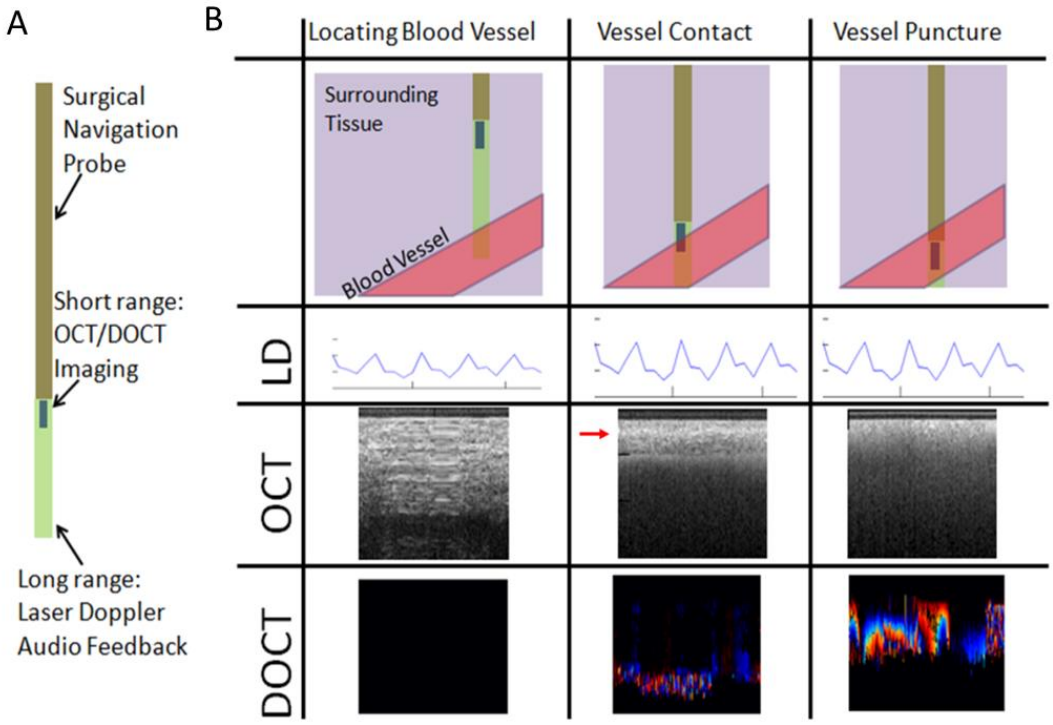

Fig. 7-3. OCT/LD probe for targeting blood vessels

(A) A cartoon depicting the relative penetration depth of OCT and LD. LD can detect blood flow beyond the OCT field of view (up to 5 mm) and provide audio feedback. (B) A table demonstrating the feedback observed from the OCT/LD probe during surgical navigation towards a blood vessel.

CGD can minimize this problem if it can provide continuous feedback on whether the tip is surrounded by blood or is pushed into the vessel wall. We predict the two

will sound different. Our ears are very good at telling subtle changes in sound. It is also much easier to multitask with visual and audio information simultaneously. The audio signal will not distract the radiologist who is looking at the monitor.

Another potential application of CGD will be pulp vitality measurements. The current standard of care in pulpal diagnosis is based on sensibility of pulpal nerves to thermal and electrical stimuli. Studies have shown that these techniques are frequently inaccurate in diagnosing the pulpal vitality, because they rely on neural rather than vascular information. While studies are available that show relatively high sensitivity and specificity for these techniques [193, 194], these studies share a significant limitation in that the gold standard was determined after treatment, and thus many cases that likely needed treatment but were never treated were not included. In addition, the utility of traditional thermal and electrical pulp testing methods in traumatic cases is very much diminished, because it is well known that following trauma, pulpal nerves do not respond to testing for a few weeks or months, but regain responsiveness with time. To address these limitations, techniques using laser Doppler flowmetry [195, 196], infrared [197] and pulse oximetry [198, 199] have been introduced to accurately determine pulpal vitality. The major limitations of these methods have been the inability to limit detection of blood flow to the tooth (and not the gingival or periodontal tissues), the need to immobilize the patient's head in relation to the probe by creating a customized stabilizing jig for each patient, the interference caused by enamel cracks or dental restorations and the reduction in size of the pulp space with age or following a traumatic injury. Therefore, these technologies have not resulted in any commercially available instruments on the

market today that would truly measure pulpal vitality. CGD has much confined sample volume that could reduce the noise from the surrounding gum tissues and should significantly improve the specificity.

CGD can also be applied to non-vascular interventions: Detect changes in tissue at the probe tip as one pushes it forward (i.e. needle) into tissue. Examples include:

Percutaneous catheterization of the biliary tree. Here the GI doctor inserts a needle blindly between the ribs and aims for the base of the liver where the bile ducts emerge. The goal is to place a thin cannula into the bile duct that is blocked for some reason (i.e. stone, cancer, or stricture). This is a particularly important procedure for Chinese in China, since liver disease is one of the most common if that the biggest killers in China. My former student who is now a resident in interventional radiology at UCSF is considering using OCT as guidance for this procedure. But I think it would be so much easier to listen for changes in the sound when the tip is in solid tissue vs inside the lumen of the bile duct with bile. We can also add a spectroscopy feedback fiber to detect the difference between blood (liver) and bile (duct).

Spinal tap and epidurals. Here the CGD can be used in two ways. Currently, epidurals are carried out by the "loss of resistance" method where the anesthesiologist applies a gentle pressure on a syringe attached to the advancing needle. When the tip of the needle enters the epidural space the syringe pressure drops. The loss of resistance methods requires two hands and that the patient is motionless. We can build a unit consisting of a disposable pressurized syringe with an optical fiber embedded in the stylet that can detect flow at the tip of the needle. This would be far more sensitive than the human hand and it would require only one (not two) hand to

operate.For the spinal tap there will be no need to use the pressurized system. The fiber sensor will simply detect changes in movement within solid tissue to movement within fluid (CSF). OCT is too much technology for a relatively simple procedure. Coherence gated Doppler is orders of magnitude simpler and cheaper and therefore more feasible.

7.2 Optical coherence tomography for cancer research

Optical coherence tomography, which can provide tissue microstructure, Doppler flow imaging and speckle variance angiography simultaneously in real time without any contrast agent is a powerful tool for preclinical animal study. In chapter 6, an OCT imaging platform with novel imaging algorithms for monitoring tumor microenvironment during PIT treatment is presented. By using speckle variance to remove the motion artifact, we can perform intra-vital OCT imaging on *in vivo* animals without an artificial window chamber, which may significantly affect the physiology of tumors. Observations of the hemodynamic changes provides with a better understanding of the therapeutic mechanism of this new anti-cancer therapy.

In the future, we plan to integrate fluorescence molecular imaging (FMI) with the needle device to study the variation of the permeability of tumor blood vessels during photo-immunotherapy (PIT). We will inject a fluorescence contrast agent through the tail vein and quantify how much fluoresce molecular is leaked into tumor bed. Fig. 7-4 shows the schematic of the multi-model imaging needle system. The left side of Fig. 7-4 is a SS-OCT system. In the sample arm, the GRIN lens will relay the laser spot into the tissue and collect the back scattered light. The fluorescence molecular imaging (FMI) subsystem is combined with the OCT sample arm using a dichroic

mirror. The fluorescence excitation and emission light (yellow line, wavelength < 800 nm) will be reflected by the dichroic mirror, while the long wavelength OCT light (red line, 1300 nm) will penetrate through the mirror. Two imaging modalities will be carefully co-registered. The emission fluorescence signal will be reflected by another dichroic mirror. Then, it will pass through an emission filter and finally reach the photomultiplier tube (PMT). The wavelength of the excitation laser, emission filter and dichroic mirror are chosen based on the excitation and emission properties of the selected fluorophores. This system can be readily adapted to image fluorophores with different excitation/emission wavelengths in the range of 400 – 800 nm.

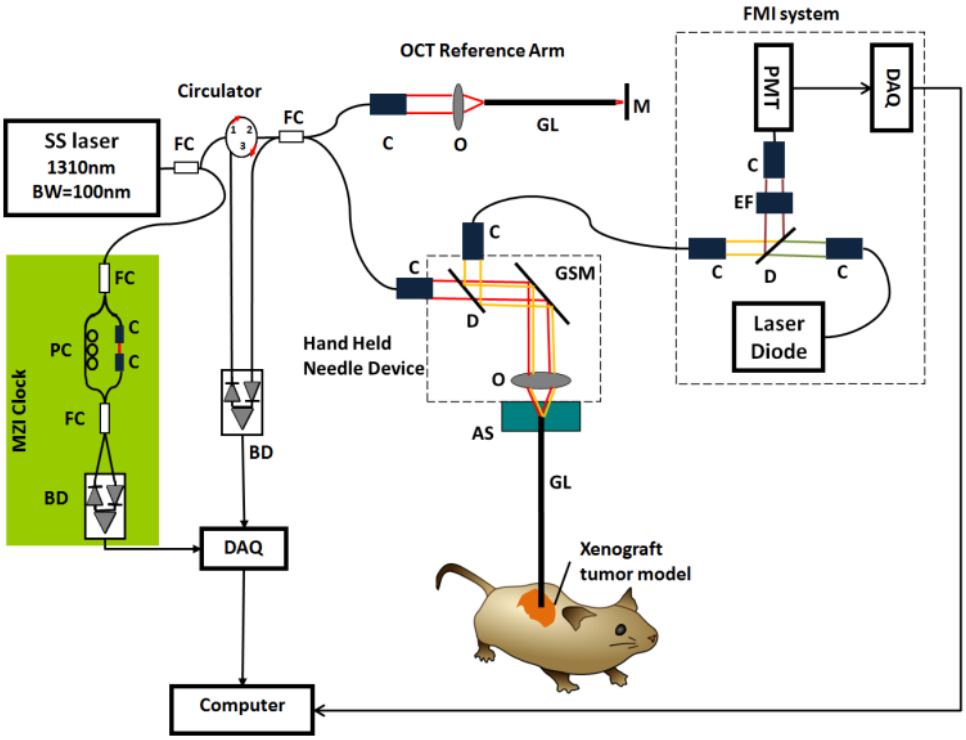

Fig. 7-4. Schematic of OCT/FMI imaging needle.

FC: fiber coupler; PC: polarization controller; C: collimator, BD: balanced detector, MZI: Mach-Zehnder interferometer (frequency clocks), DAQ: data acquisition board, M: mirror, GSM: galvo scanning mirror, O: objective lens, AS: alignment stages, GL: GRIN lens needle, D: dichroic mirror, EF: fluorescence emission filter.

7.3 Contributions

Here are the itemized personal contributions that advance the field of biomedical imaging and sensing:

- Developed one of the thinnest (O.D. 0.74 mm) forward-imaging needle-type Doppler OCT probe and demonstrated that the needle can target or avoid specific tissues in large animals *in vivo*. The novel design that replaces the distal actuation with proximal actuation and a relay GRIN lens significantly reduces the needle size (from > 2mm to 0.74 mm) and enables the applications requiring minimal tissue damaging, such as neurosurgery and spine surgery. Furthermore, real time (8 frames/s with Doppler OCT) imaging speed, micrometer resolution (~ 10 μm) and great soft tissue contrast (blood vessels, gray matter, white matter, ligament and nerve bundle) makes this system a promising platform technology for needle-based procedures.

- Designed and constructed the first MRI compatible OCT imaging system that improves the accuracy of MRI-guided procedure by two orders to ~ 20 micrometer and provides an optical contrast that enhances the detection of MRI-occult tissue landmarks. Furthermore, concurrent and multi-scale MRI/OCT imaging could be used to correlate the functional MRI (fMRI) signal with high resolution optical signal to study the neural origins of fMRI signal.

- Developed a cost-effective optical sensing system, coherence gated Doppler (CGD) to replace Doppler OCT in certain medical settings (reduced the system cost from $30,000 to $3,000). CGD probe has wider speed detection range (from mm/s to m/s) than phase sensitive Doppler OCT (< 1 mm/s) and provides better spatial resolution (< 100 μm) than Laser Doppler (mm-cm).

- Investigated the super enhanced permeability and retention (SUPR) effect induced by photoimmunotherapy. Developed advanced imaging algorithms for tracking and quantifying the rapid hemodynamic changes during the therapy in tumor-bearing mice *in vivo*. Successfully extracted important physiological parameters that lead to better understanding of the mechanism of SUPR effect.

Appendix A

Matlab Code for phase-sensitive Doppler OCT

```
function
[OCT_Display_Complete,dPhase_Complete,dVelocity_Complete,dVariance_Complete]=DOCT_FRG_
Read_3D(Filename,frame_start,frame_stop)

%%%%%%%%%%%%%%%%%%%%  Chia-Pin Liang  %%%%%%%%%%%%%%%%%%%%

%%%%%%%%%%%%%%%%%%%%%%%
%Frames to read
if nargin < 2
    frame_start =1;            %Start Frame for DOCT processing (must be <= to
"frame_stop")
    frame_stop ='all';           %End Frame for DOCT processing (integer value > 0 or
'all' for total frames, default=199)
end

%%%%%%%%%%%%%%%%%%%%%%%
%Parameters for applying window function to fringe data (fringe_apodization)
Contrast = 1.0;
Brightness = 0;
Scan = 'F';         % which scan will be processed: 'F' for Forward, 'R' for backward,
'B' for both
apodiz_method =  'Gaussian';  % 'Cosine', 'Gaussian',
'Super_Gaussian','Hann','Hamming','Blackman', 'Nuttall', 'Blackman_Harris'*,'none'

%%%%%%%%%%%%%%%%%%%%%%%
%Parameters for phase-resolved Doppler OCT
BulkMotionRemoval = 'H';    % 'H'-- histogram method; 'C'--- complex vector method,
'N'--- none

%Phase-resolved method or called autocorrelaton method
dThreshold_Intensity = 40;          % OCT intensity threshold for Doppler image
dThreshold_Variance = 0.1;         % OCT variance threshold for suppression of noise
start_ref = 120;                     % start data point in every A line for bulk
motion removal
end_ref = 350;                      % end data point in every A line for bulk motion
removal
ref_points = end_ref-start_ref;     % data points for complex vector method of bulk
motion removal
bin_size = 128;                     % bin size used in histogram removal method
shift_depth = 1;                    % step size in depth for sliding average window
shift_width = 1;                    % step size in width for sliding average window
OCT_ave_depth = 1;                  % window length in depth for OCT sliding average
window
OCT_ave_width = 1;                  % window length in width for OCT sliding average
window
DOCT_ave_depth = 5;                 % window length in depth for DOCT sliding average
window
DOCT_ave_width = 5;                 % window length in width for DOCT sliding average
window
%%%OCT window size must be <= DOCT window size!%%%

%%%%%%%%%%%%%%%%%%%%%%%%%%%%%%%%%%%%%%%%%%%%%%%%%%%%%%%%%%%%%%%%%%%%%%%%%%%%%%%%
%%%%%%%%%%%%%%%%%%%%%%%%%%%%%%%%%%%%%%%%%%%%%%%%%%%%%%%%%%%%%%%%%%%%%%%%%%%%%%%%
%Get OCT (.FRG) file name if there is no input argument
if nargin < 1
    msg1 = msgbox('Select OCT FRG Data File','Select File');
    uiwait(msg1);
    pause(0.1);

    %Get file name and file path of the fringe data
    [filename, pathname] = uigetfile( ...
       {'*.FRG','OCT FRG File (*.FRG)';'*.*', 'All Files (*.*)'}, ...
        'Select OCT FRG File','MultiSelect','off');
```

```
    if pathname == 0
        return
    end
    Filename = fullfile(pathname,filename);
end

%Read OCT fringe data from selected (.FRG) file
[OCT_Fringe_3D, image_depth, nFr, frame_start, frame_stop] =
Load_Thorlabs_DOCT_FRG_3D(Filename,frame_start, frame_stop);
[FFT_length, image_width, Num_frame] = size(OCT_Fringe_3D);

%Analyze OCT fringe data
count=1;
for frm_n = 1:Num_frame    %DOCT frames are doubled so only process every other one
    %Display current Doppler frame number
    index = frame_start + frm_n -1;
    disp('%%%%%%%%%%%%%%%%%%%%%%%%%%%%%%%%%%%%')
    disp(sprintf('Processing Frame: %d',index))

    %Determine which scan to process ['F' for forward,'R' for backward,or 'B' for both]
    if strcmpi(Scan,'F')
        k_Fringe = OCT_Fringe_3D(:, 1:2:image_width, frm_n);
    elseif strcmpi(Scan,'R')
        k_Fringe = OCT_Fringe_3D(:, 2:2:image_width, frm_n);
    elseif strcmpi(Scan,'B')
        k_Fringe = OCT_Fringe_3D(:, :, frm_n);
    end

    %---------------------------------------------------------
    %Apply apodization to k domain spectral fringes using specified window function
    k_Fringe = Fringe_apodization(k_Fringe, apodiz_method);

    %Compute complex OCT fringes from k domain spectral fringes
    OCT_complex = Compute_Analytical(k_Fringe, FFT_length, image_depth);

    %Calculate average OCT signal, doppler phase shift, variance, and phase images
    [OCT_Intensity dPhase dVariance] =
Phase_Resolve_DOCT(OCT_complex,BulkMotionRemoval,dThreshold_Intensity,...

dThreshold_Variance,start_ref,end_ref,ref_points,bin_size,shift_depth,shift_width,OCT_
ave_depth,OCT_ave_width,...
        DOCT_ave_depth,DOCT_ave_width);

    %Convert OCT intensity image to dB scale and rescale to [0, 255]
    OCT_Display = OCT_mapping(OCT_Intensity, Contrast, Brightness);

    %---------------------------------------------------------
    %Zero pad the end to restore original image dimensions from the averaging window
%     OCT_Display=[[OCT_Display zeros(size(OCT_Display,1),DOCT_ave_width+1)];
zeros(DOCT_ave_depth,size(OCT_Display,2)+DOCT_ave_width+1)];
%     dPhase=[[dPhase zeros(size(dPhase,1),DOCT_ave_width+1)];
zeros(DOCT_ave_depth,size(dPhase,2)+DOCT_ave_width+1)];

    %---------------------------------------------------------
    %Plot images
%     figure; imagesc(OCT_Display); colormap(gray(256)); colorbar; axis image;
%     figure; imagesc(dPhase); colormap(DOCT_Colormap(256)); colorbar; axis image;
caxis([-pi pi]);

    %---------------------------------------------------------
    %Pre-allocate variables
    if frm_n == 1
        OCT_Display_Complete=zeros([size(OCT_Display) frame_stop-frame_start+1]) ;
%OCT intensity image
        dPhase_Complete=zeros([size(dPhase) frame_stop-frame_start+1]) ;
%Doppler OCT phase image
        dVariance_Complete=zeros([size(dVariance) frame_stop-frame_start+1]);
%Doppler variance image
    end

    %---------------------------------------------------------
```

```
    %Store XZ image results in 3D matrices
    OCT_Display_Complete(:,:,count)=OCT_Display;    %OCT intensity image
%     hFigure0=figure(0);
%     imagesc(OCT_Display);
%     colormap(gray(256));
%     colorbar('vert');
%     title(['Frame ', num2str(index)])
%     pause(0.1);

    dPhase_Complete(:,:,count)=dPhase;        %OCT doppler image
%     hFigure1=figure(1);
%     clim = [-pi, pi];
%     imagesc(dPhase,clim);
%     colormap(dmap);
%     colorbar('vert');
%     title(['Frame ', num2str(index)]);
%     pause(0.1);

    dVariance_Complete(:,:,count)=dVariance;
%     hFigure=figure(4);
%     clim = [0.5, 1];
%     imagesc(dVariance, clim)
%     colormap(hot)
%     colorbar('vert')
%     title(['Frame ', num2str(index)])
%     pause(0.1);

    count=count+1;
end

%-------------------------------------------------------------
%Unwrap DOCT images
% [OCT_Display_Final dPhase_Final dPhase_Complete_Proj
dPhase_Complete_unwrap]=DOCT_Unwrap(OCT_Display_Complete,dPhase_Complete);

%-------------------------------------------------------------
%Convert Doppler phase-shift (rad) to vertical velocity component(Vz)
lambda=0.001320;  %(mm) central wavelength of laser source (1320 nm)
if strcmpi(Scan,'B')
    f_a=16000;   %axial scanning frequency (Hz)
else
    f_a=8000;   %axial scanning frequency (Hz)
end
n=1.33;      %index of refraction for scattering medium (e.g. tissue)
dVelocity_Complete = (lambda*f_a/(4*pi*n)).*dPhase_Complete;  %velocity = mm/sec

%-------------------------------------------------------------
%Correct image aspect ratio
% [OCT_Display_Final dVelocity_Final DOCT_FlowRate
XSect_Area]=DOCT_AspectRatio_AreaIntegration(OCT_Display_Final,dVelocity_Final);

%OCT/DOCT image overlay
% [FusedImage]=OCT_DOCT_Overlay(OCT_Display_Final,dVelocity_Final);

%-------------------------------------------------------------
%Assign variable to workspace
% if exist('OCT_Display_Complete','var');
assignin('base','OCT_Display_Complete',OCT_Display_Complete); end;
% if exist('dPhase_Complete','var');
assignin('base','dPhase_Complete',dPhase_Complete); end;
% if exist('dVelocity_Complete','var');
assignin('base','dVelocity_Complete',dVelocity_Complete); end;
% if exist('dVariance_Complete','var');
assignin('base','dVariance_Complete',dVariance_Complete); end;
% if exist('DOCT_FlowRate','var');
assignin('base','DOCT_FlowRate',DOCT_FlowRate); end;
% if exist('XSect_Area','var');          assignin('base','XSect_Area',XSect_Area);
end;
% if exist('FusedImage','var');          assignin('base','FusedImage',FusedImage);
end;
```

```
%-----------------------------------------------------------
%Save variables in MAT file
% [path name]=fileparts(Filename);
% save(fullfile(path,[name,'_VARS.mat']),'OCT_Display_Complete','OCT_Display_Final',...
%
'dPhase_Complete','dPhase_Complete_Proj','dPhase_Complete_unwrap','dPhase_Final','dVel
ocity_Final');

%%
%%%%%%%%%%%%%%%%%%%%%%%%%%%%%%%%%%%%%%%%%%%%%%%%%%%%%%%%%%%%%%%%%%%%%%%%%%%%%%%%%%%%%%%
function [OCT_FRG_3D, depth, nFr, frame_start, frame_stop] =
Load_Thorlabs_DOCT_FRG_3D(f_name,frame_start, frame_stop)
%Load calibrated spectral fringes in k domain from "frame_start" to "frame_stop"

%Read File Header
fid = fopen(f_name, 'rb' );     %open link with FRG file ['rb' = read ('r') with full
precision ('b')]
% disp(f_name)          %display FRG filename
file_id = fread( fid, 16, 'uchar');        % File identification string
file_head = fread( fid, 6, 'int32' );      % File_header
nFr = file_head(1);                        % Number of images saved in the file
width = 992;                        % Image width
% width = file_head(2);                      % Image width
depth = file_head(3) ;                     % Image depth
nFrp3D = file_head(4);                     % Number of frames in each 3D volume
n3D = file_head(5);                        % Numer of 3D volumes
FFT_length = file_head(6);                 % FFT_length for OCT fringe
if FFT_length == 0
    FFT_length = 2*depth;
end
junk = fread(fid,118,'int32');             % Reversed bytes

frmLenBytes = 40 + width * FFT_length * 2;  % number of bytes per frame (40 bytes is
the length of sub header)
frmNpixels = FFT_length * width;    %number of pixels per frame

if strcmpi(frame_stop,'all')
    frame_stop=nFr;
end

%Read out frame fringe data
if frame_start > nFr
   disp(sprintf('frame_start larger than number of total frames: %d',nFr))
   frame_start = nFr;
   disp(sprintf('frame_start re_assigned to %d',nFr))
end

if frame_stop > nFr
   disp(sprintf('frame_stop larger than number of total frames: %d',nFr))
   frame_stop = nFr;
   disp(sprintf('frame_stop re_assigned to %d',nFr))
end

fseek(fid, (frame_start-1)*frmLenBytes, 'cof');
total_frames=frame_stop-frame_start+1;
frmId = 0;

%Save frame fringe data to 3D variable
OCT_FRG_3D=zeros(FFT_length,width,total_frames);
for frame_n = frame_start:frame_stop
    frmId = frmId + 1;
    disp(sprintf('...Frame loaded: %d',frame_n))
    elapsed_time(frmId) = fread( fid, 1, 'int32' );
    frame_info = fread( fid, 36, 'int8' );
    frame_data = fread( fid, frmNpixels, 'int16' );
    frame_data = reshape(frame_data, FFT_length, width);
    OCT_FRG_3D(:,:,frmId) = frame_data;
end

fclose(fid);    %close link with OCT (.FRG) file
```

```
%%
%%%%%%%%%%%%%%%%%%%%%%%%%%%%%%%%%%%%%%%%%%%%%%%%%%%%%%%%%%%%%%%%%%%%%%%%%%%%%%%%%%%%%%

function Fringe_apodiz = Fringe_apodization(Fringe_k, apodiz_method)
%%%%%%%%%%%%%%%%%%%%%%%%Inputs%%%%%%%%%%%%%%%%%%%%%%%%
% Fringe_k = fringe data from OCT scan
% apodiz_method = 'Cosine', 'Gaussian', 'Super_Gaussian','Hann','Hamming',
            %'Blackman', 'Nuttall', 'Blackman_Harris'*,'none'

%%%%%%%%%%%%%%%%%%%%%%%%Outputs%%%%%%%%%%%%%%%%%%%%%%%%
% Fringe_apodiz = fringe data with applied window function

%-----------------------------------------
%Window function for OCT fringe data apodization
[index_length, width] = size(Fringe_k);
window_band = 0.5*index_length;
depth_index = (1:index_length) - round(index_length/2);

switch apodiz_method
    case 'Kaiser'
         disp('Kaiser window')
         alpha = 2;
         index = (1:index_length)-1;
         v = pi*alpha*sqrt(1 - (2*index/(index_length-1) -1).^2);
         window = (besseli(0,v)./besseli(0,pi*alpha))'*ones(1,width); %'Kaiser'
    case 'Cosine'
         disp('Cosine window')
         window = cos(pi*depth_index./index_length)'*ones(1,width); %'Cosine'
    case 'Super_Gaussian'
         disp('Super Gaussian window')
         window = exp(-(depth_index./window_band).^4)'*ones(1,width); %'super
Gaussian'
    case 'Gaussian'
         disp('Gaussian window')
         window = exp(-(depth_index./window_band).^2)'*ones(1,width); %'Gaussian'
    case 'Hamming'
          disp('Hamming window')
         window =(0.53836 - 0.46164*cos(2*pi*(1:index_length)./(index_length-
1)))'*ones(1,width); %Hamming
    case 'Hann'
          disp('Hann window')
          window = (0.5 - 0.5*cos(2*pi*(1:index_length)./(index_length-
1)))'*ones(1,width); %Hann
    case 'Blackman'
          disp('Blackman window')
          window =(0.42 - 0.5*cos(2*pi*(1:index_length)./(index_length-1)) + ...
             0.08*cos(4*pi*(1:index_length)./(index_length-1)))'*ones(1,width);
%Blackman
    case 'Nuttall'
          disp('Nuttal window')
          window =(0.355768 - 0.487396*cos(2*pi*(1:index_length)./(index_length-
1))+ ...
              + 0.144232*cos(4*pi*(1:index_length)./(index_length-1))- ...
              0.012604*cos(6*pi*(1:index_length)./(index_length-1)))'*ones(1,width);
%Nuttall
    case 'Blackman_Harris'
          disp('Blackman_Harris window')
          window =(0.35875 - 0.48829*cos(2*pi*(1:index_length)./(index_length-1))+ ...
              + 0.14128*cos(4*pi*(1:index_length)./(index_length-1))- ...
              0.01168*cos(6*pi*(1:index_length)./(index_length-1)))'*ones(1,width);
%Blackman_Harris
     otherwise
         disp('Rectangular window')
         window = 1;    %Rectangular
end
Fringe_apodiz = Fringe_k.*window;


%%
%%%%%%%%%%%%%%%%%%%%%%%%%%%%%%%%%%%%%%%%%%%%%%%%%%%%%%%%%%%%%%%%%%%%%%%%%%%%%%%%%%%%%%
```

```
function OCT_complex = Compute_Analytical(Fringe, FFT_length, image_depth)

%Calculte complex OCT fringes from the k domain spectral fringes
complex_temp = ifft(Fringe,FFT_length);

%Cut off the mirror conjugate image
OCT_image = abs(complex_temp(1:image_depth,:));

%Take last 1/10 pixels of A-line for calculation of the noise level
aver_fract = 1/10;
aver_pixel = round(image_depth*aver_fract);
level_noise = sum(OCT_image((image_depth - aver_pixel):image_depth,:))/(aver_pixel+1);
level_noise_matrix = ones(image_depth,1)*level_noise;

%Normzlize the OCT complex signal to the noise background
OCT_complex = complex_temp(1:image_depth,:).*(1./level_noise_matrix);


%%
%%%%%%%%%%%%%%%%%%%%%%%%%%%%%%%%%%%%%%%%%%%%%%%%%%%%%%%%%%%%%%%%%%%%%%%%%%%%%%%%%%%%%%%

function [OCT_Intensity dPhase dVariance] = Phase_Resolve_DOCT(complex_signal,
BulkMotionRemoval,...

dThreshold_Intensity,dThreshold_Variance,start_ref,end_ref,ref_points,bin_size,shift_d
epth,shift_width,...
    OCT_ave_depth,OCT_ave_width,DOCT_ave_depth,DOCT_ave_width)

%Display bulk removal method
disp(['Bulk Motion Removal Method = ',BulkMotionRemoval]);

OCT_area = OCT_ave_depth*OCT_ave_width;  % number of data points in OCT sliding
average window
DOCT_area = DOCT_ave_depth*DOCT_ave_width;  % number of data points in DOCT sliding
average window

%Get size of data for Doppler calculation
[data_depth data_width] = size(complex_signal);

% data_re and next_re are adjacent real part of the complex A-line signal
% data_im and next_im are adjacent imag part of the complex A-line signal
data_re = real(complex_signal(:,1:data_width-1));
data_im = imag(complex_signal(:,1:data_width-1));
next_re = real(complex_signal(:,2:data_width));
next_im = imag(complex_signal(:,2:data_width));
clear complex_signal

if BulkMotionRemoval == 'C'
    %Calculate intensity threshold used in complex vector bulk motion removal method
    dThreshold_Intensity_ref = dThreshold_Intensity - 10*log10(DOCT_area);

    %Complex vector method for bulk motion removal
    [next_re, next_im] = bulk_removal(data_re, data_im, next_re, next_im,start_ref,
end_ref, ref_points, dThreshold_Intensity_ref);
end

%Calcualte OCT intensity image
dR1 = data_re.^2 + data_im.^2;

%Calculate real and imaginary components of Doppler signal using adjacent complex A-
scan fringes
dRx =  data_re.*next_re + data_im.*next_im; %real component
dRy =  data_im.*next_re - data_re.*next_im;  %imaginary component
clear  data_re data_im next_re next_im

%Calculate the image size for intensity, dPhase, and dVariance images
img_depth = floor((data_depth - DOCT_ave_depth)/shift_depth);
img_width = floor((data_width - DOCT_ave_width - 1)/shift_width);   %-1 to account for
size of image after taking difference between axial scans
```

```
%Pre-allocate variables
OCT_Intensity = zeros(img_depth, img_width);
dRR1 = zeros(img_depth, img_width);
dRX = zeros(img_depth, img_width);
dRY = zeros(img_depth, img_width);

%Calculate OCT intensity, and real and imag components of Doppler signal by sliding
average window
%hWait = waitbar(0,'Computing Doppler OCT');
for j = 1:img_width
  for i = 1:img_depth
      %OCT Intensity Window Range
      OCT_depth_win1 = (i-1)*shift_depth + 1;
      OCT_depth_win2 = (i-1)*shift_depth + 1 + OCT_ave_depth;
      OCT_depth_range = OCT_depth_win1:OCT_depth_win2;
      OCT_width_win1 = (j-1)*shift_width + 1;
      OCT_width_win2 = (j-1)*shift_width + 1 + OCT_ave_width;
      OCT_width_range = OCT_width_win1:OCT_width_win2;

      %Doppler OCT (DOCT) Window Range
      DOCT_depth_win1 = (i-1)*shift_depth + 1;
      DOCT_depth_win2 = (i-1)*shift_depth + DOCT_ave_depth;
      DOCT_depth_range = DOCT_depth_win1:DOCT_depth_win2;
      DOCT_width_win1 = (j-1)*shift_width + 1;
      DOCT_width_win2 = (j-1)*shift_width + DOCT_ave_width;
      DOCT_width_range = DOCT_width_win1:DOCT_width_win2;

      %Calculations
      OCT_Intensity(i,j) = sum(sum(dR1(OCT_depth_range,OCT_width_range))); %intensity
(using OCT window)
      dRR1(i,j) = sum(sum(dR1(DOCT_depth_range,DOCT_width_range)));  %intensity (using
DOCT window)
      dRX(i,j) = sum(sum(dRx(DOCT_depth_range,DOCT_width_range)));  %real component
      dRY(i,j) = sum(sum(dRy(DOCT_depth_range,DOCT_width_range)));  %imaginary
component
  end
%  waitbar(j/img_width,hWait);
end
%close(hWait);
pause(0.1);
clear dR1 dRx dRy

%Calculate freq-shift (or phase-shift) and variance of Doppler OCT signal
dPhase = atan2(dRY./(DOCT_ave_depth*(DOCT_ave_width-
1)),dRX./(DOCT_ave_depth*(DOCT_ave_width-1)));
dVariance = 1 - sqrt(dRX.^2 + dRY.^2)./dRR1;

%-----------------------------------------------------
if BulkMotionRemoval == 'H'
    %Histogram method for bulk motion removal
    dPhase = BulkMotionRemoval_Histogram(dPhase,start_ref,end_ref,bin_size);
end

%Suppress noise where singal intensity is small than the intensity threshold
dPhase(10*log10(dRR1) < dThreshold_Intensity) = 0;
dVariance(10*log10(dRR1) < dThreshold_Intensity) = 0;

%Suppress velocity noise where variance is small than the variance threshold
dPhase(dVariance < dThreshold_Variance) = 0;

%Renormalize the OCT intensity by the number of pixels in the sliding average window
OCT_Intensity = OCT_Intensity/OCT_area;

%%
%%%%%%%%%%%%%%%%%%%%%%%%%%%%%%%%%%%%%%%%%%%%%%%%%%%%%%%%%%%%%%%%%%%%%%%%%%%%%%%%%%%%%%%

function OCT_display = OCT_mapping(OCT_linear, Contrast, Brightness)

[height width]= size(OCT_linear);

%Calculate max A-scan value
```

```
[Aline_max Aline_pos] = max(max(OCT_linear));  % find max intensity in OCT image

%Calculate of the noise backgroud at the refrence A-scan
aver_fract = 1/10;  %take last 1/10 of pixels of A-scan
noise_level = sum(OCT_linear(round((1-
aver_fract)*height):height,Aline_pos))/(height*aver_fract);

%Calculate dynamic range of OCT image
dB_Range = 10*log10(Aline_max/noise_level);

%Convert OCT signal in linear scale into dB and map it to range [0, 255]
OCT_log = (10*log10(OCT_linear/Aline_max) + dB_Range)/dB_Range*255;

%Remap OCT image using Contrast and  Brightness settings
OCT_display = Contrast*(OCT_log) + Brightness;
OCT_display(OCT_display > 255) = 255;
OCT_display(OCT_display < 0) = 0;


%%
%%%%%%%%%%%%%%%%%%%%%%%%%%%%%%%%%%%%%%%%%%%%%%%%%%%%%%%%%%%%%%%%%%%%%%%%%%%%%%%%%%%%%%

function [next_re, next_im] = bulk_removal(data_re, data_im, next_re, next_im,
start_ref, end_ref, ref_points, dThreshold_Intensity_ref)

%Bulk motion removal in complex domain using a complex vector
[data_depth, data_width] = size(data_re);

for k = 1:data_width
    %Reset variable values
    tempX = 0;
    tempY = 0;
    tempR = 0;

    %Start referece of every A-line
    j = start_ref;
    ref_num = 0;
    %For evey A-line, find intensity data points that is large enought in the
reference range
        % and accumulate the real--X and imag-- Y part of the Doppler signal of the
bulk motion
    while (ref_num < ref_points) && (j>=start_ref) && (j<=end_ref)
    tempR = next_re(j,k).*next_re(j,k) + next_im(j,k).*next_im(j,k);
    if (10*log10(tempR) > dThreshold_Intensity_ref);
       tempX = tempX + (data_re(j,k).*next_re(j,k) + data_im(j,k).*next_im(j,k));
       tempY = tempY + (data_im(j,k).*next_re(j,k) - data_re(j,k).*next_im(j,k));
       ref_num = ref_num +1;
    end
    j = j +1;
    end
    %Calculate the Doppler power
    tempR = sqrt(tempX.^2+ tempY.^2);

    %When the number of data points is large than half of the
        % reference data points, calculate the normalized real and imag
        % part of the Dopperl signal of the bulk motion
    if (ref_points~=0) && (ref_num > ref_points/3)
        tempX = tempX/tempR ;
        tempY = -tempY/tempR;
    else
        tempX = 1;
        tempY = 0;
    end
    %Remove bulk motion from every other A-line fringes
    dR = next_re(:,k).*tempX + next_im(:,k).*tempY;
    next_im(:,k) = next_im(:,k).*tempX -next_re(:,k).*tempY;
    next_re(:,k) = dR;
end


%%%%%%%%%%%%%%%%%%%%%%%%%%%%%%%%%%%%%%%%%%%%%%%%%%%%%%%%%%%%%%%%%%%%%%%%%%%%%%%%%%%%%%
```

```
%%
%%%%%%%%%%%%%%%%%%%%%%%%%%%%%%%%%%%%%%%%%%%%%%%%%%%%%%%%%%%%%%%%%%%%%%%%%%%%%%%%%%%%%%

function KasaiClean=BulkMotionRemoval_Histogram(Kasai, lascan, uascan, bin_size)
%Histogram Algorithm
%Define Bulk Motion Removal Paramaters
%This function accepts the doppler image (you can use 1 line of the
%doppler image at a time or all 512 lines depending on how your code works)
%lascan defines the start of the tissue region (top of image is 1)
%uascan defines bottom of the tissur region.
%I would suggest setting it up so that lascan and uascan are fixed at first
%to the top 2/3 of the screen (lascan=1,uascan=350) since this is usually where we get
signal
%from.

half_bin_size = bin_size/2;

%Remove bulk motion for each A scan
for i=1:size(Kasai,2)
    clear HKasai
    clear MaxKasai

    %Determine the phase shift of the majority of pixels using a
    %histogram of the a scan with specified bin size.
    HKasai=hist(Kasai(lascan:uascan,i), -pi:(2*pi/(bin_size-1)):pi);
    A=mean(find(HKasai==max(HKasai)));

    %Rotate A scan data between [-pi pi] so that the peak of the histogram
    %zero-centered (i.e. the maximum phase shift is shifted to zero).
    if (A > half_bin_size)
        MaxKasai=(A-half_bin_size)*pi/half_bin_size;
    else
        MaxKasai=-(half_bin_size-A)*pi/half_bin_size;
    end
    Kasai(:,i)=-Kasai(:,i)+(MaxKasai);

    %Wrap the phase again after zero-centering the histogram peak
    outside_lower=find(Kasai(:,i) < -pi);
    Kasai(outside_lower,i)=Kasai(outside_lower,i)+(2*pi);
    outside_upper=find(Kasai(:,i) > pi);
    Kasai(outside_upper,i)=Kasai(outside_upper,i)-(2*pi);

    clear outside_upper
    clear outside_lower
end
KasaiClean=-Kasai;

%%
%%%%%%%%%%%%%%%%%%%%%%%%%%%%%%%%%%%%%%%%%%%%%%%%%%%%%%%%%%%%%%%%%%%%%%%%%%%%%%%%%%%%%%
```

Appendix B

Matlab code for ROI selection, bulk motion remove and DOCT unwarpping.

```
% Combinging multiple mat files to one file with selected frame inteval
% Should have OCT3D, DOCT3D and SV files ready before using this program

finterval=5; % frame interval
[filename,pathname] = uigetfile( ...
       {'*.mat','mat Files (*.mat)';'*.*', 'All Files (*.*)'}, ...
        'Select files','MultiSelect','on'); % select all OCT3D files for merging.
    for i=1:length(filename)
        Filename = fullfile(pathname,filename{i});
        [a,b]=fileparts(filename{i});
        SVfname=strrep(b,'_OCT3D','_SV.mat');
        DOCTfname=strrep(b,'_OCT3D','_DOCT3D.mat');
        PVfname=strrep(b,'_OCT3D','_Variance3D.mat');

        OCTFname=Filename;
        SVFname=fullfile(pathname,SVfname);
        DOCTFname=fullfile(pathname,DOCTfname);
        PVFname=fullfile(pathname,PVfname);


        oct=load(OCTFname);
        OCT=oct.OCT_Display_Complete;
        OCT=OCT(:,:,1:finterval:end);

        doct=load(DOCTFname);
        DOCT=doct.dVelocity_Complete;
        DOCT=DOCT(:,:,1:finterval:end);

        sv=load(SVFname);
        SV=sv.SV;
        SV=SV(:,:,1:finterval:end);

        pv=load(PVFname);
        PV=pv.dVariance_Complete;
        PV=PV(:,:,1:finterval:end);


        if i<=1;
            OCT_C=OCT;
            DOCT_C=DOCT;
            SV_C=SV;
            PV_C=PV;
        else
            OCT_C=cat(3,OCT_C,OCT);% Combing multiple files.
            DOCT_C=cat(3,DOCT_C,DOCT);
            SV_C=cat(3,SV_C,SV);
            PV_C=cat(3,PV_C,PV);

        end
    end

        Of_name='m2l_OCT_C.mat';
        Df_name='m2l_DOCT_C.mat';
        SVf_name='m2l_SV_C.mat';
        PVf_name='m2l_PV_C.mat';
        Ooutpath=fullfile(pathname,Of_name);
        Doutpath=fullfile(pathname,Df_name);
        SVoutpath=fullfile(pathname,SVf_name);
        PVoutpath=fullfile(pathname,PVf_name);

        save(Ooutpath,'OCT_C');
        save(Doutpath,'DOCT_C');
        save(SVoutpath,'SV_C');
        save(PVoutpath,'PV_C');
```

```
%%%%%%%%%%%%%%%%%%%%%%%%%%%%%%%%%%%%%%%%%%%%%%%%%%%%%%%%%%%%%%%%%%%%%%%%%%%%%%%

%%% Removing the bulk motion by rejecting the SV frames with high intensity
a=sum(sum(SV_C));
b(1:size(a,3))=a(1,1,:);
b=double(b);
[pks,locs] = findpeaks(-b); % searching the frames with peak intesnity
a=find(pks<-4*10^6|pks==0);
locs(a)=[];

plot(b);hold on;
plot(locs,b(locs)+0.05,'k^','markerfacecolor',[1 0 0]);

time=(0:600/size(OCT_C,3):600);
time=time(1:size(time,2)-1);
time=time(locs);

SV_C_c=SV_C(:,:,locs);
OCT_C_c=OCT_C(:,:,locs);
DOCT_C_c=DOCT_C(:,:,locs);
PV_C_c=PV_C(:,:,locs);


%%%%%%%%%%%%%%%%%%%%%%%%%%%%%%%%%%%%%%%%%%%%%%%%%%%%%%%%%%%%%%%%%%%%%%%%%%%%%%%
% measuring the lateral size of blood vessel.

figure('Color',[1 1 1]);
set(gcf,'Position',[0 0 18000 900]);
vdepth=20;
% width=7; %convolution width; only odd number

for i=1:size(SV_C_c,3)
% Emap=single(edge(SV_C_c(:,:,10))); %edge map;binary map; conv2 doesn't accetp logic
map;
% SEmap=conv2(Emap,ones(width)); % Smoothed Emap; dispersed island
% SEmap=imresize(SEmap,size(SV_C_c(:,:,i)));

OCT=imresize(OCT_C_c(:,:,i),[512 120]);
DOCT=imresize(DOCT_C_c(:,:,i),[512 120]);
PV=imresize(PV_C_c(:,:,i),[512 120]);
SV=double(imresize(SV_C_c(:,:,i),[512 120]));
SV_C_C=SV(:,40:120);

SEmap=imfill(SV_C_C,'holes');
SEmap(SEmap<110)=0; % converted to binary map
SEmap(SEmap>=110)=1;
L=bwlabeln(SEmap); % Labeled map; One distinctive number is assigned to each
individual island in the SEmap

for j=1:max(max((L)))
    E=(L==j);
    Area(j)=sum(E(:)); % the area of each island
end
label=find(Area==max(Area)); % finding the label assigned to the largest island
% ROI(:,:,i)=(L==label); % The ROI is defined to largest island.
ROI_C=(L==label); % The ROI is defined to largest island.
ROI_C1(:,:,i)=cat(2,zeros(512,39),ROI_C);
ROI=ROI_C1(:,:,i);


[row, col]=find(ROI==1);
for k=1:vdepth
    rowinitial=min(row);% start with the shallowest row
    r=rowinitial+k-1;
    if r>max(row)
        break
    else
    rindex=find(row==r);
    vwidth(k)=col(max(rindex))-col(min(rindex));
    clear rindex;
```

```
    end
end
Vwidth(i)=median(vwidth);
clear area;

DOCT1=DOCT.*ROI;
DOCT1(DOCT1<-0.3)=DOCT1(DOCT1<-0.3)+2*pi;% DOCT unwrap
flow(i)=sum(sum(DOCT1.*ROI))/sum(sum(ROI));


DOCT(DOCT<-0.3)=DOCT(DOCT<-0.3)+2*pi;


OCT_s=Ind2RGB_Convert(sepia,OCT,[20 250]);
DOCT_d=Ind2RGB_Convert(DOCT_Colormap,DOCT,[-pi pi]);
SV_h=Ind2RGB_Convert(hot,SV,[0  600]);
ROI_g=Ind2RGB_Convert(gray,ROI,[0 1]);

subplot(141);imshow(OCT_s); title(['OCT ',num2str(time(i))]);
subplot(142);imshow(DOCT_d);title('DOCT');
subplot(143);imshow(SV_h);title('SV');
subplot(144);imshow(ROI_g);title('ROI');

ROImov(i)=getframe(gcf);

end

% save varaiables and plot the data
save('C:\Users\Chia Pin\Desktop\NCI\publication\data\082913m1l_Vwidth.mat','Vwidth');
save('C:\Users\Chia Pin\Desktop\NCI\publication\data\082913m1l_flow.mat','flow');
save('C:\Users\Chia Pin\Desktop\NCI\publication\data\082913m1l_ROImov.mat','ROImov');
subplot(211);plot(Vwidth);
subplot(212);plot(flow);

e1=round(size(Vwidth,2)/10);
I=size(Vwidth,2)-e1;
e2=size(Vwidth,2);
mean(Vwidth(I:e2))/mean(Vwidth(1:e1))

flow1=flow;
% flow1(locs)=[];
mean(flow1(I:e2)) /mean(flow1(1:e1))
```

Reference

1. C. M. Owen, and M. E. Linskey, "Frame-based stereotaxy in a frameless era: current capabilities, relative role, and the positive- and negative predictive values of blood through the needle," J. Neuro-Oncol. **93**, 139-149 (2009).
2. H. J. Colbassani, S. Nishio, K. M. Sweeney, R. A. E. Bakay, and Y. Takei, "CT-assisted stereotactic brain biopsy - value of intraoperative frozen section diagnosis," Journal of Neurology Neurosurgery and Psychiatry **51**, 332-341 (1988).
3. N. K. Venkataramana, S. K. V. Kumar, S. Balaraju, R. C. Radhakrishnan, A. Bansal, A. Dixit, D. K. Rao, M. Das, M. Jan, P. K. Gupta, and S. M. Totey, "Open-labeled study of unilateral autologous bone-marrow-derived mesenchymal stem cell transplantation in Parkinson's disease," Translational Research **155**, 62-70 (2010).
4. B. Z. Roitberg, N. Khan, M. S. Alp, T. Hersonskey, F. T. Charbel, and J. I. Ausman, "Bedside external ventricular drain placement for the treatment of acute hydrocephalus," British Journal of Neurosurgery **15**, 324-327 (2001).
5. P. Limousin, P. Krack, P. Pollak, A. Benazzouz, C. Ardouin, D. Hoffmann, and A. L. Benabid, "Electrical stimulation of the subthalamic nucleus in advanced Parkinson's disease," N. Engl. J. Med. **339**, 1105-1111 (1998).
6. P. A. Starr, "Placement of deep brain stimulators into the subthalamic nucleus or Globus pallidus internus: technical approach," Stereotact Funct Neurosurg **79**, 118-145 (2002).
7. P. D. Sawin, P. W. Hitchon, K. A. Follett, and J. C. Torner, "Computed imaging-assisted stereotactic brain biopsy - A risk analysis of 225 consecutive cases," Surgical Neurology **49**, 640-649 (1998).
8. D. K. Binder, G. Rau, and P. A. Starr, "Hemorrhagic complications of microelectrode-guided deep brain stimulation," Stereotact Funct Neurosurg **80**, 28-31 (2003).
9. D. K. Binder, G. M. Rau, and P. A. Starr, "Risk factors for hemorrhage during microelectrode-guided deep brain stimulator implantation for movement disorders," Neurosurgery **56**, 722-732; discussion 722-732 (2005).
10. W. A. Hall, "The safety and efficacy of stereotactic biopsy for intracranial lesions," Cancer **82**, 1749-1755 (1998).
11. M. I. Hariz, "Complications of deep brain stimulation surgery," Movement Disorders **17**, S162-S166 (2002).
12. A. E. Lang, S. Gill, N. K. Patel, A. Lozano, J. G. Nutt, R. Penn, D. J. Brooks, G. Hotton, E. Moro, P. Heywood, M. A. Brodsky, K. Burchiel, P. Kelly, A. Dalvi, B. Scott, M. Stacy, D. Turner, V. G. F. Wooten, W. J. Elias, E. R. Laws, V. Dhawan, A. J. Stoessl, J. Matcham, R. J. Coffey, and M. Traub, "Randomized controlled trial of intraputamenal glial cell line-derived neurotrophic factor infusion in Parkinson disease," Ann. Neurol. **59**, 459-466 (2006).

13. B. D. Greenberg, L. A. Gabriels, D. A. Malone, Jr., A. R. Rezai, G. M. Friehs, M. S. Okun, N. A. Shapira, K. D. Foote, P. R. Cosyns, C. S. Kubu, P. F. Malloy, S. P. Salloway, J. E. Giftakis, M. T. Rise, A. G. Machado, K. B. Baker, P. H. Stypulkowski, W. K. Goodman, S. A. Rasmussen, and B. J. Nuttin, "Deep brain stimulation of the ventral internal capsule/ventral striatum for obsessive-compulsive disorder: worldwide experience," Mol Psychiatry **15**, 64-79 (2008).
14. D. A. Malone, Jr., D. D. Dougherty, A. R. Rezai, L. L. Carpenter, G. M. Friehs, E. N. Eskandar, S. L. Rauch, S. A. Rasmussen, A. G. Machado, C. S. Kubu, A. R. Tyrka, L. H. Price, P. H. Stypulkowski, J. E. Giftakis, M. T. Rise, P. F. Malloy, S. P. Salloway, and B. D. Greenberg, "Deep brain stimulation of the ventral capsule/ventral striatum for treatment-resistant depression," Biol Psychiatry **65**, 267-275 (2009).
15. J. M. Henderson, ""Connectomic surgery": diffusion tensor imaging (DTI) tractography as a targeting modality for surgical modulation of neural networks," Front Integr Neurosci **6**, 15 (2012).
16. M. Mitsunaga, T. Nakajima, K. Sano, P. L. Choyke, and H. Kobayashi, "Near-infrared theranostic photoimmunotherapy (PIT): repeated exposure of light enhances the effect of immunoconjugate," Bioconjug Chem **23**, 604-609.
17. M. Mitsunaga, M. Ogawa, N. Kosaka, L. T. Rosenblum, P. L. Choyke, and H. Kobayashi, "Cancer cell-selective in vivo near infrared photoimmunotherapy targeting specific membrane molecules," Nat Med **17**, 1685-1691.
18. K. Sano, T. Nakajima, P. L. Choyke, and H. Kobayashi, "Markedly enhanced permeability and retention effects induced by photo-immunotherapy of tumors," ACS Nano **7**, 717-724.
19. A. V. Kulkarni, A. Guha, A. Lozano, and M. Bernstein, "Incidence of silent hemorrhage and delayed deterioration after stereotactic brain biopsy," J Neurosurg **89**, 31-35 (1998).
20. P. N. Kongkham, E. Knifed, M. S. Tamber, and M. Bernstein, "Complications in 622 cases of frame-based stereotactic biopsy, a decreasing procedure," Can J Neurol Sci **35**, 79-84 (2008).
21. M. Nishihara, T. Sasayama, H. Kudo, and E. Kohmura, "Morbidity of stereotactic biopsy for intracranial lesions," Kobe J Med Sci **56**, E148-153 (2010).
22. F. M. Skidmore, R. L. Rodriguez, H. H. Fernandez, W. K. Goodman, K. D. Foote, and M. S. Okun, "Lessons learned in deep brain stimulation for movement and neuropsychiatric disorders," Cns Spectrums **11**, 521-+ (2006).
23. P. Mohr, "Deep Brain Stimulation in Psychiatry," Neuroendocrinol Lett **29**, 123-132 (2008).
24. E. D. Flora, C. L. Perera, A. L. Cameron, and G. J. Maddern, "Deep Brain Stimulation for Essential Tremor: A Systematic Review," Movement Disorders **25**, 1550-1559 (2010).
25. C. Andrews, I. Aviles-Olmos, M. Hariz, and T. Foltynie, "Which patients with dystonia benefit from deep brain stimulation? A metaregression of individual patient outcomes," Journal of Neurology Neurosurgery and Psychiatry **81**, 1383-1389 (2010).

26. T. Terao, H. Takahashi, F. Yokochi, M. Taniguchi, R. Okiyama, and I. Hamada, "Hemorrhagic complication of stereotactic surgery in patients with movement disorders," J Neurosurg **98**, 1241-1246 (2003).
27. G. Deuschl, J. Herzog, G. Kleiner-Fisman, C. Kubu, A. M. Lozano, K. E. Lyons, M. C. Rodriguez-Oroz, F. Tamma, A. I. Troster, J. L. Vitek, J. Volkmann, and V. Voon, "Deep brain stimulation: Postoperative issues," Movement Disorders **21**, S219-S237 (2006).
28. J. Voges, R. Hilker, K. Botzel, K. L. Kiening, M. Moss, A. Kupsch, A. Schnitzler, G. H. Schneider, U. Steude, G. Deuschl, and M. O. Pinsker, "Thirty days complication rate following surgery performed for deep-brain-stimulation," Movement Disorders **22**, 1486-1489 (2007).
29. C. A. Sansur, R. C. Frysinger, N. Pouratian, K. M. Fu, M. Bittl, R. J. Oskouian, E. R. Laws, and W. J. Elias, "Incidence of symptomatic hemorrhage after stereotactic electrode placement," J Neurosurg **107**, 998-1003 (2007).
30. J. M. Bronstein, M. Tagliati, R. L. Alterman, A. M. Lozano, J. Volkmann, A. Stefani, F. B. Horak, M. S. Okun, K. D. Foote, P. Krack, R. Pahwa, J. M. Henderson, M. I. Hariz, R. A. Bakay, A. Rezai, W. J. Marks, Jr., E. Moro, J. L. Vitek, F. M. Weaver, R. E. Gross, and M. R. DeLong, "Deep brain stimulation for Parkinson disease: an expert consensus and review of key issues," Arch Neurol **68**, 165 (2010).
31. A. Gorgulho, A. A. De Salles, L. Frighetto, and E. Behnke, "Incidence of hemorrhage associated with electrophysiological studies performed using macroelectrodes and microelectrodes in functional neurosurgery," J Neurosurg **102**, 888-896 (2005).
32. H. Hirabayashi, M. Tengvar, and M. I. Hariz, "Stereotactic imaging of the pallidal target," Mov Disord **17 Suppl 3**, S130-134 (2002).
33. A. Funkiewiez, E. Caputo, C. Ardouin, P. Krack, V. Fraix, A. L. Benabid, and P. Pollak, "Behavioral and mood changes associated with bilateral stimulation of the subthalamic nucleus: A consecutive series of 98 parkinsonian patients," Neurology **56**, A274-A274 (2001).
34. R. E. Gross, P. Krack, M. C. Rodriguez-Oroz, A. R. Rezai, and A. L. Benabid, "Electrophysiological mapping for the implantation of deep brain stimulators for Parkinson's disease and tremor," Movement Disorders **21**, S259-S283 (2006).
35. S. Baudrexel, T. Witte, C. Seifried, F. von Wegner, F. Beissner, J. C. Klein, H. Steinmetz, R. Deichmann, J. Roeper, and R. Hilker, "Resting state fMRI reveals increased subthalamic nucleus-motor cortex connectivity in Parkinson's disease," Neuroimage **55**, 1728-1738 (2011).
36. T. Wu, P. Chan, and M. Hallett, "Effective connectivity of neural networks in automatic movements in Parkinson's disease," Neuroimage **49**, 2581-2587 (2010).
37. K. L. Poston, and D. Eidelberg, "Functional brain networks and abnormal connectivity in the movement disorders," Neuroimage (2011).

38. C. Hauptmann, and P. A. Tass, "Restoration of segregated, physiological neuronal connectivity by desynchronizing stimulation," J Neural Eng **7**, 056008 (2010).
39. M. Mitsunaga, M. Ogawa, N. Kosaka, L. T. Rosenblum, P. L. Choyke, and H. Kobayashi, "Cancer cell-selective in vivo near infrared photoimmunotherapy targeting specific membrane molecules," Nat Med **17**, 1685-U1210 (2011).
40. M. S. Jafri, S. Farhang, R. S. Tang, N. Desai, P. S. Fishman, R. G. Rohwer, C. M. Tang, and J. M. Schmitt, "Optical coherence tomography in the diagnosis and treatment of neurological disorders," J Biomed Opt **10**, 051603 (2005).
41. C. P. Liang, J. Wierwille, T. Moreira, G. Schwartzbauer, M. S. Jafri, C. M. Tang, and Y. Chen, "A forward-imaging needle-type OCT probe for image guided stereotactic procedures," Optics express **19**, 26283-26294 (2011).
42. H. Wang, A. J. Black, J. Zhu, T. W. Stigen, M. K. Al-Qaisi, T. I. Netoff, A. Abosch, and T. Akkin, "Reconstructing micrometer-scale fiber pathways in the brain: multi-contrast optical coherence tomography based tractography," Neuroimage **58**, 984-992 (2011).
43. M. S. Jafri, R. Tang, and C. M. Tang, "Optical coherence tomography guided neurosurgical procedures in small rodents," Journal of Neuroscience Methods **176**, 85-95 (2009).
44. Y. L. Jia, and R. K. Wang, "Label-free in vivo optical imaging of functional microcirculations within meninges and cortex in mice," Journal of Neuroscience Methods **194**, 108-115 (2010).
45. B. J. Vakoc, D. Fukumura, R. K. Jain, and B. E. Bouma, "Cancer imaging by optical coherence tomography: preclinical progress and clinical potential," Nat Rev Cancer **12**, 363-368.
46. B. A. Standish, K. K. Lee, X. Jin, A. Mariampillai, N. R. Munce, M. F. Wood, B. C. Wilson, I. A. Vitkin, and V. X. Yang, "Interstitial Doppler optical coherence tomography as a local tumor necrosis predictor in photodynamic therapy of prostatic carcinoma: an in vivo study," Cancer Res **68**, 9987-9995 (2008).
47. G. J. Tearney, M. E. Brezinski, B. E. Bouma, S. A. Boppart, C. Pitvis, J. F. Southern, and J. G. Fujimoto, "In vivo endoscopic optical biopsy with optical coherence tomography," Science (New York, N.Y **276**, 2037-2039 (1997).
48. Z. Yaqoob, J. Wu, E. J. McDowell, X. Heng, and C. Yang, "Methods and application areas of endoscopic optical coherence tomography," J Biomed Opt **11**, 063001 (2006).
49. J. M. Zara, and C. A. Lingley-Papadopoulos, "Endoscopic OCT approaches toward cancer diagnosis," Ieee Journal of Selected Topics in Quantum Electronics **14**, 70-81 (2008).
50. G. J. Tearney, S. A. Boppart, B. E. Bouma, M. E. Brezinski, N. J. Weissman, J. F. Southern, and J. G. Fujimoto, "Scanning single-mode fiber optic catheter-endoscope for optical coherence tomography," Optics letters **21**, 543-545 (1996).
51. B. E. Bouma, and G. J. Tearney, "Power-efficient nonreciprocal interferometer and linear-scanning fiber-optic catheter for optical coherence tomography," Optics letters **24**, 531-533 (1999).

52. V. X. D. Yang, Y. X. Mao, N. Munce, B. Standish, W. Kucharczyk, N. E. Marcon, B. C. Wilson, and I. A. Vitkin, "Interstitial Doppler optical coherence tomography," Optics letters **30**, 1791-1793 (2005).
53. A. R. Tumlinson, B. Povazay, L. P. Hariri, J. McNally, A. Unterhuber, B. Hermann, H. Sattmann, W. Drexler, and J. K. Barton, "In vivo ultrahigh-resolution optical coherence tomography of mouse colon with an achromatized endoscope," J Biomed Opt **11**, 064003 (2006).
54. A. R. Tumlinson, J. K. Barton, B. Povazay, H. Sattman, A. Unterhuber, R. A. Leitgeb, and W. Drexler, "Endoscope-tip interferometer for ultrahigh resolution frequency domain optical coherence tomography in mouse colon," Optics express **14**, 1878-1887 (2006).
55. H. L. Fu, Y. Leng, M. J. Cobb, K. Hsu, J. H. Hwang, and X. Li, "Flexible miniature compound lens design for high-resolution optical coherence tomography balloon imaging catheter," J Biomed Opt **13**, 060502 (2008).
56. V. X. D. Yang, N. Munce, J. Pekar, M. L. Gordon, S. Lo, N. E. Marcon, B. C. Wilson, and I. A. Vitkin, "Micromachined array tip for multifocus fiber-based optical coherence tomography," Optics Letters **29**, 1754-1756 (2004).
57. Y. Takahashi, Y. Watanabe, and M. Sato, "High Speed Spectral Domain Optical Coherence Tomography with Forward and Side-Imaging Probe," Jpn. J. Appl. Phys. **47**, 6540-6543 (2008).
58. S. Han, M. V. Sarunic, J. Wu, M. Humayun, and C. Yang, "Handheld forward-imaging needle endoscope for ophthalmic optical coherence tomography inspection," J Biomed Opt **13**, 020505 (2008).
59. C. P. Liang, C. W. Chen, J. Wierwille, J. Desai, R. Gullapalli, R. Mezrich, C. M. Tang, and Y. Chen, "Endoscopic Microscopy Using Optical Coherence Tomography," Curr. Med. Imaging Rev. **8**, 174-193 (2012).
60. X. Li, C. Chudoba, T. Ko, C. Pitris, and J. G. Fujimoto, "Imaging needle for optical coherence tomography," Optics letters **25**, 1520-1522 (2000).
61. X. Li, T. H. Ko, and J. G. Fujimoto, "Intraluminal fiber-optic Doppler imaging catheter for structural and functional optical coherence tomography," Optics letters **26**, 1906-1908 (2001).
62. V. X. Yang, M. Gordon, S. J. Tang, N. Marcon, G. Gardiner, B. Qi, S. Bisland, E. Seng-Yue, S. Lo, J. Pekar, B. Wilson, and I. Vitkin, "High speed, wide velocity dynamic range Doppler optical coherence tomography (Part III): in vivo endoscopic imaging of blood flow in the rat and human gastrointestinal tracts," Optics express **11**, 2416-2424 (2003).
63. P. R. Herz, Y. Chen, A. D. Aguirre, J. G. Fujimoto, H. Mashimo, J. Schmitt, A. Koski, J. Goodnow, and C. Petersen, "Ultrahigh resolution optical biopsy with endoscopic optical coherence tomography," Optics express **12**, 3532-3542 (2004).
64. A. R. Tumlinson, L. P. Hariri, U. Utzinger, and J. K. Barton, "Miniature endoscope for simultaneous optical coherence tomography and laser-induced fluorescence measurement," Applied optics **43**, 113-121 (2004).
65. D. C. Adler, Y. Chen, R. Huber, J. Schmitt, J. Connolly, and J. G. Fujimoto, "Three-dimensional endomicroscopy using optical coherence tomography," Nat. Photonics **1**, 709-716 (2007).

66. B. J. Vakoc, M. Shishko, S. H. Yun, W. Y. Oh, M. J. Suter, A. E. Desjardins, J. A. Evans, N. S. Nishioka, G. J. Tearney, and B. E. Bouma, "Comprehensive esophageal microscopy by using optical frequency-domain imaging (with video)," Gastrointestinal endoscopy **65**, 898-905 (2007).
67. M. J. Suter, B. J. Vakoc, P. S. Yachimski, M. Shishkov, G. Y. Lauwers, M. Mino-Kenudson, B. E. Bouma, N. S. Nishioka, and G. J. Tearney, "Comprehensive microscopy of the esophagus in human patients with optical frequency domain imaging," Gastrointestinal endoscopy **68**, 745-753 (2008).
68. G. Isenberg, W. Kang, H. Wang, Y. S. Pan, M. Jenkins, A. Chak, D. Agrawal, and A. Rollins, "Spectral-Domain Endoscopic Optical Coherence Tomography (EOCT) Using a Balloon Probe for Esophageal Imaging," Am. J. Gastroenterol. **104**, S29-S30 (2009).
69. J. Gamelin, Y. Yang, N. Biswal, Y. Chen, S. Yan, X. Zhang, M. Karemeddini, M. Brewer, and Q. Zhu, "A prototype hybrid intraoperative probe for ovarian cancer detection," Optics express **17**, 7245-7258 (2009).
70. J. Xi, L. Huo, Y. Wu, M. J. Cobb, J. H. Hwang, and X. Li, "High-resolution OCT balloon imaging catheter with astigmatism correction," Optics letters **34**, 1943-1945 (2009).
71. V. X. Yang, Y. Mao, B. A. Standish, N. R. Munce, S. Chiu, D. Burnes, B. C. Wilson, I. A. Vitkin, P. A. Himmer, and D. L. Dickensheets, "Doppler optical coherence tomography with a micro-electro-mechanical membrane mirror for high-speed dynamic focus tracking," Optics letters **31**, 1262-1264 (2006).
72. P. Meemon, K. S. Lee, S. Murali, and J. Rolland, "Optical design of a dynamic focus catheter for high-resolution endoscopic optical coherence tomography," Applied optics **47**, 2452-2457 (2008).
73. K. Aljasem, A. Werber, A. Seifert, and H. Zappe, "Fiber optic tunable probe for endoscopic optical coherence tomography," J. Opt. A: Pure Appl. Opt. **10**, 044012 (2008).
74. B. A. Standish, K. K. Lee, A. Mariampillai, N. R. Munce, M. K. Leung, V. X. Yang, and I. A. Vitkin, "In vivo endoscopic multi-beam optical coherence tomography," Physics in medicine and biology **55**, 615-622 (2010).
75. J. Wu, M. Conry, C. Gu, F. Wang, Z. Yaqoob, and C. Yang, "Paired-angle-rotation scanning optical coherence tomography forward-imaging probe," Optics letters **31**, 1265-1267 (2006).
76. U. Sharma, and J. U. Kang, "Common-path optical coherence tomography with side-viewing bare fiber probe for endoscopic optical coherence tomography," The Review of scientific instruments **78**, 113102 (2007).
77. K. M. Tan, M. Mazilu, T. H. Chow, W. M. Lee, K. Taguichi, B. K. Ng, W. Sibbett, C. S. Herrington, C. T. Brown, and K. Dholakia, "In-fiber common-path optical coherence tomography using a conical-tip fiber," Optics express **17**, 2375-2384 (2009).
78. N. M. Fried, S. Rais-Bahrami, G. A. Lagoda, A. Y. Chuang, L. M. Su, and A. L. Burnett, "Identification and imaging of the nerves responsible for erectile function in rat prostate, in vivo, using optical nerve stimulation and optical coherence tomography," IEEE J. Sel. Top. Quantum Electron. **13**, 1641-1645 (2007).

79. S. A. Boppart, B. E. Bouma, C. Pitris, G. J. Tearney, J. G. Fujimoto, and M. E. Brezinski, "Forward-imaging instruments for optical coherence tomography," Optics letters **22**, 1618-1620 (1997).
80. Y. Wang, M. Bachman, G. P. Li, S. Guo, B. J. Wong, and Z. Chen, "Low-voltage polymer-based scanning cantilever for in vivo optical coherence tomography," Opt Lett **30**, 53-55 (2005).
81. N. R. Munce, A. Mariampillai, B. A. Standish, M. Pop, K. J. Anderson, G. Y. Liu, T. Luk, B. K. Courtney, G. A. Wright, I. A. Vitkin, and V. X. Yang, "Electrostatic forward-viewing scanning probe for Doppler optical coherence tomography using a dissipative polymer catheter," Opt Lett **33**, 657-659 (2008).
82. A. M. Sergeev, V. M. Gelikonov, G. V. Gelikonov, F. I. Feldchtein, R. V. Kuranov, N. D. Gladkova, N. M. Shakhova, L. B. Suopova, A. V. Shakhov, I. A. Kuznetzova, A. N. Denisenko, V. V. Pochinko, Y. P. Chumakov, and O. S. Streltzova, "In vivo endoscopic OCT imaging of precancer and cancer states of human mucosa," Optics express **1**, 432-440 (1997).
83. X. M. Liu, M. J. Cobb, Y. C. Chen, M. B. Kimmey, and X. D. Li, "Rapid-scanning forward-imaging miniature endoscope for real-time optical coherence tomography," Optics letters **29**, 1763-1765 (2004).
84. M. J. Cobb, X. Liu, and X. Li, "Continuous focus tracking for real-time optical coherence tomography," Optics letters **30**, 1680-1682 (2005).
85. D. L. Wang, B. V. Hunter, M. J. Cobb, and X. D. Li, "Super-achromatic rapid scanning microendoscope for ultrahigh-resolution OCT imaging," IEEE J. Sel. Top. Quantum Electron. **13**, 1596-1601 (2007).
86. P. R. Herz, Y. Chen, A. D. Aguirre, K. Schneider, P. Hsiung, J. G. Fujimoto, K. Madden, J. Schmitt, J. Goodnow, and C. Petersen, "Micromotor endoscope catheter for in vivo, ultrahigh-resolution optical coherence tomography," Optics letters **29**, 2261-2263 (2004).
87. Y. Pan, H. Xie, and G. K. Fedder, "Endoscopic optical coherence tomography based on a microelectromechanical mirror," Optics letters **26**, 1966-1968 (2001).
88. A. D. Aguirre, P. R. Hertz, Y. Chen, J. G. Fujimoto, W. Piyawattanametha, L. Fan, and M. C. Wu, "Two-axis MEMS Scanning Catheter for Ultrahigh Resolution Three-dimensional and En Face Imaging," Opt Express **15**, 2445-2453 (2007).
89. P. H. Tran, D. S. Mukai, M. Brenner, and Z. P. Chen, "In vivo endoscopic optical coherence tomography by use of a rotational microelectromechanical system probe," Optics Letters **29**, 1236-1238 (2004).
90. J. Su, J. Zhang, L. Yu, and Z. Chen, "In vivo three-dimensional microelectromechanical endoscopic swept source optical coherence tomography," Opt Express **15**, 10390-10396 (2007).
91. J. Su, J. Zhang, L. Yu, G. C. H, M. Brenner, and Z. Chen, "Real-time swept source optical coherence tomography imaging of the human airway using a microelectromechanical system endoscope and digital signal processor," J Biomed Opt **13**, 030506 (2008).

92. Y. Pan, Z. Li, T. Xie, and C. R. Chu, "Hand-held arthroscopic optical coherence tomography for in vivo high-resolution imaging of articular cartilage," Journal of biomedical optics **8**, 648-654 (2003).
93. T. Q. Xie, H. K. Xie, G. K. Fedder, and Y. T. Pan, "Endoscopic optical coherence tomography with a modified microelectromechanical systems mirror for detection of bladder cancers," Applied optics **42**, 6422-6426 (2003).
94. T. Xie, H. Xie, G. K. Fedder, and Y. Pan, "Endoscopic optical coherence tomography with new MEMS mirror," Electron. Lett. **39**, 1535-1536 (2003).
95. Z. Wang, C. S. Lee, W. C. Waltzer, J. Liu, H. Xie, Z. Yuan, and Y. Pan, "In vivo bladder imaging with microelectromechanical-systems-based endoscopic spectral domain optical coherence tomography," J Biomed Opt **12**, 034009 (2007).
96. J. M. Zara, S. Yazdanfar, K. D. Rao, J. A. Izatt, and S. W. Smith, "Electrostatic micromachine scanning mirror for optical coherence tomography," Optics letters **28**, 628-630 (2003).
97. J. M. Zara, and P. E. Patterson, "Polyimide amplified piezoelectric scanning mirror for spectral domain optical coherence tomography," Appl. Phys. Lett. **89**, 263901 (2006).
98. C. H. Chong, K. Isamoto, and H. Toshiyoshi, "Optically modulated MEMS scanning endoscope," IEEE Photonics Technol. Lett. **18**, 133-135 (2006).
99. A. Jain, A. Kopa, Y. T. Pan, G. K. Fedder, and H. K. Xie, "A two-axis electrothermal micromirror for endoscopic optical coherence tomography," Ieee Journal of Selected Topics in Quantum Electronics **10**, 636-642 (2004).
100. J. T. W. Yeow, V. X. D. Yang, A. Chahwan, M. L. Gordon, B. Qi, I. A. Vitkin, B. C. Wilson, and A. A. Goldenberg, "Micromachined 2-D scanner for 3-D optical coherence tomography," Sens. Actuator A-Phys. **117**, 331-340 (2005).
101. W. G. Jung, J. Zhang, L. Wang, P. Wilder-Smith, Z. P. Chen, D. T. McCormick, and N. C. Tien, "Three-dimensional optical coherence tomography employing a 2-axis microelectromechanical scanning mirror," IEEE J. Sel. Top. Quantum Electron. **11**, 806-810 (2005).
102. T. Mitsui, Y. Watanabe, Y. Abe, K. Yashima, T. Nakagawa, and E. Umetsu, "Two-axis Optical Scanner Non-resonantly Driven by Electromagnetic Force for OCT Imaging," J. Micromech. Microeng **22**, 33-36 (2005).
103. W. Jung, D. T. McCormick, J. Zhang, L. Wang, N. C. Tien, and Z. P. Chen, "Three-dimensional endoscopic optical coherence tomography by use of a two-axis microelectromechanical scanning mirror," Appl. Phys. Lett. **88**, 163901 (2006).
104. W. Jung, D. T. McCormick, Y. C. Ahn, A. Sepehr, M. Brenner, B. Wong, N. C. Tien, and Z. Chen, "In vivo three-dimensional spectral domain endoscopic optical coherence tomography using a microelectromechanical system mirror," Opt Lett **32**, 3239-3241 (2007).
105. K. H. Kim, B. H. Park, G. N. Maguluri, T. W. Lee, F. J. Rogomentich, M. G. Bancu, B. E. Bouma, J. F. de Boer, and J. J. Bernstein, "Two-axis magnetically-driven MEMS scanning catheter for endoscopic high-speed optical coherence tomography," Opt Express **15**, 18130-18140 (2007).

106. K. Kumar, J. C. Condit, A. McElroy, N. J. Kemp, K. Hoshino, T. E. Milner, and X. Zhang, "Fast 3D in vivo swept-source optical coherence tomography using a two-axis MEMS scanning micromirror," JOA **10**, 044013 (2008).
107. K. H. Gilchrist, "Piezoelectric scanning mirrors for endoscopic optical coherence tomography," J. Micromech. Microeng (2009).
108. T. Q. Xie, S. G. Guo, Z. P. Chen, D. Mukai, and M. Brenner, "GRIN lens rod based probe for endoscopic spectral domain optical coherence tomography with fast dynamic focus tracking," Optics express **14**, 3238-3246 (2006).
109. T. Xie, D. Mukai, S. Guo, M. Brenner, and Z. Chen, "Fiber-optic-bundle-based optical coherence tomography," Optics letters **30**, 1803-1805 (2005).
110. J. H. Han, X. Liu, C. G. Song, and J. U. Kang, "Common path optical coherence tomography with fibre bundle probe," Electron. Lett. **45**, 1110-1111 (2009).
111. W. C. Wang, K. Zhang, Q. S. Ren, and J. U. Kang, "Comparison of different focusing systems for common-path optical coherence tomography with fiber-optic bundle as endoscopic probe," Opt. Eng. **48**, 103001 (2009).
112. A. D. Aguirre, Y. Chen, B. Bryan, H. Mashimo, Q. Huang, J. L. Connolly, and J. G. Fujimoto, "Cellular resolution ex vivo imaging of gastrointestinal tissues with optical coherence microscopy," Journal of biomedical optics **15**, 016025 (2010).
113. W. A. Hall, and C. L. Truwit, "1.5 T: spectroscopy-supported brain biopsy," Neurosurg. Clin. N. Am. **16**, 165-+ (2005).
114. E. White, M. Woolley, A. Bienemann, D. E. Johnson, M. Wyatt, G. Murray, H. Taylor, and S. S. Gill, "A robust MRI-compatible system to facilitate highly accurate stereotactic administration of therapeutic agents to targets within the brain of a large animal model," J Neurosci Methods **195**, 78-87 (2011).
115. A. J. Martin, P. S. Larson, J. L. Ostrem, W. Keith Sootsman, P. Talke, O. M. Weber, N. Levesque, J. Myers, and P. A. Starr, "Placement of deep brain stimulator electrodes using real-time high-field interventional magnetic resonance imaging," Magn Reson Med **54**, 1107-1114 (2005).
116. W. A. Hall, and C. L. Truwit, "Intraoperative MR imaging," Magn Reson Imaging Clin N Am **13**, 533-543 (2005).
117. A. R. Rezai, B. H. Kopell, R. E. Gross, J. L. Vitek, A. D. Sharan, P. Limousin, and A. L. Benabid, "Deep brain stimulation for Parkinson's disease: surgical issues," Mov Disord **21 Suppl 14**, S197-218 (2006).
118. U. Walter, A. Wolters, M. Wittstock, R. Benecke, H. W. Schroeder, and J.-U. Mueller, "Deep Brain Stimulation in Dystonia: Sonographic Monitoring of Electrode Placement into the Globus Pallidus Internus," Movement Disorders **24**, 1538-1541 (2009).
119. J. R. Moringlane, G. Fuss, and G. Becker, "Peroperative transcranial sonography for electrode placement into the targeted subthalamic nucleus of patients with Parkinson disease: technical note," Surg Neurol **63**, 66-69; discussion 69 (2005).

120. D. Berg, J. D. Steinberger, C. Warren Olanow, T. P. Naidich, and T. A. Yousry, "Milestones in magnetic resonance imaging and transcranial sonography of movement disorders," Mov Disord **26**, 979-992 (2011).
121. C. A. Giller, H. Liu, D. C. German, D. Kashyap, and R. B. Dewey, "A stereotactic near-infrared probe for localization during functional neurosurgical procedures: further experience," J Neurosurg **110**, 263-273 (2009).
122. J. D. Johansson, P. Blomstedt, N. Haj-Hosseini, A. T. Bergenheim, O. Eriksson, and K. Wardell, "Combined diffuse light reflectance and electrical impedance measurements as a navigation aid in deep brain surgery," Stereotact Funct Neurosurg **87**, 105-113 (2009).
123. K. Wardell, P. Blomstedt, J. Richter, J. Antonsson, O. Eriksson, P. Zsigmond, A. T. Bergenheim, and M. I. Hariz, "Intracerebral microvascular measurements during deep brain stimulation implantation using laser Doppler perfusion monitoring," Stereotact Funct Neurosurg **85**, 279-286 (2007).
124. D. Huang, E. A. Swanson, C. P. Lin, J. S. Schuman, W. G. Stinson, W. Chang, M. R. Hee, T. Flotte, K. Gregory, C. A. Puliafito, and et al., "Optical coherence tomography," Science **254**, 1178-1181 (1991).
125. E. A. Swanson, D. Huang, M. R. Hee, J. G. Fujimoto, C. P. Lin, and C. A. Puliafito, "High-speed optical coherence domain reflectometry," Optics letters **17**, 151-153 (1992).
126. Z. Yaqoob, J. Wu, and C. Yang, "Spectral domain optical coherence tomography: a better OCT imaging strategy," BioTechniques **39**, S6-13 (2005).
127. M. A. Choma, M. V. Sarunic, C. H. Yang, and J. A. Izatt, "Sensitivity advantage of swept source and Fourier domain optical coherence tomography," Optics express **11**, 2183-2189 (2003).
128. J. F. de Boer, B. Cense, B. H. Park, M. C. Pierce, G. J. Tearney, and B. E. Bouma, "Improved signal-to-noise ratio in spectral-domain compared with time-domain optical coherence tomography," Optics letters **28**, 2067-2069 (2003).
129. R. Leitgeb, C. K. Hitzenberger, and A. F. Fercher, "Performance of fourier domain vs. time domain optical coherence tomography," Optics express **11**, 889-894 (2003).
130. Z. P. Chen, Y. H. Zhao, S. M. Srinivas, J. S. Nelson, N. Prakash, and R. D. Frostig, "Optical Doppler tomography," Ieee Journal of Selected Topics in Quantum Electronics **5**, 1134-1142 (1999).
131. R. Leitgeb, L. Schmetterer, W. Drexler, A. Fercher, R. Zawadzki, and T. Bajraszewski, "Real-time assessment of retinal blood flow with ultrafast acquisition by color Doppler Fourier domain optical coherence tomography," Opt Express **11**, 3116-3121 (2003).
132. V. X. D. Yang, M. L. Gordon, E. Seng-Yue, S. Lo, B. Qi, J. Pekar, A. Mok, B. C. Wilson, and I. A. Vitkin, "High speed, wide velocity dynamic range Doppler optical coherence tomography (Part II): Imaging in vivo cardiac dynamics of Xenopus laevis," Optics express **11**, 1650-1658 (2003).

133. V. X. D. Yang, M. L. Gordon, B. Qi, J. Pekar, S. Lo, E. Seng-Yue, A. Mok, B. C. Wilson, and I. A. Vitkin, "High speed, wide velocity dynamic range Doppler optical coherence tomography (Part I): System design, signal processing, and performance," Opt Express **11**, 794-809 (2003).
134. A. Mariampillai, B. A. Standish, E. H. Moriyama, M. Khurana, N. R. Munce, M. K. Leung, J. Jiang, A. Cable, B. C. Wilson, I. A. Vitkin, and V. X. Yang, "Speckle variance detection of microvasculature using swept-source optical coherence tomography," Opt Lett **33**, 1530-1532 (2008).
135. Z. P. Chen, T. E. Milner, S. Srinivas, X. J. Wang, A. Malekafzali, M. J. C. vanGemert, and J. S. Nelson, "Noninvasive imaging of in vivo blood flow velocity using optical Doppler tomography," Optics Letters **22**, 1119-1121 (1997).
136. V. Westphal, S. Yazdanfar, A. M. Rollins, and J. A. Izatt, "Real-time, high velocity-resolution color Doppler optical coherence tomography," Opt Lett **27**, 34-36 (2002).
137. C. P. Liang, Y. Wu, J. Schmitt, P. E. Bigeleisen, J. Slavin, M. S. Jafri, C. M. Tang, and Y. Chen, "Coherence-gated Doppler: a fiber sensor for precise localization of blood flow," Biomed Opt Express **4**, 760-771 (2013).
138. S. K. Piechnik, P. A. Chiarelli, and P. Jezzard, "Modelling vascular reactivity to investigate the basis of the relationship between cerebral blood volume and flow under CO2 manipulation," Neuroimage **39**, 107-118 (2008).
139. S. A. Boppart, B. E. Bouma, C. Pitris, G. J. Tearney, J. G. Fujimoto, and M. E. Brezinski, "Forward-imaging instruments for optical coherence tomography," Opt Lett **22**, 1618-1620 (1997).
140. A. Sergeev, V. Gelikonov, G. Gelikonov, F. Feldchtein, R. Kuranov, N. Gladkova, N. Shakhova, L. Snopova, A. Shakhov, I. Kuznetzova, A. Denisenko, V. Pochinko, Y. Chumakov, and O. Streltzova, "In vivo endoscopic OCT imaging of precancer and cancer states of human mucosa," Opt Express **1**, 432-440 (1997).
141. Y. Pan, H. Xie, and G. K. Fedder, "Endoscopic optical coherence tomography based on a microelectromechanical mirror," Opt Lett **26**, 1966-1968 (2001).
142. Y. Pan, Z. Li, T. Xie, and C. R. Chu, "Hand-held arthroscopic optical coherence tomography for in vivo high-resolution imaging of articular cartilage," J Biomed Opt **8**, 648-654 (2003).
143. T. Xie, H. Xie, G. K. Fedder, and Y. Pan, "Endoscopic optical coherence tomography with a modified microelectromechanical systems mirror for detection of bladder cancers," Applied optics **42**, 6422-6426 (2003).
144. J. M. Zara, S. Yazdanfar, K. D. Rao, J. A. Izatt, and S. W. Smith, "Electrostatic micromachine scanning mirror for optical coherence tomography," Opt Lett **28**, 628-630 (2003).
145. X. Liu, M. J. Cobb, Y. Chen, M. B. Kimmey, and X. Li, "Rapid-scanning forward-imaging miniature endoscope for real-time optical coherence tomography," Opt Lett **29**, 1763-1765 (2004).
146. M. J. Cobb, X. Liu, and X. Li, "Continuous focus tracking for real-time optical coherence tomography," Opt Lett **30**, 1680-1682 (2005).

147. J. M. Zara, and P. E. Patterson, "Polyimide amplified piezoelectric scanning mirror for spectral domain optical coherence tomography," Appl. Phys. Lett. **89**, 3 (2006).
148. A. D. Aguirre, J. Sawinski, S. W. Huang, C. Zhou, W. Denk, and J. G. Fujimoto, "High speed optical coherence microscopy with autofocus adjustment and a miniaturized endoscopic imaging probe," Opt Express **18**, 4222-4239 (2010).
149. C. P. Fleming, K. J. Quan, and A. M. Rollins, "Toward guidance of epicardial cardiac radiofrequency ablation therapy using optical coherence tomography," J Biomed Opt **15**, 041510 (2010).
150. J. G. Wu, M. Conry, C. H. Gu, F. Wang, Z. Yaqoob, and C. H. Yang, "Paired-angle-rotation scanning optical coherence tomography forward-imaging probe," Opt Lett **31**, 1265-1267 (2006).
151. T. Xie, G. Liu, K. Kreuter, S. Mahon, H. Colt, D. Mukai, G. M. Peavy, Z. Chen, and M. Brenner, "In vivo three-dimensional imaging of normal tissue and tumors in the rabbit pleural cavity using endoscopic swept source optical coherence tomography with thoracoscopic guidance," J Biomed Opt **14**, Article No.: 064045 (2009).
152. T. Xie, S. Guo, Z. Chen, D. Mukai, and M. Brenner, "GRIN lens rod based probe for endoscopic spectral domain optical coherence tomography with fast dynamic focus tracking," Opt Express **14**, 3238-3246 (2006).
153. L. Yu, G. Liu, M. Rubinstein, A. Saidi, B. J. Wong, and Z. Chen, "Office-based dynamic imaging of vocal cords in awake patients with swept-source optical coherence tomography," J Biomed Opt **14**, 064020 (2009).
154. S. G. Guo, L. F. Yu, A. Sepehr, J. Perez, J. P. Su, J. M. Ridgway, D. Vokes, B. J. F. Wong, and Z. P. Chen, "Gradient-index lens rod based probe for office-based optical coherence tomography of the human larynx," J Biomed Opt **14**, 014017 (2009).
155. Q. Li, M. L. Onozato, P. M. Andrews, C. W. Chen, A. Paek, R. Naphas, S. A. Yuan, J. Jiang, A. Cable, and Y. Chen, "Automated quantification of microstructural dimensions of the human kidney using optical coherence tomography (OCT)," Opt Express **17**, 16000-16016 (2009).
156. S. A. Yuan, Q. Li, J. Jiang, A. Cable, and Y. Chen, "Three-dimensional coregistered optical coherence tomography and line-scanning fluorescence laminar optical tomography," Opt Lett **34**, 1615-1617 (2009).
157. S. A. Yuan, C. A. Roney, J. Wierwille, C. W. Chen, B. Y. Xu, G. Griffiths, J. Jiang, H. Z. Ma, A. Cable, R. M. Summers, and Y. Chen, "Co-registered optical coherence tomography and fluorescence molecular imaging for simultaneous morphological and molecular imaging," Phys Med Biol **55**, 191-206 (2010).
158. N. Burris, K. Schwartz, C. M. Tang, M. S. Jafri, J. Schmitt, M. H. Kwon, O. Toshinaga, J. Y. Gu, J. Brown, E. Brown, R. Pierson, and R. Poston, "Catheter-based infrared light scanner as a tool to assess conduit quality in coronary artery bypass surgery," Journal of Thoracic and Cardiovascular Surgery **133**, 419-427 (2007).

159. S. W. Jeon, M. A. Shure, K. B. Baker, D. Huang, A. M. Rollins, A. Chahlavi, and A. R. Rezai, "A feasibility study of optical coherence tomography for guiding deep brain probes," Journal of Neuroscience Methods **154**, 96-101 (2006).
160. D. Morofke, M. C. Kolios, I. A. Vitkin, and V. X. D. Yang, "Wide dynamic range detection of bidirectional flow in Doppler optical coherence tomography using a two-dimensional Kasai estimator," Optics Letters **32**, 253-255 (2007).
161. T. Klein, W. Wieser, C. M. Eigenwillig, B. R. Biedermann, and R. Huber, "Megahertz OCT for ultrawide-field retinal imaging with a 1050nm Fourier domain mode-locked laser," Opt Express **19**, 3044-3062 (2011).
162. J. Ren, J. Wu, E. J. McDowell, and C. Yang, "Manual-scanning optical coherence tomography probe based on position tracking," Opt Lett **34**, 3400-3402 (2009).
163. T. Schulz, S. Puccini, J. P. Schneider, and T. Kahn, "Interventional and intraoperative MR: review and update of techniques and clinical experience," Eur. Radiol. **14**, 2212-2227 (2004).
164. P. S. Larson, P. A. Starr, G. Bates, L. Tansey, R. M. Richardson, and A. J. Martin, "An Optimized System for Interventional Magnetic Resonance Imaging-Guided Stereotactic Surgery: Preliminary Evaluation of Targeting Accuracy," Neurosurgery **70**, 9 (2012).
165. G. R. Sutherland, I. Latour, and A. D. Greer, "Integrating an image-guided robot with intraoperative MRI: a review of the design and construction of neuroArm," IEEE Eng Med Biol Mag **27**, 59-65 (2008).
166. B. Yang, U. X. Tan, A. McMillan, R. Gullapalli, and J. P. Desai, "Design and Control of a 1-DOF MRI Compatible Pneumatically Actuated Robot with Long Transmission Lines," IEEE ASME Trans Mechatron **16**, 1040-1048 (2011).
167. N. V. Tsekos, A. Khanicheh, E. Christoforou, and C. Mavroidis, "Magnetic resonance - Compatible robotic and mechatronics systems for image-guided interventions and rehabilitation: A review study," in *Annual Review of Biomedical Engineering*(Annual Reviews, Palo Alto, 2007), pp. 351-387.
168. C. P. Liang, B. Yang, I. K. Kim, G. Makris, J. P. Desai, R. P. Gullapalli, and Y. Chen, "Concurrent multiscale imaging with magnetic resonance imaging and optical coherence tomography," J Biomed Opt **18**, 046015 (2013).
169. A. Ahmad, S. G. Adie, E. J. Chaney, U. Sharma, and S. A. Boppart, "Cross-correlation-based image acquisition technique for manually-scanned optical coherence tomography," Optics express **17**, 8125-8136 (2009).
170. X. Liu, Y. Huang, and J. U. Kang, "Distortion-free freehand-scanning OCT implemented with real-time scanning speed variance correction," Optics express **20**, 16567-16583 (2012).
171. T. Grau, R. W. Leipold, R. Conradi, E. Martin, and J. Motsch, "Efficacy of ultrasound imaging in obstetric epidural anesthesia," J Clin Anesth **14**, 169-175 (2002).
172. D. Karakitsos, N. Labropoulos, E. De Groot, A. P. Patrianakos, G. Kouraklis, J. Poularas, G. Samonis, D. A. Tsoutsos, M. M. Konstadoulakis, and A.

Karabinis, "Real-time ultrasound-guided catheterisation of the internal jugular vein: a prospective comparison with the landmark technique in critical care patients," Crit Care **10** (2006).
173. H. C. Eun, "Evaluation of skin blood flow by laser Doppler flowmetry," Clin Dermatol **13**, 337-347 (1995).
174. K. Kijsamanmith, S. Timpawat, N. Vongsavan, and B. Matthews, "Pulpal blood flow recorded from human premolar teeth with a laser Doppler flow meter using either red or infrared light," Arch Oral Biol **56**, 629-633 (2011).
175. A. L. Petoukhova, W. Steenbergen, and F. F. M. de Mul, "Path-length distribution and path-length-resolved Doppler measurements of multiply scattered photons by use of low-coherence interferometry," Optics Letters **26**, 1492-1494 (2001).
176. B. Varghese, V. Rajan, T. G. Van Leeuwen, and W. Steenbergen, "In Vivo Optical Path Lengths and Path Length Resolved Doppler Shifts of Multiply Scattered Light," Laser Surg Med **42**, 692-700 (2010).
177. V. Rajan, B. Varghese, T. G. van Leeuwen, and W. Steenbergen, "Review of methodological developments in laser Doppler flowmetry," Laser Med Sci **24**, 269-283 (2009).
178. J. M. Gardin, C. S. Burn, W. J. Childs, and W. L. Henry, "Evaluation of Blood-Flow Velocity in the Ascending Aorta and Main Pulmonary-Artery of Normal Subjects by Doppler Echocardiography," American Heart Journal **107**, 310-319 (1984).
179. V. Ntziachristos, "Going deeper than microscopy: the optical imaging frontier in biology," Nat Methods **7**, 603-614 (2010).
180. D. J. Smithies, T. Lindmo, Z. P. Chen, J. S. Nelson, and T. E. Milner, "Signal attenuation and localization in optical coherence tomography studied by Monte Carlo simulation," Phys Med Biol **43**, 3025-3044 (1998).
181. A. M. Zysk, S. G. Adie, J. J. Armstrong, M. S. Leigh, A. Paduch, D. D. Sampson, F. T. Nguyen, and S. A. Boppart, "Needle-based refractive index measurement using low-coherence interferometry," Optics Letters **32**, 385-387 (2007).
182. V. Yang, M. Gordon, B. Qi, J. Pekar, S. Lo, E. Seng-Yue, A. Mok, B. Wilson, and I. Vitkin, "High speed, wide velocity dynamic range Doppler optical coherence tomography (Part I): System design, signal processing, and performance," Opt Express **11**, 794-809 (2003).
183. W. Wieser, B. R. Biedermann, T. Klein, C. M. Eigenwillig, and R. Huber, "Multi-megahertz OCT: High quality 3D imaging at 20 million A-scans and 4.5 GVoxels per second," Opt Express **18**, 14685-14704 (2010).
184. L. Liu, J. A. Gardecki, S. K. Nadkarni, J. D. Toussaint, Y. Yagi, B. E. Bouma, and G. J. Tearney, "Imaging the subcellular structure of human coronary atherosclerosis using micro-optical coherence tomography," Nat Med **17**, 1010-1014 (2011).
185. O. Assayag, K. Grieve, B. Devaux, F. Harms, J. Pallud, F. Chretien, C. Boccara, and P. Varlet, "Imaging of non-tumorous and tumorous human brain tissues with full-field optical coherence tomography," NeuroImage. Clinical **2**, 549-557 (2013).

186. M. Axer, K. Amunts, D. Grassel, C. Palm, J. Dammers, H. Axer, U. Pietrzyk, and K. Zilles, "A novel approach to the human connectome: ultra-high resolution mapping of fiber tracts in the brain," Neuroimage **54**, 1091-1101 (2011).
187. C. L. Jeng, T. M. Torrillo, and M. A. Rosenblatt, "Complications of peripheral nerve blocks," British journal of anaesthesia **105 Suppl 1**, i97-107 (2010).
188. A. Curatolo, R. A. McLaughlin, B. C. Quirk, R. W. Kirk, A. G. Bourke, B. A. Wood, P. D. Robbins, C. M. Saunders, and D. D. Sampson, "Ultrasound-guided optical coherence tomography needle probe for the assessment of breast cancer tumor margins," AJR. American journal of roentgenology **199**, W520-522 (2012).
189. B. Yang, S. Roys, U.-X. Tan, M. Philip, H. Richard, R. P. Gullapalli, and J. P. Desai, "Design, development, and evaluation of a master-slave surgical system for breast biopsy under continuous MRI," The International Journal of Robotics Research (2013).
190. C. Sun, F. Nolte, K. H. Cheng, B. Vuong, K. K. Lee, B. A. Standish, B. Courtney, T. R. Marotta, A. Mariampillai, and V. X. Yang, "In vivo feasibility of endovascular Doppler optical coherence tomography," Biomed Opt Express **3**, 2600-2610 (2012).
191. B. Scheer, A. Perel, and U. J. Pfeiffer, "Clinical review: complications and risk factors of peripheral arterial catheters used for haemodynamic monitoring in anaesthesia and intensive care medicine," Critical care (London, England) **6**, 199-204 (2002).
192. L. A. Eisen, M. Narasimhan, J. S. Berger, P. H. Mayo, M. J. Rosen, and R. F. Schneider, "Mechanical complications of central venous catheters," Journal of intensive care medicine **21**, 40-46 (2006).
193. K. Petersson, C. Soderstrom, M. Kiani-Anaraki, and G. Levy, "Evaluation of the ability of thermal and electrical tests to register pulp vitality," Endod Dent Traumatol **15**, 127-131 (1999).
194. R. Weisleder, S. Yamauchi, D. J. Caplan, M. Trope, and F. B. Teixeira, "The validity of pulp testing: a clinical study," J Am Dent Assoc **140**, 1013-1017 (2009).
195. B. Gazelius, L. Olgart, and B. Edwall, "Restored vitality in luxated teeth assessed by laser Doppler flowmeter," Endod Dent Traumatol **4**, 265-268 (1988).
196. L. Olgart, B. Gazelius, and U. Lindh-Stromberg, "Laser Doppler flowmetry in assessing vitality in luxated permanent teeth," Int Endod J **21**, 300-306 (1988).
197. J. M. Schmitt, R. L. Webber, and E. C. Walker, "Optical determination of dental pulp vitality," IEEE Trans Biomed Eng **38**, 346-352 (1991).
198. W. C. Noblett, L. R. Wilcox, F. Scamman, W. T. Johnson, and A. Diaz-Arnold, "Detection of pulpal circulation in vitro by pulse oximetry," J Endod **22**, 1-5 (1996).
199. M. H. Pozzobon, R. de Sousa Vieira, A. M. Alves, J. Reyes-Carmona, C. S. Teixeira, B. D. de Souza, and W. T. Felippe, "Assessment of pulp blood flow in primary and permanent teeth using pulse oximetry," Dent Traumatol **27**, 184-188 (2011).